Bosonic Entanglement and Quantum Sensing from Energy Transfer in two-tone Floquet Systems

Yinan Chen,^{1,2,*} Andreas Elben,^{1,3,†} Angel Rubio,^{4,5} and Gil Refael^{1,2,6,‡}

¹Institute of Quantum Information and Matter, California Institute of Technology ²Department of Physics, California Institute of Technology, Pasadena CA 91125, USA ³Walter Burke Institute for Theoretical Physics, California Institute of Technology ⁴Max Planck Institute for the Structure and Dynamics of Matter,

Luruper Chaussee 149, 22761 Hamburg, Germany

⁵Center for Computational Quantum Physics, Simons Foundation Flatiron Institute, New York, NY 10010 USA

⁶AWS Center for Quantum Computing, Pasadena, CA, 91125, USA

(Dated: October 16, 2024)

Quantum-enhanced sensors, which surpass the standard quantum limit (SQL) and approach the fundamental precision limits dictated by quantum mechanics, are finding applications across a wide range of scientific fields. This quantum advantage becomes particularly significant when a large number of particles are included in the sensing circuit. Achieving such enhancement requires introducing and preserving entanglement among many particles, posing significant experimental challenges. In this work, we integrate concepts from Floquet theory and quantum information to design an entangler capable of generating the desired entanglement between two paths of a quantum interferometer. We demonstrate that our path-entangled states enable sensing beyond the SQL, reaching the fundamental Heisenberg limit (HL) of quantum mechanics. Moreover, we show that a decoding parity measurement maintains the HL when specific conditions from Floquet theory are satisfied—particularly those related to the periodic driving parameters that preserve entanglement during evolution. We address the effects of a priori phase uncertainty and imperfect transmission, showing that our method remains robust under realistic conditions. Finally, we propose a superconducting-circuit implementation of our sensor in the microwave regime, highlighting its potential for practical applications in high-precision measurements.

I. INTRODUCTION

Quantum sensors are widely used today in both scientific research [1–3] and technical applications [4–6]. Traditional quantum-enabled sensors utilize uncorrelated (classical) states, which limits their sensitivity to the standard quantum limit (SQL), dictated by the Heisenberg uncertainty principle [7]. In contrast, quantumenhanced sensors employ entangled states of many particles, allowing them to surpass the SQL and reach the ultimate limit set by quantum mechanics, known as the Heisenberg limit (HL) [8]. Typically, in an interferometric setup, such quantum-enhanced sensors use entangled qubits [9–11] or photons [12, 13] to probe an unknown parameter encoded in a quantum operation. Among these states, the Greenberger-Horne-Zeilinger (GHZ) state [8, 14] in qubit systems and the N00N state [13, 15] in optical systems—defined as $|\text{N00N}\rangle \equiv \frac{1}{\sqrt{2}}\left(|N,0\rangle + |0,N\rangle\right)$ over two photonic modes with a total of N photons was shown to precisely achieve the HL. Other types of entangled states, such as the entangled coherent state [16], Bat state [16–18], and coherent light mixed with a squeezed vacuum state [19], have also been demonstrated to asymptotically reach the HL at large photon numbers. Recent experiments have demonstrated the generation

of such entangled states of photons or phonons, typically with a particle number N<10. These states can be generated through phonon manipulation in trapped ion systems [20], parametric down-conversion and post-selection [21, 22], and mixing quantum and classical light [23]. However, developing efficient protocols to generate entangled states with a higher number of bosons and stabilizing the entanglement against experimental imperfections, such as photon loss and noise, remains a significant challenge.

The ability to engineer exotic states and phases of matter in controllable ways has spurred extensive theoretical [24–28] as well as experimental [29–31] efforts. This often involves driving materials, thereby creating synthetic dimensions and inducing novel dynamics that lack a static counterpart. For instance, spins driven adiabatically by fields with different frequencies give rise to quantized energy transfer between the drives, effectively realizing a temporal version of the quantum Hall effect [32–39]. When treating the drives in such a scheme as quantized, their state evolves as well, and the interaction with a spin or other system elements could be used as a tool to engineer the quantum state of the drives [40–42].

In this work, we relate sensing properties in quantum metrology to properties of the quasi-energy spectrum of Floquet systems, which enables the design of a *Floquet quantum sensor* that inherits the tunability from Floquet engineering while possessing a sub-SQL sensitivity. As a starting point, we consider a quantum system subject to two classical periodic drives. We demonstrate that the

^{*} vinanc@caltech.edu

[†] aelben@caltech.edu

[‡] refael@caltech.edu

direction of energy transfer between the two drives is determined by the initial state of the system. Treating the drives quantum-mechanically, this allows to generate entanglement within two modes of bosons over time. We quantify this entanglement using quantum Fisher information (QFI) [43], which serves as a global lower bound on the sensitivity dictated by the quantum Cramér–Rao bound (qCRB) [44, 45]. We show that the QFI of our path-entangled states, generated by energy transfer in Floquet systems, can be computed from the quasienergy band structure [46] of the Floquet Hamiltonian, and typically achieves the HL. Furthermore, we demonstrate that for drives with identical frequencies, a Mach-Zehnder interferometer (MZI) followed by a parity measurement [17, 18] on the output bosons can read out the QFI with at least SQL precision. We establish conditions on the quasienergy bands necessary for readout with HL precision using parity measurement. Additionally, we address the effects of the a priori uncertainties in the parameter (phase) to be measured [11, 47, 48] as well as particle loss in imperfect transmissions [49–51]. Our analysis suggests that our sensing protocol based on energy transfer can, in principle, be generalized to an arbitrarily large number of particles. Combined with the scalable readout by parity measurement, we anticipate that our sensing protocol can be realized in near-term experiments.

The paper is structured as follows. In Sec. II, we briefly review basic notions of quantum metrology. In Sec. III, we discuss the energy transfer in two-tone Floquet systems with classical driving fields. In Sec. IV, we quantize the drives as bosonic quantum fields and demonstrate that path-entangled states with OFI approaching the HL can be generated, employing properties of the quasi-energy band structure. We apply our results to three examples of driven qubits. Next, in Sec. V, we show that these path-entangled states can be used within a MZI with parity measurement to reach a sensing precision given the SQL and even the HL, if certain conditions satisfied. In Sec. VI, we study the effect of a priori uncertainty in the sensing parameter and imperfect transmission (photon loss) in the interferometer. Finally, in Sec. VII, we propose ways of realizing our quantum sensor in superconducting circuits.

II. QUANTUM SENSING AND THE QUANTUM FISHER INFORMATION

A. Quantum Fisher information

In this section, we review basic notions of quantum metrology and quantum estimation theory [52]. We focus on the estimation of a single parameter (phase) θ encoded via a unitary transformation $\rho_0 \to \rho_\theta = e^{-i\theta A}\rho_0 e^{i\theta A}$ on a probe quantum state ρ_0 prepared in a quantum sensor. Throughout the main text, we assume that the phase θ is unknown, but fixed in repeated runs of the experiment. This setting can be analyzed within the quantum Fisher

information framework [52]. More generally, the parameter can be treated as a random variable with a probability distribution $P(\theta)$ within a Bayesian approach, see App. H.

Our aim is to learn (estimate) the unknown parameter θ from measurements on ρ_{θ} . We model such measurement with a POVM Π specified by a set of positive Hermitian operators $\{\hat{\Pi}_{\mu}\}$ and corresponding outcomes π_{μ} , satisfying $\sum\limits_{\mu=1}^{M}\hat{\Pi}_{\mu}=\hat{\mathbb{1}}$, where M is the number of possible

measurement outcomes. Here, the probability $p(\pi_{\mu}|\theta)$ to observe outcome π_{μ} , given an a priori value of θ , is given by

$$p\left(\pi_{\mu}|\theta\right) = \operatorname{Tr}\left[\rho_{\theta}\hat{\Pi}_{\mu}\right]. \tag{1}$$

Finally, an estimator function $\theta_{\rm est}$ is given such that for each outcome π_{μ} , the estimated value of the a priori phase θ is given by $\theta_{\rm est}$ (π_{μ}), with mean value over repe-

titions
$$\bar{\theta}_{\text{est}} = \sum_{\mu=1}^{M} \theta_{\text{est}}(\pi_{\mu}) p(\pi_{\mu}|\theta)$$
 and variance

$$\Delta \theta_{\rm est}^2 = \sum_{\mu=1}^{M} \left(\theta_{\rm est} \left(\pi_{\mu} \right) - \overline{\theta}_{\rm est} \right)^2 p \left(\pi_{\mu} | \theta \right). \tag{2}$$

The choice of the (classical) estimation function is crucial for the success of the estimation procedure. In the following, we concentrate on locally unbiased estimators which faithfully estimate $\overline{\theta}_{\rm est}=\theta$ in an (at least infinitesimal) local environment around its fixed value, $\partial \theta_{\rm est}\left(\pi_{\mu}\right)/\partial \theta=1$. In this case, the celebrated Cramer-Rao bound [52] lower bounds the variance of the estimator

$$\Delta \theta_{\text{est}}^2 \ge \frac{1}{F_{\theta}[\rho_0, A, \Pi]}.$$
 (3)

Here, $F_{\theta}[\rho_0, A, \Pi]$ is the classical Fisher information

$$F_{\theta}[\rho_0, A, \Pi] = \sum_{\mu=1}^{M} \left[\partial_{\theta} \log p \left(\pi_{\mu} | \theta \right) \right]^2 p \left(\pi_{\mu} | \theta \right). \tag{4}$$

We note that $F_{\theta}[\rho_0, A, \Pi]$ depends on the choice of measurement (the POVM) and probe state ρ_{θ} . We can optimize $F_{\theta}[\rho_0, A, \Pi]$ over all possible POVMs Π to obtain the measurement that allows to estimate θ with minimal uncertainty (variance). The corresponding maximal Fisher information

$$F_q[\rho_0, A] = \sup_{\Pi} F_{\theta}[\rho_0, A, \Pi]$$
 (5)

is called the quantum Fisher information $F_q[\rho_0, A]$ [52]. It can be computed explicitly and takes a θ -independent form

$$F_q[\rho_0, A] = 2 \sum_{k,l,\lambda_k + \lambda_l > 0} \frac{(\lambda_k - \lambda_l)^2}{\lambda_k + \lambda_l} \left| \langle k | A | l \rangle \right|^2, \quad (6)$$

where λ_k are the eigenvalues of the probe state ρ_0 with eigenvectors $|k\rangle$ [52]. For a pure probe state $\rho_0 = |\psi_0\rangle \langle \psi_0|$ the QFI has a much simpler expression $F_q[\rho_0, A] = 4\left(\langle A^2\rangle - \langle A\rangle^2\right)$. Inserting into Eq. 3, this yields the quantum Cramer-Rao bound

$$\Delta \theta_{\text{est}}^2 \ge \frac{1}{F_q[\rho_0, A]},\tag{7}$$

which fundamentally limits the sensing precision for parameter θ encoded via an operator A into a quantum state ρ_0 . For a quantum state ρ_0 of N particles, the scaling of the quantum Fisher information with N is of central importance: The standard quantum limit (SQL) $F_q[\rho_0,A] \propto N$ applies to states with only classically correlated (or uncorrelated) particles. It originates from the Heisenberg uncertainty relation for each particle. Entanglement (quantum correlations) between the particles allows us to surpass this and reach the Heisenberg limit (HL) $F_q[\rho_0,A] \propto N^2$.

A lot of research has thus been dedicated to devising and implementing probe states ρ_0 with large quantum Fisher information (see [53, 54] and references therein). Additionally, the QFI involves a non-trivial optimization over all possible POVMs allowed by quantum mechanics, with the optimal POVM often not known or difficult to implement [53, 54]. A second challenge concerns thus the realization of a measurement Π such that the corresponding classical Fisher information is close to the optimal quantum Fisher information. Various examples of such sensors are known in the literature which we will discuss in the next subsection.

B. Examples of quantum sensors

Typical quantum sensors built from photons and atoms are the Mach-Zehnder interferometer (MZI) [16, 55, 56] and the Ramsey interferometer (RI) [11, 47, 48, 57]. In these systems, the experimental quantum sensing protocol can be summarized as follows [Fig. 1.(a)]: First, the probe state ρ_0 is prepared via an entangling operation $U_{\rm en}$ starting from a simple initial (product) state of photons or atoms, $\rho_0 = U_{\rm en} \rho_I U_{\rm en}^{\dagger}$. Second, the phase is encoded $\rho_0 \rightarrow \rho_\theta = e^{-i\theta A} \rho_0 e^{i\theta A}$. Lastly, the POVM measurement is realized by a decoding operation $U_{\rm de} \rho_\theta U_{\rm de}^{\dagger}$ followed by projective measurement.

In a Mach-Zehnder interferometer [Fig. 1.(b)], two modes of photons \hat{a}_1, \hat{a}_2 are sent to a 50-50 beam splitter represented by $\hat{\mathcal{U}}_{\rm en}^{\rm MZI}=e^{-i\hat{J}_y\frac{\pi}{2}}$ with $\hat{J}_y=\frac{i}{2}\left(\hat{a}_1^{\dagger}\hat{a}_2-\hat{a}_2^{\dagger}\hat{a}_1\right)$. The beam splitter separates the output photons to two interferometric paths, in which a phase θ is imprinted by a unitary operator $\hat{\mathcal{U}}_{\theta}^{\rm MZI}=e^{-i\hat{J}_z\theta}$ with $\hat{J}_z=\frac{1}{2}\left(\hat{a}_1^{\dagger}\hat{a}_1-\hat{a}_2^{\dagger}\hat{a}_2\right)$. After imprinting the phase, the probe state is sent to another 50-50 beam splitter given by $\hat{\mathcal{U}}_{\rm de}^{\rm MZI}=e^{-i\hat{J}_x\frac{\pi}{2}}$ with

 $\hat{J}_x = \frac{1}{2} \left(\hat{a}_1^{\dagger} \hat{a}_2 + \hat{a}_2^{\dagger} \hat{a}_1 \right)$. Finally, a photo-counting or parity measurement of the output photons are applied to decode the phase information. Note that in a Mach-Zehnder interferometer, $\hat{J}_{x,y,z}$ form the Schwinger representation of angular momentum, and hence is an example of the SU(2) interferometer [58]. To maximize the QFI $F_q = F_q \left[\rho_0, \hat{J}_z \right]$ corresponding to the generator \hat{J}_z , the (pure) probe state ρ_0 should maximize the variance of J_z , i.e. of the number difference of photons in the two modes. For an N-photon input, the probe state that maximizes such QFI is the N00N state $|N00N\rangle = \frac{1}{\sqrt{2}}(|N\rangle \otimes |0\rangle + |0\rangle \otimes |N\rangle)$, where $|N\rangle$ and $|0\rangle$ are the N-photon Fock state and the vacuum state, respectively. The N00N state yields a QFI $F_q = N^2$ that scales quadratically with the number of photons N. In comparison, in a classical (i.e. with classically non-entangled photons as probes) interferometer, F_q can at most scale linearly as N [59]. Entanglement between interferometric paths then improves the QFI by a factor of N. In the context of metrology, such entanglement between two interferometric paths is therefore expected to enhance the sensitivity of phase estimation.

In a Ramsey interferometer, the input state is instead a direct-product state $|0\rangle\otimes|0\rangle\otimes\cdots\otimes|0\rangle$ of N 2-level atoms. Accordingly, the entangler $\hat{\mathcal{U}}_{\mathrm{en}}^{\mathrm{RI}}=e^{-i\hat{S}_y\frac{\pi}{2}}$, phase imprinter $\hat{\mathcal{U}}_{\mathrm{de}}^{\mathrm{RI}}=e^{-i\hat{S}_z\theta}$, and the decoder $\hat{\mathcal{U}}_{\mathrm{de}}^{\mathrm{RI}}=e^{-i\hat{S}_x\frac{\pi}{2}}$ are realized via global rotations of the atoms $\hat{S}_{x,y,z}=\frac{1}{2}\sum_{j=1}^{N}\hat{\sigma}_{j}^{x,y,z}$ with $\hat{\sigma}_{j}^{x,y,z}$ the Pauli operators of the j-th atom. It is, again, clear from the construction that $\hat{S}_{x,y,z}$ form a representation of the SU(2) group and hence is another example of the SU(2) interferometer. The counterpart of the N00N state, which maximizes the QFI in the Mach-Zehnder interferometer, becomes the GHZ state defined as the macroscopically entangled state between atoms $|\mathrm{GHZ}\rangle=\frac{1}{\sqrt{2}}(|0\rangle\otimes\cdots\otimes|0\rangle+|1\rangle\otimes\cdots\otimes|1\rangle)$, which gives an N^2 -scaling QFI with respect to \hat{S}_z .

C. This work: Floquet quantum sensor

In the previous paragraphs, we discussed the MZI and RI, where metrologically useful quantum states are generated by applying entangling gates to the system's photons and qubits, respectively. Alternatively, it was proposed to couple the system to ancillary degrees of freedom and use operations on the ancilla to entangle the system's constituents [60–62]. In line with this approach, we study a setup in this work involving two bosonic modes coupled to an ancilla qubit [Fig. 1.(b)].

Previous studies showed that in the limit of classical drives—i.e., an ancilla qubit driven by two periodic classical driving fields—the ancilla qubit can mediate an en-

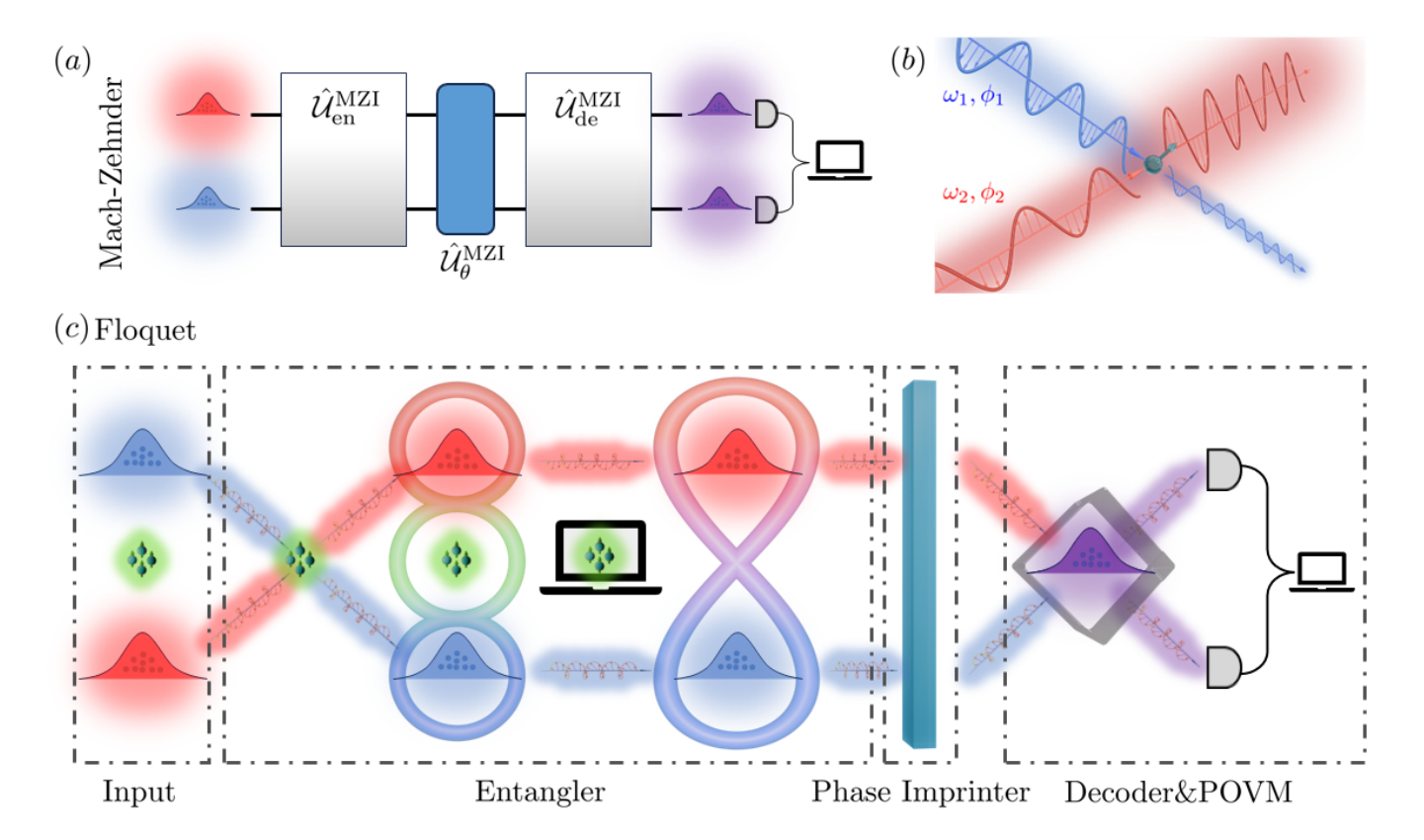


FIG. 1. Quantum sensing from energy transfer. (a) A circuit diagram of a Mach-Zehnder interferometer: Two modes of input bosons are first entangled by an entangler $\hat{\mathcal{U}}_{\text{en}}^{\text{MZI}}$. An unknown phase θ is then imprinted by a θ -dependent unitary $\hat{\mathcal{U}}_{\theta}^{\text{MZI}}$. Finally, a decoding circuit $\hat{\mathcal{U}}_{\text{de}}^{\text{MZI}}$ together with a set of POVM measurements are applied to the probe state. An estimator (computer) deduces the value of θ based on the measurement outcome. (b) Energy transfer between two classical drives with commensurate frequencies $\frac{\omega_1}{\omega_2} \in \mathbb{Q}$ and initial phases $\phi_{1,2}$. Depending on the initial configuration of the qudit, energy is converted from one mode to the other. (c) Quantum sensor based on energy transfer in two-tone Floquet systems. The circuit differs from a Mach-Zehnder interferometer in the entangler: two modes of input bosons are now coupled to a finite-dimensional ancilla. The entangled output of bosons is then generated by projecting out the ancilla degrees of freedom.

ergy transfer between the drives, a process known as frequency conversion [32, 63]. In this work, we explore the full quantum system and demonstrate that the energy transfer between the classical drives, mediated by the ancilla qubit, leads to the generation of path-entangled (mode-entangled) quantum states in the quantum system, also mediated by the ancilla qubit. Crucially, these path-entangled states are metrologically significant, with their QFI approaching the Heisenberg limit. We further show that this can be applied in an MZI-like interferometer to estimate phases with Heisenberg-limit sensitivity via a parity measurement under specific conditions.

Building on these results, we propose a Floquet quantum sensor [Fig. 1.(c)]: Two initially uncorrelated modes of bosons, for instance a product state of two coherent states or Fock states, first interact with a qubit (or qudit) for a time T. Following this interaction, a projective measurement on the qubit (or qudit) generates pathentangled bosonic modes as the output state. A phase θ is then encoded using $\hat{\mathcal{U}}_{\theta}^{\text{MZI}}$ as in the MZI. Finally, a readout circuit, comprising a decoder $\hat{\mathcal{U}}_{\text{de}}^{\text{MZI}}$ followed by a parity measurement, is applied to the phase-encoded

state. Under certain conditions on the initial states of the bosonic modes and their interaction with the qubit (see below), this allows to estimate the phase θ with Heisenberg-like sensitivity $\Delta^2\theta \sim 1/T^2$.

III. ENERGY TRANSFER BETWEEN CLASSICAL DRIVES

In this section, we discuss the energy transfer between two classical fields driving a single qubit acting as a mediator. We assume the qubit is governed by static Hamiltonian \hat{H}_0 and subject to two periodic classical drives described by the coupling Hamiltonians $\hat{H}_{1,2}\left(\omega_{1,2}t+\phi_{1,2}\right)=\hat{H}_{1,2}\left[\omega_{1,2}(t+T_{1,2})+\phi_{1,2}\right]$ [Fig. 1.(b)]. Here, $\omega_{1,2}$ denote the frequencies, $T_{1,2}=2\pi/\omega_{1,2}$ the periods and $\phi_{1,2}$ the initial phases of the drives. The full Hamiltonian reads as

$$\hat{H}(t) = \hat{H}_0 + \hat{H}_1(\omega_1 t + \phi_1) + \hat{H}_2(\omega_2 t + \phi_2). \tag{8}$$

To obtain a Floquet system, we require that two frequencies $\omega_{1,2}$ are commensurate, i.e. that their ratio, $\omega_1/\omega_2 \in$

 \mathbb{Q} is a rational number. Consequently, the Hamiltonian $\hat{H}(t)$ exhibits a period T_{com} (with T_{com} the least common multiple of $T_{1,2}$) such that $\hat{H}(t+T_{\text{com}})=\hat{H}(t)$.

Generally, the time evolution of the system is described by the $\hat{U}(t) = \mathcal{T}e^{-i\int_0^t \hat{H}(\tau)d\tau}$ where \mathcal{T} is the time-ordering symbol. In the following, we are interested in the system at stroboscopic times $T = kT_{\rm com}$ with k an integer. We can express the qubit state conveniently in terms of the (quasi-)eigenenergies ϵ_n and eigenstates $|n\rangle$ with n=1,2 of the Floquet Hamiltonian $H_F \equiv i/T_{\rm com} \log U(T_{\rm com})$ such that $(\hbar=1)$

$$U(T) = U(T_{\text{com}})^k = \sum_{n=1,2} e^{-i\epsilon_n k T_{\text{com}}} |n\rangle \langle n|. \quad (9)$$

We are interested in the long-time energy transfer between the two classical drives, viewing the quantum system as a mediator. We study the power $P_j(t) = \dot{E}_j(t) \equiv \langle \psi(t) | \frac{d \hat{H}_j(\omega_j t + \phi_j)}{dt} | \psi(t) \rangle$ absorbed from drive j at time t. Here, $|\psi(t)\rangle = \hat{\mathcal{U}}(t) |\psi(0)\rangle$ is the quantum state evolved in time under $\hat{H}(t)$ with initial state $|\psi(0)\rangle$. In general, $P_j(t)$ varies over time. The average power absorbed by drive j over a time window [0,T] is given by the time average [63]

$$\overline{P_{j}}(T) = \frac{1}{T} \int_{0}^{T} dt \langle \psi(t) | \frac{d\hat{H}_{j}}{dt} | \psi(t) \rangle$$

$$= \langle \psi(0) | i\omega_{j} \frac{1}{T} \hat{\mathcal{U}}^{\dagger}(T) \partial_{\phi_{j}} \hat{\mathcal{U}}(T) | \psi(0) \rangle$$

$$= \omega_{j} \langle \psi(0) | \hat{P}_{j}(T) | \psi(0) \rangle.$$
(10)

Here $\hat{P}_{j}(T) \equiv \frac{i}{T}\hat{\mathcal{U}}^{\dagger}(T)\,\partial_{\phi_{j}}\hat{\mathcal{U}}(T)$ and we suppress the initial phases $\phi_{1,2}$ subscript. For Floquet systems, at $T = kT_{\text{com}}$ $(k \in \mathbb{N})$, we can derive a compact form of $\overline{P}_{j}(T)$ for large T (App. A)

$$\hat{P}_{j}(T) = \sum_{n=1,2} \left(\partial_{\phi_{j}} \epsilon_{n} \right) |n\rangle \langle n| + O\left(\frac{1}{T}\right). \tag{11}$$

We denote the long-time limit as $\hat{P}_j \equiv \sum_{n=1,2} \left(\partial_{\phi_j} \epsilon_n \right) |n\rangle \langle n|$, the 'power operator'. We note that this expression is specific for driven qubits (two-level systems). We derive corresponding expressions for qudits (*d*-level systems) in App. A. \hat{P}_j is solely determined by properties of the Floquet Hamiltonian. Crucially, the transferred energy is however specified by the expectation value of \hat{P}_j with respect to the initial

state of the system. This introduces controllability: by varying the initial state $|\psi(0)\rangle$, we can control the energy transfer between the two classical drives.

We now demonstrate explicitly that it is indeed feasible to completely revert the energy transfer between the two drives by choosing the appropriate initial states of the driven quantum system. We focus first on the power operator \hat{P}_1 . We show in App. A that it is traceless, $\mathrm{Tr}\left[\hat{P}_1\right] = 0$ (equivalently, it also holds $\mathrm{Tr}\left[\hat{P}_2\right] = 0$).

This ensures two opposite eigenvalues $\pm P$ of \hat{P}_1 . Further denoting the corresponding eigenstates as $|\pm P\rangle$, this enables us to define two states $|0\rangle$, $|1\rangle$ as

$$|0\rangle = |P\rangle,$$

 $|1\rangle = |-P\rangle.$ (12)

Equivalently, one have opposite eigenvalues of \hat{P}_2 with eigenstates $|\pm P\rangle'$ and define the corresponding states $|0\rangle'$ and $|1\rangle'$. It follows from energy conservation $\omega_1\hat{P}_1 + \omega_2\hat{P}_2 = 0$ (see App. A) that these states are closely related, $|0\rangle' = |1\rangle$ and $|1\rangle' = |0\rangle$. Thus, by preparing the qubit in state $|0\rangle$ ($|1\rangle$), we can reverse the power transferred from drive 1 to drive 2.

Finally, we discuss energy conservation in the driven system in more details. Due to its bounded Hilbert space, the qubit can only store a finite amount of energy. Therefore, over long times T, there is no net flow of energy in or out of the qubit. The qubits acts as a mediator that enables energy exchange between the two drives. Mathematically, this poses a constraint on the quasienergy spectrum: $\epsilon_n = \epsilon_n(\omega_1, \omega_2, \phi_1, \phi_2)$ is only a function of $\frac{\phi_1}{\omega_1} - \frac{\phi_2}{\omega_2}$ [64], which is used in defining characteristic functions in Sec. V.

IV. ENERGY TRANSFER AND ENTANGLEMENT GENERATION BETWEEN QUANTUM DRIVES

A. Energy transfer between two quantum drives

We now quantize the two classical driving fields and treat them as two bosonic modes.

1. Quantizing the drives

We first rewrite the Hamiltonian Eq. (8) to make its periodic time dependence more explicit

$$\hat{H}(t) = \hat{H}_0 + \hat{H}_{1,o} \sin(\omega_1 t + \phi_1) + \hat{H}_{1,e} \cos(\omega_1 t + \phi_1) + \hat{H}_{2,o} \sin(\omega_2 t + \phi_2) + \hat{H}_{2,e} \cos(\omega_2 t + \phi_2)$$
(13)

Here, we have expanded $\hat{H}_j (\omega_j t + \phi_j)$ in Eq. (8) into $\hat{H}_{j,o} \sin{(\omega_j t + \phi_j)}$ and $\hat{H}_{j,e} \cos{(\omega_j t + \phi_j)}$. The subscript e,o in the coefficients denote even and odd contributions. We assume that these drives are realized by bosonic fields. Typical examples are photons from optical cavities [65], bosons in superconducting circuits [66], phonons from lattice or mechanical vibrations [67], and magnons from spin waves [68]. The quantization of the drives is hence accomplished via the substitution $e^{i(\omega_j t + \phi_j)} \rightarrow \hat{a}_j$, with \hat{a}_j the bosonic annihilation operator for the j-th drive satisfying $[\hat{a}_j, \hat{a}_j^{\dagger}] = 1$ and $[\hat{a}_1^{(\dagger)}, \hat{a}_2^{(\dagger)}] = 0$. With

this identification, the two-tone Hamiltonian becomes a time-independent Hamiltonian for the combined system of qubit and quantum drives

$$\hat{H}_{q} = \hat{H}_{0} + \hat{H}_{B} + \hat{H}_{1,o} \frac{\hat{a}_{1} - \hat{a}_{1}^{\dagger}}{2i} + \hat{H}_{1,e} \frac{\hat{a}_{1} + \hat{a}_{1}^{\dagger}}{2} + \hat{H}_{2,o} \frac{\hat{a}_{2} - \hat{a}_{2}^{\dagger}}{2i} + \hat{H}_{2,e} \frac{\hat{a}_{2} + \hat{a}_{2}^{\dagger}}{2}.$$

$$(14)$$

We have included a term $\hat{H}_B = \hat{\mathbb{1}}_0 \otimes \left(\omega_1 \hat{a}_1^{\dagger} \hat{a}_1 + \omega_2 \hat{a}_2^{\dagger} \hat{a}_2\right)$ to account for the free evolution of two drives, where $\hat{\mathbb{1}}_0$ is the identity operator on the qubit. The Hilbert space becomes a direct product between \mathcal{H} for the qubit and two Fock spaces $\mathcal{F}_{1,2}$ for quantum drives, $\mathcal{H}_q = \mathcal{H} \otimes \mathcal{F}_1 \otimes \mathcal{F}_2$. An orthonormal basis of this space is denoted as $|\lambda\rangle \otimes |n_1\rangle \otimes |n_2\rangle$ where $\{|\lambda\rangle\}_{\lambda=1,\dots,d}$ is an orthonormal basis of \mathcal{H} and $\{|n_{1,2}\rangle\}_{n_{1,2}=0,1,\dots}$ the Fock states for $\mathcal{F}_{1,2}$, respectively.

2. Approximation by a uniform lattice model

In Sec. III, we have shown that a qubit driven by two classical fields can serve a mediator for energy transfer. We now extend this to the quantized model. To this end, we note that for states with narrow Fock space distribution $\frac{\delta n_{1,2}}{\sqrt{n_{1/2,c}}} \ll 1$ with mean $n_{1/2,c} \equiv \langle \hat{a}_{1,2}^{\dagger} \hat{a}_{1,2} \rangle$ and

standard deviation $\delta n_{1,2} \equiv \sqrt{\langle \left(\hat{a}_{1,2}^{\dagger} \hat{a}_{1,2}\right)^2 \rangle - \langle \hat{a}_{1,2}^{\dagger} \hat{a}_{1,2} \rangle^2}$, the Hamiltonian (14) can be approximated by a solvable Floquet lattice model [32, 41]

$$\hat{H}_{l} = \hat{H}_{0} + \hat{H}_{B} + \hat{H}_{1,o}^{c} \frac{\hat{T}_{1} - \hat{T}_{1}^{\dagger}}{2i} + \hat{H}_{1,e}^{c} \frac{\hat{T}_{1} + \hat{T}_{1}^{\dagger}}{2}$$

$$+ \hat{H}_{2,o}^{c} \frac{\hat{T}_{2} - \hat{T}_{2}^{\dagger}}{2i} + \hat{H}_{2,e}^{c} \frac{\hat{T}_{2} + \hat{T}_{2}^{\dagger}}{2}.$$

$$(15)$$

Here, we neglected terms of error $O\left(\frac{\delta n_{1,2}}{\sqrt{n_{1/2},c}}\right)$ and defined the Fock space translation operators $\hat{T}_{1,2} \equiv \sum_{n_{1,2}} |n_{1,2}-1\rangle \langle n_{1,2}|$ and $\hat{H}^c_{1/2,o/e} = \sqrt{n_{1/2},c}\hat{H}_{1/2,o/e}$ are renormalized qubit operators. Using the translation symmetry, we change to a Fourier basis in Fock space $|\phi_{1,2}\rangle = \int_0^{2\pi} dn_{1,2}e^{i\phi_{1,2}n_{1,2}}|n_{1,2}\rangle$ and switch to an interaction picture with respect to the bosonic Hamiltonian $\hat{U}(t) = e^{-i\hat{H}_B t}$. Now, the lattice model Eq. (15) decomposes into a direct sum of Bloch Hamiltonians $\hat{H}_l(t) = \bigoplus_{\sigma} \hat{H}_{\phi}(t) \otimes |\phi\rangle \langle \phi|$ with

$$\hat{H}_{\phi}(t) = \hat{H}_{0} + \hat{H}_{1,o}^{c} \sin(\omega_{1}t + \phi_{1}) + \hat{H}_{1,e}^{c} \cos(\omega_{1}t + \phi_{1}) + \hat{H}_{2,o}^{c} \sin(\omega_{2}t + \phi_{2}) + \hat{H}_{2,e}^{c} \cos(\omega_{2}t + \phi_{2}),$$
(16)

with $\phi \equiv (\phi_1, \phi_2)$ and the corresponding $|\phi\rangle \equiv |\phi_1\rangle \otimes |\phi_2\rangle$. We briefly remark on the form of $\hat{H}_l(t)$ in the interaction picture. First, the phase is uniquely defined only

up to mod 2π , and the corresponding states should be understood in a periodic way $|\phi_{1,2}+2\pi\rangle=|\phi_{1,2}\rangle$. Second, $|\phi\rangle$ is motionless in the interaction picture, and hence the only dynamic evolution results from the (driven) system. For a given $|\phi\rangle$, the system evolves under $\hat{H}_0 + \hat{H}_{\phi}(t)$, which is identical to the two-tone Floquet Hamiltonian Eq. (13). We hence conclude that the dynamics of each phase component is described by the two-tone Floquet Hamiltonian Eq. (13).

In the following study of energy transfer and entanglement generation, we assume the dynamics of the original model Eq. (14) being well-described by the lattice model Eq. (15) and leave the numerical justification to Sec. IV C.

3. Energy transfer

We now analyze the dynamics under Eq. (16). We assume that there is no initial entanglement or correlation between the system and drives, i.e., we start with an initial product state

$$|\Psi(0)\rangle = |\psi(0)\rangle \otimes \int_{PZ} d^{2}\phi f(\phi) |\phi\rangle,$$
 (17)

where $|\Psi\left(0\right)\rangle$ and $|\psi\left(0\right)\rangle$ denote the initial system state and initial qubit state and $d^{2}\phi\equiv d\phi_{1}d\phi_{2}$ is the metric of the integral over the 1-st Brillouin zone BZ $\equiv\left[0,2\pi\right)^{2}$. Finally, $f\left(\phi\right)$ is the initial field distribution of the drives satisfying $\int\limits_{\mathrm{BZ}}d^{2}\phi\left|f\left(\phi\right)\right|^{2}=1$.

For each value of ϕ , the qubit evolves under a Floquet Hamiltonian $i\partial_t |\psi(\phi,t)\rangle = \hat{H}_{\phi}(t) |\psi(\phi,t)\rangle$. As before, we want to quantify power transferred to the *j*-th drive with j=1,2:

$$\overline{P_j}\left(T\right) = \frac{\omega_j}{T} \left(\left\langle \hat{a}_j^{\dagger} \hat{a}_j \right\rangle_0 - \left\langle \hat{a}_j^{\dagger} \hat{a}_j \right\rangle_T \right), \tag{18}$$

where $\langle \Box \rangle_0 = \langle \Psi(0) | \Box | \Psi(0) \rangle$ and $\langle \Box \rangle_T = \langle \Psi(T) | \Box | \Psi(T) \rangle$ are expectation values of \Box at t=0 and t=T, respectively. We observe the dynamics at stroboscopic times $T=kT_{\rm com}$ with k=0,1,2,... In App. B, we show that the long-time limit $\lim_{T\to\infty} \overline{P_j}(T) = \omega_j \langle \hat{P}_j[f] \rangle_0$ is determined by the 'functional power operator'

$$\hat{P}_j[f] = \int_{BZ} d^2 \phi ||f(\phi)||^2 \hat{P}_j(\phi).$$
 (19)

Here, $\hat{P}_{j}(\phi) = \sum_{n=1,2} \left[\partial_{\phi_{j}} \epsilon_{n}(\phi) \right] |n(\phi)\rangle \langle n(\phi)|$ is the power operator defined with respect to the ϕ -dependent Floquet Hamiltonian $\hat{H}_{\phi}(t)$, analogous to Sec. III. Since $\hat{P}_{j}[f]$ is a weighted sum of power operators $\hat{P}_{j}(\phi)$, it directly inherits properties such as tracelessness $\text{Tr}\left[\hat{P}_{j}[f]\right] = 0$ and energy conservation $\omega_{1}\hat{P}_{1}[f] + \omega_{2}\hat{P}_{2}[f] = 0$ (see Sec. III and App. B).

As its classical counterpart, the tracelessness of $\hat{P}_j[f]$ ensures two opposite eigenvalues $\pm P_f$ with eigenstates $|\pm P\rangle_f$, which enables us to define two states

$$\begin{aligned} |0\rangle_f &= |P\rangle_f\,,\\ |1\rangle_f &= |-P\rangle_f\,, \end{aligned} \tag{20}$$

which physically results in opposite energy flow from the j-th drive as $\langle 0|_f \hat{P}_j [f] |0\rangle_f + \langle 1|_f \hat{P}_j [f] |1\rangle_f = 0$. We note that the functional power operator $\hat{P}_j [f]$ depends on the field distribution $f(\phi)$ and so do its eigenvalues $\pm P_f$ and eigenstates $|\pm P\rangle_f$. As a result, different initial field distributions $f(\phi)$ result in different states $|0\rangle_f$ and $|1\rangle_f$.

B. Quadratically growing quantum Fisher information

In this subsection, we utilize energy transfer to generate states advantageous for quantum metrology, where the quantum Fisher information increases as T^2 , with T the time of conversion interaction. We have observed that flipping the qubit from $|0\rangle_f$ to $|1\rangle_f$ (and vice versa) changes the direction of energy flow accordingly. We now ask: how should we initialize the qubit so that useful entanglement for metrology can be generated at a later time? We address this question with the following statement:

Given the initial field distribution $f(\phi)$ of the drives and a non-zero power operator $\hat{P}_j[f]$, a path-entangled state can be prepared by first initializing the ancilla qubit in $|\beta, +\rangle_f = \frac{1}{\sqrt{2}} \left(|0\rangle_f + e^{i\beta} |1\rangle_f \right)$, then evolving the qubit-drives system for some time $T = kT_{\text{com}}$ according to \hat{H}_l , and finally measuring the qubit back to $|\beta, +\rangle_f$:

$$|\text{PES}\rangle_{T} \equiv \frac{1}{\mathcal{N}_{T}}\hat{\Pi}_{\beta}e^{-i\hat{H}_{l}T}\left[|\beta,+\rangle_{f} \otimes \int_{\text{BZ}} d^{2}\phi f(\phi)|\phi\rangle\right],$$
(21)

where $\hat{\Pi}_{\beta} \equiv |\beta, +\rangle_f \langle \beta, +|_f$ is the projection to the qubit state $|\beta, +\rangle_f$ and 'PES' is the abbreviation for 'pathentangled state'. \mathcal{N}_T is a T-dependent normalization factor. The QFI of $|\text{PES}\rangle_T$ with respect to \hat{J}_z (recall the MZI) asymptotically approaches the HL and is bounded by:

$$\frac{1}{2}P^{2}\left[f\right] \leq \lim_{T \to \infty} \frac{1}{T^{2}}F_{q}\left[\left|\text{PES}\right\rangle_{T}, \hat{J}_{z}\right] \leq 2P^{2}\left[f\right], \quad (22)$$

with $\hat{J}_z = \frac{1}{2} \left(\hat{a}_1^{\dagger} \hat{a}_1 - \hat{a}_2^{\dagger} \hat{a}_2 \right)$ and the scalar bound

$$P^{2}[f] \equiv \frac{1}{2} \int_{BZ} d^{2}\phi \left| f^{2}(\phi) \right| \left\{ \left[(\partial_{\Delta\phi}) \epsilon_{1} \right]^{2} + \left[(\partial_{\Delta\phi}) \epsilon_{2} \right]^{2} \right\},$$
(23)

where $\Delta \phi \equiv \phi_1 - \phi_2$ and $\partial_{\Delta \phi} \equiv \partial_{\phi_1} - \partial_{\phi_2}$.

While the proof is left to App. C, we clarify here the terminology used and the physical implications of the statement. The term 'path-entangled state' is borrowed from optical interferometry [69], where two spatially distinguishable photonic modes enter different interferometric arms or paths. Introducing (mode) entanglement between two modes yields 'path entanglement'. Proper path entanglement can endow the interferometer with HL sensitivity. Conversely, however, HL sensitivity (expressed in the QFI) does not necessarily imply path entanglement, unlike in qubit systems [70–72]. Examples of this are single-mode cat states $\frac{1}{2}[|\alpha\rangle \pm |-\alpha\rangle]$ [73], squeezed states [2], etc. Nevertheless, we demonstrate in Appendix D that path entanglement in $|PES\rangle_T$ significantly enhances the quantum Fisher information. The generalization and optimization of the quantum Fisher information for a d-level ancilla are discussed in App. E.

Finally, since the power operator $\hat{P}_j[f]$ and the bound $P^2[f]$ on the QFI are completely determined by the Floquet spectrum $\{\epsilon_n, |n\rangle\}$ with initial field distributions $f(\phi)$, the sensing ability of $|\text{PES}\rangle_T$ can be assessed before the experiment. In Sec.V, we will extend this observation to a specific choice of POVM measurement, and determine the maximal measurement sensitivity from the classical Floquet spectrum for Eq. (16).

C. Numerical examples

1. Example I: Two identical circularly-polarized drives

The first non-trivial model is a 2-level system under circularly-polarized drives:

$$\hat{H}_{\phi}(t) = \frac{\omega_0}{2} \hat{\sigma}_z + \mathcal{A} \left[\cos \left(\omega t + \phi_1 \right) + \cos \left(\omega t + \phi_2 \right) \right] \hat{\sigma}_x + \mathcal{A} \left[\sin \left(\omega t + \phi_1 \right) + \sin \left(\omega t + \phi_2 \right) \right] \hat{\sigma}_y.$$
(24)

The drives' requencies ω , amplitudes \mathcal{A} , and polarization are identical. The effective Hamiltonian in the rotating frame is given as (up to a unitary transform due to different choice of starting time $[t_0, t_0 + T_{\text{com}})$):

$$\hat{H}_{\text{eff}} = \frac{\omega_0 - \omega}{2} \hat{\sigma}_z + 2\mathcal{A}\cos\left(\frac{\phi_1 - \phi_2}{2}\right) \hat{\sigma}_x, \qquad (25)$$

with quasienergies (back in the lab frame)

$$\epsilon_{1/2} = \frac{1}{2} \left[\omega \pm \sqrt{(\omega_0 - \omega)^2 + 16A^2 \cos^2\left(\frac{\phi_1 - \phi_2}{2}\right)} \right]. \tag{26}$$

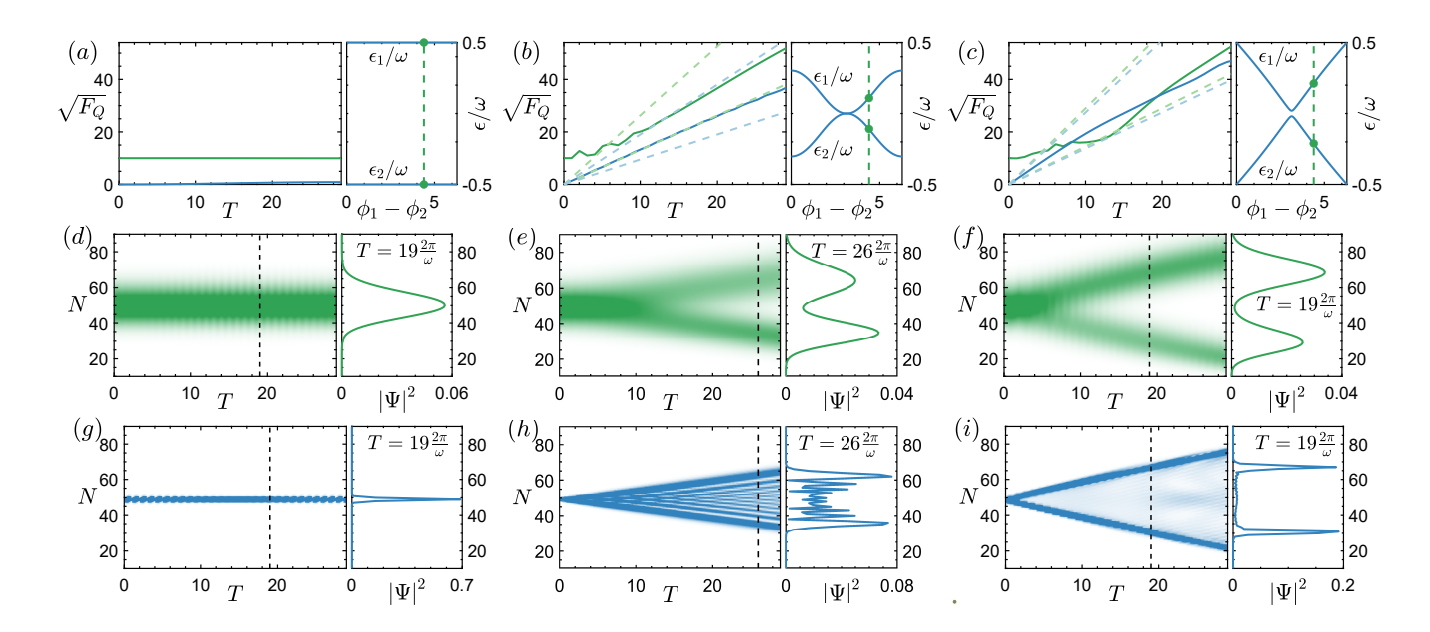


FIG. 2. Quantum Fisher information and wavefunction profiles of qubit-drives systems. (a)(d)(g) oscillating Zeeman field, (b)(e)(h) 2-level system with circularly-polarized drives and (c)(f)(i) polarization conversion. In (a)-(c), we plot both $\sqrt{F_Q} \equiv \sqrt{F_q \left[|\text{PES}\rangle_T, \hat{J}_z\right]}$ (left panels) and Floquet quasienergy bands (right panels) for three models. In the left panels, we plot $\sqrt{F_Q}$ for both coherent state (green solid) and Fock state (blue solid) input of the driving field. The corresponding bonds [upper and lower, see Eq. (22)] $P^2[f]$ are notated as green and blue dashed lines. In the right panels, we plot the quasienergy bands and indicate regions in the 1-st Brillouin zone $\phi_1 - \phi_2 \in [0, 2\pi)$, over which $f(\phi)$ spreads for both coherent (green dashed lines and dots) and Fock (blue solid curves) inputs. In (d)-(i), we plot wavefunction profiles $|\Psi|^2$ of the second drive for both coherent ((d)-(f)) and Fock ((g)-(i)) inputs as a function of time T (left panels) and their cross sections (right panels) at a single moment indicated by the black dashed lines in the left panels. For all three models, we start with average 50 bosons in each drive. For coherent-state inputs, we introduce an initial phase difference $\phi_{20} - \phi_{10} = 0.6\pi$ between two drives. Other parameters in different models are given as follows: for the oscillating Zeeman field, $B_0 = B_{1,2} g B_0 = \omega_{1,2}$; for the 2-level system with circularly-polarized drives, $\omega = \frac{\omega_0}{4}$, $\mathcal{A} = \frac{\omega_0}{8}$; and for the polarization conversion, $\omega = \omega_0$, $\mathcal{A} = \frac{\omega_0}{2}$. The corresponding parameters in the quantized models can be obtained via the procedure given in the main text (see Sec. IV).

Eq. (26) has a non-trivial dispersion relation with respect to $\phi_1 - \phi_2$, which, for a general field distribution $f(\phi)$, exhibits non-vanishing power $\hat{P}_{j}[f]$ and quadratically growing quantum Fisher information $F_q \sim P^2[f]T^2$. An exception comes with a symmetric field distribution $f(\phi_1, \phi_2) = f(\phi_2, \phi_1)$, where the power operator vanishes $\hat{P}_{j}[f] = 0$, while $P^{2}[f]$ remains non-zero in general. In Fig. 2.(b), (e), (h), we plot the time dependence of the QFI for $|PES\rangle_T$ and the wavefunctions $|\Psi|^2(N_2) \equiv \langle |N_2\rangle \langle N_2| \rangle_T$ of the second mode for different inputs. The quasienergy bands given in the right panel of Fig. 2 .(b) are dispersive except at $\phi_1 - \phi_2 = 0, \pi$ (it is also gapless at π for $\omega = \omega_0$). F_q is given in the left panel and is well-bounded by $\frac{1}{2}P^2[f]T^2$ and $2P^2[f]T^2$ represented by four dashed lines (green lines for coherentstate input with $|f(\boldsymbol{\phi})|^2 = \delta(\phi_1 - \phi_{10}, \phi_2 - \phi_{20})$, where ϕ_{10}, ϕ_{20} are the initial phases of the drives, and blue lines for Fock-state input with $|f(\phi)|^2 = \frac{1}{4\pi^2}$).

Typically, energy transfer and the QFI are analogous to the motion of waves: the mean group velocity $\partial_k \epsilon(k)$ quantifies the energy transfer, while the square mean

of the group velocity $[\partial_k \epsilon(k)]^2$ quantifies the QFI. In Fig. 2.(e), the wavefunction splits into up- and downbranches for a coherent-state input with an initial phase difference $\phi_{20} - \phi_{10} = 0.6\pi$ due to a non-vanishing $\hat{P}_j[f]$. In comparison, in Fig. 2.(h), the wavefunction of a twin-Fock-state input diffuses into a 'Bat state' at later times due to a vanishing $\hat{P}_j[f]$ but a non-zero $P^2[f]$ for $|f(\phi)|^2 = \frac{1}{4\pi^2}$.

2. Example II: Two circularly-polarized drives with opposite chirality

Flipping the sign of $\sin(\omega t + \phi_2)$ in Eq. (24) and shifting the time-independent part $\frac{\omega_0}{2}\hat{\sigma}_x$, the model now describes energy transfer between two circularly-polarized drives with opposite chiralities (polarization conversion):

$$\hat{H}_{\phi}(t) = \frac{\omega_0}{2} \hat{\sigma}_x + \mathcal{A} \left[\cos \left(\omega t + \phi_1 \right) + \cos \left(\omega t + \phi_2 \right) \right] \hat{\sigma}_x + \mathcal{A} \left[\sin \left(\omega t + \phi_1 \right) - \sin \left(\omega t + \phi_2 \right) \right] \hat{\sigma}_y.$$
(27)

The effective Hamiltonian of Eq. (27), as well as its quasienergies and quasieigenstates, can only be obtained numerically. Fortunately, some core properties of the spectrum can be obtained by looking at the symmetry of the Floquet Hamiltonian. that $\hat{\sigma}_x \hat{H}_{\phi_1,\phi_2}(t) \hat{\sigma}_x = \hat{H}_{\phi_2,\phi_1}(t)$, which swaps the subscript $\phi_1,\phi_2 \rightarrow \phi_2,\phi_1$. This directly leads to $\epsilon_{1,2}\left(\phi_{1},\phi_{2}\right) = \epsilon_{1,2}\left(\phi_{2},\phi_{1}\right), \; \left|1\left(\phi_{2},\phi_{1}\right)\right\rangle = \hat{\sigma}_{x}\left|1\left(\phi_{1},\phi_{2}\right)\right\rangle$ and $|2(\phi_2,\phi_1)\rangle = \hat{\sigma}_x |2(\phi_1,\phi_2)\rangle$. The $\hat{\sigma}_x$ operation hence matches quasienergies and quasieigenstates at (ϕ_1, ϕ_2) and (ϕ_2, ϕ_1) . Consequently, for a symmetric field distribution $f(\phi_1, \phi_2) = f(\phi_2, \phi_1)$, the functional power operator also experiences a sign flip under $\hat{\sigma}_x$ operation: $\hat{\sigma}_x \hat{P}_j[f] \hat{\sigma}_x = -\hat{P}_j[f]$. The initial state of the ancilla can be hence prepared as $|\beta, +\rangle_f = |\uparrow / \downarrow \rangle$ with $\hat{\sigma}_x |\uparrow\rangle \downarrow\rangle = \pm |\uparrow\rangle \downarrow\rangle$ eigenstates of $\hat{\sigma}_x$.

More properties are obtained by numerically solving the quasienergies, which are given in the right panel of Fig. 2.(c). First, the bands are gapless at $\phi_1 = \phi_2$ with a finite dispersion, as the quasienergies are defined modulo ω , and hence $\pm 0.5\omega$ are identified. Second, the bands are linear about $\phi_1 - \phi_2 = 0, \pi$, which results in $P^2[f]$ approximately independent of the initial distribution $f(\phi)$. This is shown in Fig. 2.(c), where the QFI for the coherent-state and Fock-state inputs grows at a similar rate and the dashed lines representing the bounds overlap.

Another consequence of the linearity is that wavefunctions do not disperse as the second derivative vanishes $\partial_{\Delta\phi}^2 \epsilon_{1,2} = 0$ except at $\phi_1 - \phi_2 = \pi$ with a finite gap opening. In Fig. 2.(f), (i), wavefunctions for both coherent-state and Fock-state inputs are translated into up- and down-branches and maintain their initial shapes for each branch, analogous to soliton motion in waves. This model, therefore, functions like a quantum beam splitter that evenly splits the inputs without introducing unwanted superpositions. Specifically, a Fock-state input results in a N00N-like output [Fig.2.(i)], whereas the previous model produces more superpositions [Fig.2.(h)] for the same input.

3. Example III: Two-tone oscillating Zeeman field

Consider a spin-1/2 particle interacting with a two-tone Zeeman field $\boldsymbol{B}(t) = [B_0 + B_1 \cos{(\omega_1 t + \phi_1)} + B_2 \cos{(\omega_2 t + \phi_2)}] \hat{z}$ with commensurate frequencies $\omega_{1,2}$ along z-axis:

$$\hat{H}(t) = -g\boldsymbol{B}(t) \cdot \hat{\boldsymbol{S}},\tag{28}$$

with g the coupling strength and $\hat{S} = (\hat{S}_x, \hat{S}_y, \hat{S}_z)$ the spin vector. The effective Hamiltonian is given as:

$$\hat{H}_{\text{eff}} = -gB_0\hat{S}_z,\tag{29}$$

which is completely independent of initial phases $\phi = (\phi_1, \phi_2)$. Since the Hamiltonian commutes with itself at different times $\left[\hat{H}\left(t\right), \hat{H}\left(t'\right)\right] = 0$. The ϕ -independence makes both $\hat{P}_j\left[f\right]$ and $P^2\left[f\right]$ vanish for any field distribution $f\left(\phi\right)$. As a result, there is neither energy transfer between the drives nor entanglement generation when quantizing the drives. In Fig. 2.(a), (d), (g), we plot the time dependence of the QFI and wavefunctions for different initial states of the drives. The flat bands in the right panel of Fig. 2.(a) now results in T-independent QFI [Fig. 2.(a), left panel] and wavefunctions [Fig. 2.(d), (g)]. In other words, both energy transfer and growing sensitivity require a dispersive quasi-energy spectrum.

4. Discussion of the lattice approximation

Throughout the study of the dynamics and entanglement generation, we assume the Floquet lattice model Eq. (16) is a good approximation of the quantized-drives model Eq. (14) upon the condition $\frac{\delta n_{1,2}}{\sqrt{n}_{1/2,c}}\ll 1$ throughout the time evolution. This condition is violated at later times when the growing ΔJ_z increases $\delta n_{1,2}$ to being comparable with $n_{1/2,c}$ [Fig. 2.(e), (f), (h), (i)]. However, from extensive numerical study of both three models mentioned above and other driven models, the dynamics of the wavefunction and the growing of QFI $F_q\left[|\mathrm{PES}\rangle_T\,,\hat{J}_z\right]$ are well-captured by the $\hat{P}_j\left[f\right]$ and $P^2\left[f\right]$ even at later moments when $\delta n_{1,2}\approx n_{1/2,c}.$ We hence conclude that the dynamics of the quantized-drives model Eq. (14) is well-described by Eq. (16) as a direct sum of two-tone Floquet Hamiltonians Eq. (13).

V. DECODING A PHASE WITH PARITY MEASUREMENTS

A. General requirements on drive frequencies and band structure

We have seen that PES's with QFI exhibiting Heisenberg scaling can be generated using various Floquet models of the form (14) by properly initializing the ancilla qubit. A natural question arises: can we maintain such HL sensitivity with a measurement accessible to current experiments? Our goal in this section is, therefore, to find general conditions on models of the form of Eq. (14) which yield HL sensitivity with experimentally accessible measurements. In optical interferometry, one widely used measurement is the parity of an output mode of an interferometer [17], and is shown to approach sub-SQL sensitivity for various path-entangled states [16, 18, 74, 75]. In principle, the parity measurement is scalable to large number of photons with recent

experimental success [76, 77]. We thus concentrate in this section on the use of the parity measurement.

As described in Sec. II C, we adopt a parity measurement on the second output mode $\hat{\Pi} \equiv (-1)^{\hat{a}_2^{\dagger}\hat{a}_2}$ after a Mach-Zehnder interferometer as our POVM measurement [Fig. 1.(c)]. By the end of this section, we will filter out Floquet models Eq. (14) capable of generating PES's that exhibit sub-SQL sensitivity from a single-shot parity measurement. Recall the phase imprinter and decoder in a Mach-Zehnder interferometer is given as $\hat{\mathcal{U}}_{\theta}^{\text{MZI}} = e^{-i\hat{J}_x\theta}$ and $\hat{\mathcal{U}}_{\text{de}}^{\text{MZI}} = e^{-i\hat{J}_x\pi}$, respectively. The parity operator, under these transforms, becomes

$$\hat{\Pi}_{\theta} = \hat{\mathcal{U}}_{\theta}^{\text{MZI},\dagger} \, \hat{\mathcal{U}}_{\text{de}}^{\text{MZI},\dagger} \, \hat{\Pi} \, \hat{\mathcal{U}}_{\text{de}}^{\text{MZI}} \, \hat{\mathcal{U}}_{\theta}^{\text{MZI}} = e^{2i\hat{J}_{z}\left(\theta - \frac{\pi}{2}\right)} \hat{S}, \tag{30}$$

where $\hat{S} = \sum_{n,m=1}^{\infty} |n\rangle \langle m| \otimes |m\rangle \langle n|$ is the SWAP operator over two input bosonic modes. Redefining the phase $\tilde{\theta} \equiv \theta - \frac{\pi}{2}$, the parity operator has a simple dependence on $\tilde{\theta}$ as $\hat{\Pi}_{\tilde{\theta}} = e^{2i\hat{J}_z\tilde{\theta}}\hat{S}$. The derivation of Eq. (30) is left to App. F.

From classical information theory (Sec. II), the variance of an unbiased estimator $V_{\rm ub}(\tilde{\theta})$ is lower-bounded by the inverse of the classical Fisher information $F_{\tilde{\theta}}$ [Eq. (4)], which, for the parity operator $\hat{\Pi}_{\tilde{\theta}}$, is given by [17]

$$F_{\tilde{\theta}} = \frac{\left| \partial_{\tilde{\theta}} \left\langle \Pi_{\tilde{\theta}} \right\rangle_{\text{PES}} \right|^2}{1 - \left\langle \Pi_{\tilde{\theta}} \right\rangle_{\text{PES}}^2},\tag{31}$$

where $\langle \Box \rangle_{\mathrm{PES}} \equiv \langle \mathrm{PES}|_T \, \Box \, | \mathrm{PES} \rangle_T$ the expectation value of \Box with respect to the PES.

For $\omega_1 \neq \omega_2$, we expect Eq. (31) to be unable to reach either the SQL or the HL. We leave the analytic arguments to App. G. Instead, here we provide the physical intuition behind this observation: in an SU(2)interferometer, all unitary operators commute with the total number operator, which is the total spin $\hat{S}^2 = \hat{S}_x^2 + \hat{S}_y^2 + \hat{S}_z^2$ in a Ramsey interferometer and the total number of photons $\hat{N} = \hat{a}_1^{\dagger} \hat{a}_1 + \hat{a}_2^{\dagger} \hat{a}_2$ in a Mach-Zehnder interferometer. In other words, each operation in the sensing circuit preserves the angular momentum or total number of particles. Superposition and interference can hence only exist between states with identical angular momentum or number of particles. In the language of functional power operators, the conservation of particle number is translated into $\hat{P}_1[f] + \hat{P}_2[f] = 0$. This is consistent with the energy conservation $\omega_1 \hat{P}_1[f] + \omega_2 \hat{P}_2[f] = 0$ if and only if two frequencies are identical $\omega_1 = \omega_2$. We thus find that a necessary condition for approaching the SQL or HL is having drives with identical frequencies.

For $\omega_1=\omega_2=\omega$, in general, we show in App. G that the asymptotic behaviors of $\langle \Pi_{\tilde{\theta}}\rangle_{\text{PES}}$ and $\partial_{\tilde{\theta}}\langle \Pi_{\tilde{\theta}}\rangle_{\text{PES}}$ are, instead, governed by $\langle \Pi_{\tilde{\theta}}\rangle_{\text{PES}}=O(\frac{1}{\sqrt{T}})$ and $\partial_{\tilde{\theta}}\langle \Pi_{\tilde{\theta}}\rangle_{\text{PES}}=O\left(\sqrt{T}\right)$, which endow $F_{\tilde{\theta}}=O(T)$ that approaches the SQL. Although the QFI of pathentangled states $|\text{PES}\rangle_T$ exhibit the HL scaling in general, the parity measurement $\langle \Pi_{\tilde{\theta}}\rangle_{\text{PES}}$ can only extract this phase information with precision given by the SQL. This is because the time evolution appears in exponentials $e^{-i\epsilon_n(\phi)T}$ [Eq. (9)] oscillating fast at $T\gg 1$ and wiping out a significant amount of information as most of them average to 0 in $\langle \hat{\Pi}_{\tilde{\theta}} \rangle$.

To overcome such fast oscillation in the long time limit, stationary phases (also known as critical points) of the exponentials have to be degenerate, giving a 'steady region' of ϵ_n in which the exponentials vary slowly. This, as derived in App. G, can be formulated by the following condition:

$$\partial_{\tilde{x}}^{2} \mathcal{G}_{nm}(\tilde{x}, \tilde{\theta})|_{\tilde{x}=\tilde{x}_{0}} = 0, \quad \partial_{\tilde{\theta}} \mathcal{G}_{nm}(\tilde{x}_{0}, \tilde{\theta}) \neq 0,$$
 (32)

where

$$\mathcal{G}_{nm}(\tilde{x},\tilde{\theta}) \equiv \epsilon_n \left(\tilde{x}\right) - \epsilon_m \left(-\tilde{x} + \frac{\sqrt{2}}{\omega}\tilde{\theta}\right) \tag{33}$$

is a measure of energy difference between band n,m=1,2 at \tilde{x} and $-\tilde{x}+\frac{\sqrt{2}}{\omega}\tilde{\theta}$, respectively. $\tilde{x}\equiv\frac{1}{\sqrt{2}\omega}\left(\phi_1-\phi_2\right)$ is the time delay (recall, due to energy conservation, the quasi energies only depend on a single parameter \tilde{x}) between two drives and \tilde{x}_0 the critical point defined by $\partial_{\tilde{x}}\mathcal{G}_{nm}(\tilde{x},\tilde{\theta})|_{\tilde{x}=\tilde{x}_0}=0$. An asymptotic Heisenberg-limit sensitivity $\sqrt{F_{\tilde{\theta}}}\sim T^2$ at $\tilde{\theta}$ is obtainable from the parity measurement on $|\text{PES}\rangle_T$ only if Eq. (32) has solution \tilde{x}_0 for at least one choice of n,m. Here, we assume that $\tilde{x}_0, -\tilde{x}_0+\frac{\sqrt{2}}{\omega}\tilde{\theta}$ lie within the support of $f(\phi)$. We hence dub \mathcal{G}_{nm} characteristic functions (of quasienergy bands) determining the sensitivity from parity measurement. A schematic illustration of the characteristic functions \mathcal{G}_{nm} for a 2-level ancilla can be found in Fig. 3.

B. Numerical examples

1. Example I: Two circularly-polarized drives with same chiralities

A simple way to produce degenerate critical points, as defined in Eq. (32), is requiring a symmetric band structure about some value of $\tilde{\theta}$. An example of symmetric band structures can be seen in our previous 2-level system with identical circularly polarized drives [Eq. (24)]. In this model, two bands meet at $\phi_1 - \phi_2 = \pi$ while being symmetric about $\phi_1 - \phi_2 = 0$, π , which gives

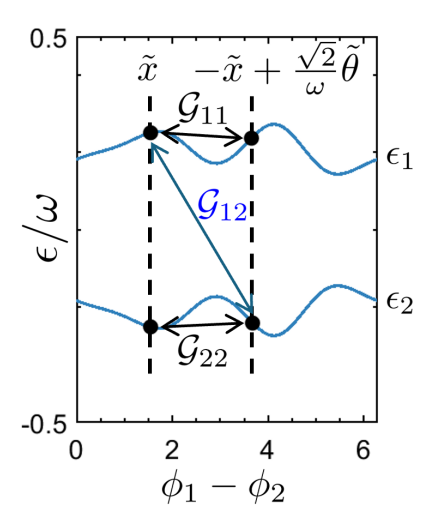


FIG. 3. A Schematic illustration of the characteristic functions. For the qubit model described in Eq. (34), one has two quasienergy bands symmetric about $\epsilon=0$. Consequently, two classes of characteristic functions can be defined: intraband, \mathcal{G}_{11} and \mathcal{G}_{22} , and interband, \mathcal{G}_{12} and \mathcal{G}_{21} . Physically, they measure the difference in quasienergies within and between bands. The band structure of Eq. (34) is obtained for $\omega=\omega_0$ and $\mathcal{A}=\frac{\omega_0}{2}$.

$$\mathcal{G}_{11}(\tilde{x},0) = \mathcal{G}_{22}(\tilde{x},0) = 0 \text{ and } \mathcal{G}_{11}(\tilde{x},\pi) = \mathcal{G}_{22}(\tilde{x},\pi) = 0$$
 for all $\tilde{x} \in [-\pi/\sqrt{2}\omega, \pi/\sqrt{2}\omega)$.

Consequently, a generic field distribution $f(\phi)$ is expected to exhibit an asymptotic HL scaling $\Delta \tilde{\theta} \sim T^{-1}$ at $T \gg T_{\rm com}$ for $\tilde{\theta} = 0, \pi$ [Fig. 4.(b): from numerics, we observe that with a Fock state input the sensitivity scales approximately as $\Delta \tilde{\theta} \sim T^{-0.98}$ at $\tilde{\theta} = 0, \pi$]. However, for other values of $\tilde{\theta}$, critical points of $\mathcal{G}_{nm}(\tilde{x}, \tilde{\theta})$ become non-degenerate and hence fail to approach the HL.

There is one subtlety for coherent-state inputs: a symmetric coherent-state input $f(\phi_1, \phi_2) = f(\phi_2, \phi_1)$ requires a degenerate critical point at $\tilde{\theta} = 0$ (App. G), but as the power $\partial_{\Delta\phi}\epsilon_{1,2}$ is vanishing at the same point, it fails to satisfy the second condition in Eq. (32) and fails to reach the HL. On the other hand, an asymmetric distribution $\left|f\left(\phi\right)\right|^{2}=\delta\left(\phi_{1}-\phi_{10},\phi_{2}-\phi_{20}\right)$ for coherent-state inputs requires a degenerate critical point of $\mathcal{G}_{nm}(\tilde{x}, \tilde{\theta})$ at $\tilde{\theta} = \phi_{10} - \phi_{20}$ (App. G), where $\phi_{10,20}$ are (different) initial phases of the coherent drives. This is only obtainable for $\phi_{10} - \phi_{20} = \pi$, which again leads to vanishing power as $\partial_{\Delta\phi}\epsilon_{1,2}|_{\Delta\phi=\pi}=0$. As a result, this model [Eq. (24)] fails to reach the HL for any coherentstate input with the parity measurement. Thus, for a coherent-state input, we find somewhat counterintuitively that the QFI grows quadratically while the parity measurement is not sensitive to the encoded phase [Fig. 4.(b), (h)].

2. Example II: Two circularly-polarized drives with opposite chiralities

Two ways to reach the HL scaling for coherent-state inputs are as follows: (1) a degenerate critical point at $\tilde{\theta} = 0, \pi$, while maintaining a finite dispersion $\partial_{\Delta\phi}\epsilon_{1,2}\neq 0$, or (2) requiring linear and symmetric dispersion about some value of $\phi_1 - \phi_2$. For (1), one can simply choose a symmetric distribution or a π -phase difference for the coherent-state input, and the nonvanishing power ensures an asymptotic HL scaling. For (2), the restriction on $\hat{\theta}$ is further lifted, since linearity and symmetry allow $\mathcal{G}_{nm}(\tilde{x}, \hat{\theta})$ with degenerate critical points for any \tilde{x} and $-\tilde{x} + \frac{\sqrt{2}}{\omega}\tilde{\theta}$ as long as they both lie in such linear and symmetric regions (recall Dirac points). Both cases can be found in our previous polarization conversion model [Eq. (27)], where the band structure is symmetric and linear about both $\tilde{\theta} = 0$ and $\tilde{\theta} = \pi$, and has a Dirac point at $\tilde{\theta} = 0$, resulting in a non-vanishing power $\partial_{\Delta\phi}\epsilon_{1,2}|_{\Delta\phi=0}$. For $\tilde{\theta}=\pi$, the power vanishes while retaining its symmetry and linearity about this point. Consequently, the model obtains a HL scaling for coherent-state inputs even for a general asymmetric distribution $f(\phi)$ that requires degenerate critical points at $\theta \neq 0, \pi$ [Fig. 4.(c), (i): an initial phase difference $\phi_{20} - \phi_{10} = 0.6\pi$ is chosen for the coherent-state input]. For Fock-state inputs, this lifted restriction on θ also poses less constraints on the a priori knowledge of θ and results in a wider range of sub-SQL sensitivity in the spectrum [Fig. 4.(f)].

3. Example III: a specific driven qubit model

Finally, we consider the sensitivity of the parity measurement for a specific model given as

$$\hat{H}_{\phi}(t) = \frac{\omega_0}{2} \hat{\sigma}_z + \mathcal{A} \left[3\sin(\omega t + \phi_1) \hat{\sigma}_y + \sin(\omega t + \phi_2) \hat{\sigma}_x \right] + \mathcal{A} \left[\cos(\omega t + \phi_1) + 2\cos(\omega t + \phi_2) \right] \hat{\sigma}_z,$$
(34)

whose quasienergy bands are given in Fig. 3 and do not exhibit any degeneracy or symmetry. Specifically, its characteristic functions $\mathcal{G}_{nm}(\tilde{x},\tilde{\theta})$ only have non-degenerate critical points for any value of $\tilde{\theta}$. Consequently, the HL scaling is inaccessible for any type of inputs and the non-degenerate critical points can only give the SQL scaling [Fig. 4.(a), (d), (g)].

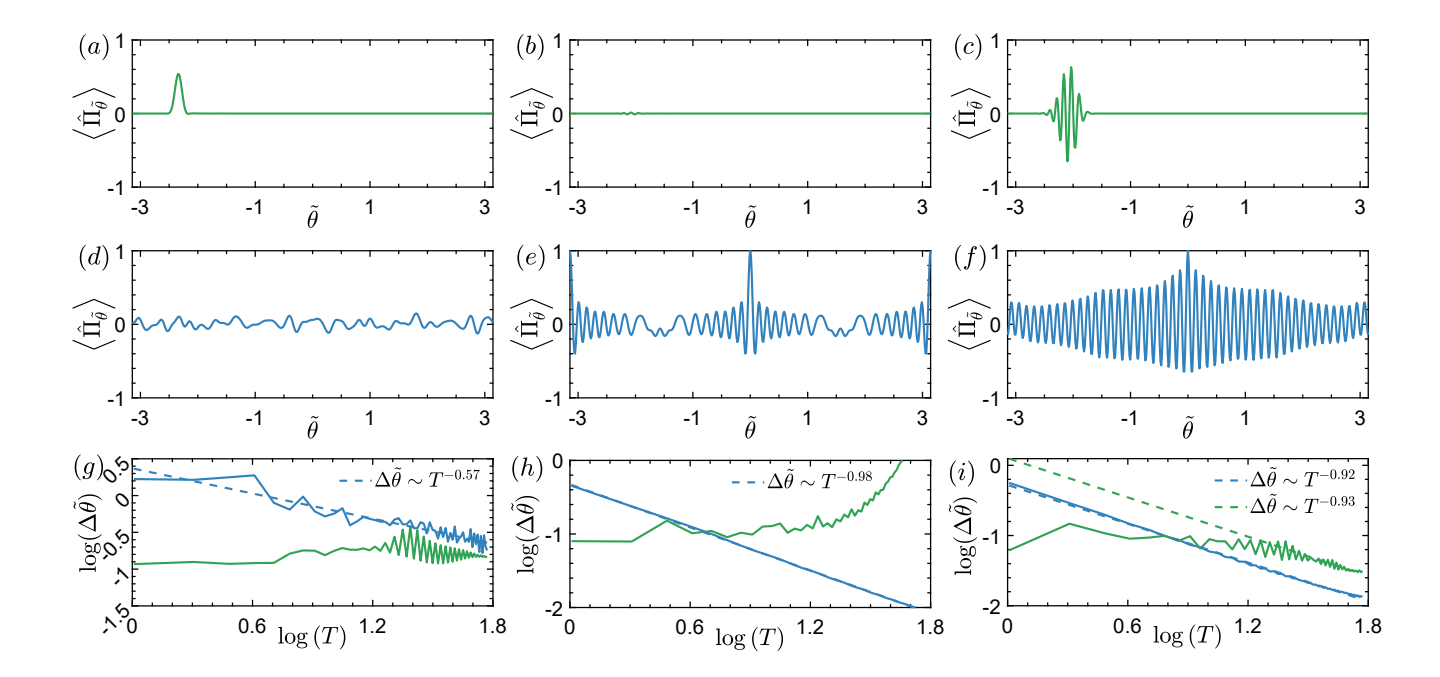


FIG. 4. Parity measurements and corresponding sensitivity for three models: (a)(d)(g) the specific model given in Eq. (34), (b)(e)(h) 2-level system with circularly-polarized drives and (c)(f)(i) polarization conversion. In (a)(b)(c), we plot the expectation value of the parity operator $\hat{\Pi}_{\tilde{\theta}}$ as a function of $\tilde{\theta}$ for coherent-state inputs. In (d)(e)(f), the same quantity is plotted for Fock-state inputs. The optimal sensitivity from the parity measurement for both inputs and all three models is given in (g)(h)(i), where the green (blue) curves and dashed green (blue) lines represent the sensitivity of coherent (Fock) inputs and their asymptotic scaling, respectively. The Heisenberg limit and the standard quantum limit are represented by slopes $\kappa = -1$ and $\kappa = -0.5$ in the log-log plot of sensistivity vs. interaction time (T). For all three models, we start with average 50 bosons in each drive. For coherent-state inputs, we introduce an initial phase difference $\phi_{20} - \phi_{10} = 0.6\pi$ between two drives. Other parameters in different models are given as follows: for the specific model given in Eq. (34), $\omega = \omega_0$, $\mathcal{A} = \frac{\omega_0}{2}$; for the 2-level system with circularly-polarized drives, $\omega = \frac{\omega_0}{4}$, $\mathcal{A} = \frac{\omega_0}{8}$; and for the polarization conversion, $\omega = \omega_0$, $\mathcal{A} = \frac{\omega_0}{2}$.

VI. PARTICLE LOSS AND A FINITE PHASE RANGE

In this section, we discuss the robustness of the PES's against loss in the interferometer and a finite (a priori) phase range $\delta\theta$. The mathematical tools employed are the Kraus representation for lossy dynamics and the Bayesian approach (App. H) for dealing with a finite (a priori) phase range.

A. Effects of particle loss

The first source of error arises from the potential loss of particles in the interferometer. We use Kraus operators [49, 51] to simulate such loss. To be specific, we consider an interferometer with one lossy arm (\hat{a}_1) and one lossless arm (\hat{a}_2) . We expect qualitatively similar behaviors when both arms are lossy. In the Kraus representation, the state after a lossy transmission line with transmissivity $\eta \in [0, 1]$ is given by:

$$\hat{\rho} = \sum_{j=0}^{+\infty} \hat{K}_j \hat{\rho}_0 \hat{K}_j^{\dagger}, \tag{35}$$

 $|\text{PES}\rangle_T \langle \text{PES}|_T$ and \hat{K}_{i} with \equiv $(1-\eta)^{\frac{j}{2}} \eta^{\frac{1}{2}\hat{a}_1^{\dagger}\hat{a}_1} \hat{a}_1^j / \sqrt{j!}$. Noting that $\eta = 1$ represents a perfect transmission with no boson loss while $\eta = 0$ stands for a complete loss of bosons. simulation is made for the polarization conversion model with 30 input bosons in each drive with identical frequencies $\omega_1 = \omega_2 = \omega_0$ and renormalized amplitudes $\mathcal{A} = \frac{\omega_0}{2}$. For the coherent-state input, we specify an initial phase difference $\phi_{20} - \phi_{10} = 0.6\pi$. The conversion time is chosen as $T = 32T_{\text{com}}$. In Fig. 5.(b), we plot the sensitivity $\Delta\theta$ both from the QFI (solid lines) and parity measurement (dashed lines) as a function of the transmissivity η for coherent-state inputs (green), Fock-state inputs (blue) and the NOON state (red). Typically, the QFIs for coherent-state and Fock-state inputs exhibit robustness against loss and present sub-SQL sensitivity even at $\eta = 0.5$. As comparison, the N00N state is much more fragile to loss and already goes beyond the SQL at $\eta \approx 0.91$. This is consistent

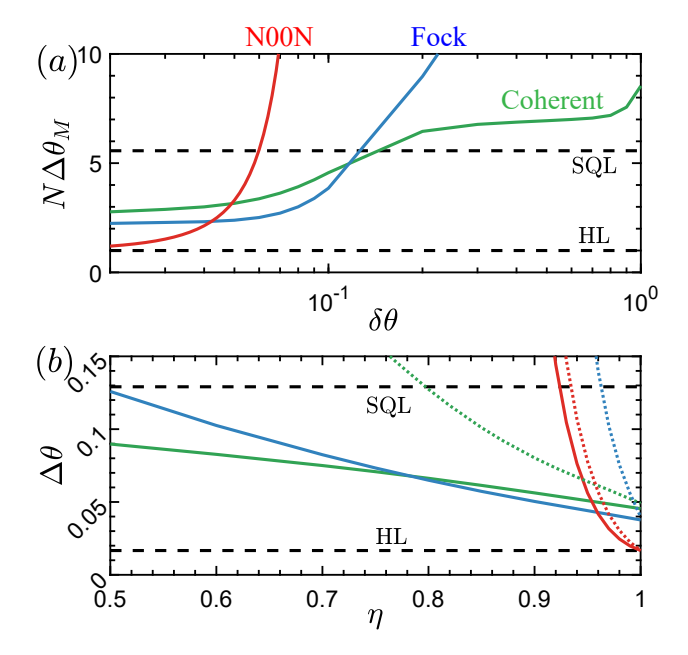


FIG. 5. Sensitivity under a priori phase uncertainties and lossy interferometry. (a) The improvement $\Delta\theta_m$ in Eq. (38) as a function of the a priori phase uncertainty $\delta\theta$ for coherent (green) and Fock (blue) inputs. The behavior of $\Delta\theta_m$ for the N00N state (red) is shown for comparison. The entangler is chosen as the polarization conversion model with $\omega=\omega_0$, $\mathcal{A}=\frac{\omega_0}{2}$ and 15 bosons in each mode initially. For the N00N state, we choose N=30. (b) The sensitivity $\Delta\theta$ from both the qCRB (solid) and parity measurement (dashed) for coherent-state (green) and Fock-state (blue) inputs. Again, we plot $\Delta\theta$ for the N00N state (red) for comparison. The model is the same as in (a), but with 30 bosons in each mode initially. For the N00N state, we choose N=60.

with the observation that entangled coherent states and $|N-m:m\rangle\equiv\frac{1}{\sqrt{2}}(|N-m,m\rangle+|m,N-m\rangle)$ with $1\leq m\leq N-1$ are, in general, more robust than the N00N state against loss [49]. The parity measurement, however, appears more sensitive to the lossy interferometer for all three kinds of states. Specifically, the parity measurement for the Fock-state input and N00N state performs worse than the SQL for $\eta<0.93$. The coherent-state input is more robust and its super-resolution survives up to $\eta\approx0.8$. However, this is still much worse than the QFI itself. As a result, we conclude that the PES's we generate are robust against loss themselves, while the parity measurement is less able to extract the QFI when there is significant loss.

When the loss is small, however, all PES's converge to almost the same sub-SQL sensitivity as a result of the linearity of the band [Fig. 2.(c)]. However, such sub-SQL sensitivity only applies for specific values of $\tilde{\theta}$ for a general field distribution $f(\phi)$. In Fig. 4.(c), (f), we plot the expectation value of the parity operator $\langle \hat{\Pi}_{\tilde{\theta}} \rangle$ for coherent-state inputs (c) and Fock-state inputs (f) at $\eta =$

1 as a function of $\tilde{\theta}$. For coherent-state inputs, the sub-SQL sensitivity only appears within a finite range of $\tilde{\theta}$, while Fock-state inputs are sub-SQL in a wider range. As seen earlier, this is an interplay between degenerate critical points of \mathcal{G} and initial field distributions $f(\phi)$. Consequently, when the transmission is perfect, one is, potentially, able to tailor the input $f(\phi)$ such that the range of $\tilde{\theta}$ exhibiting sub-SQL sensitivity is maximized.

B. Effects of a finite phase range

Another source of error comes from a finite (a priori) phase range $\delta\theta$. This phase uncertainty arises when a priori knowledge of its value is lacking. The quantity of interest now becomes the posterior variance, $\Delta_p\theta^2$ given in Eq. (H3), which one aims to minimize (App. H). Given the probe state as $|\psi\rangle_p$ ($\hat{\rho}_p$ for a mixed state) and the phase imprinting unitary as $\hat{\mathcal{U}}_{\theta}$, one then needs to minimize $\Delta_p\theta^2$ over all possible POVM measurements. This challenging task is facilitated by the work done in [65], which narrows the infinitely many possililities down to projective measurements $\{|\mu\rangle\langle\mu|\}$ with outcome μ satisfying $\sum |\mu\rangle\langle\mu| = \hat{\mathbb{1}}_0$. The projective measurement can hence be described by a hermitian operator

$$\hat{S} = \sum_{\mu} \mu |\mu\rangle \langle \mu|. \tag{36}$$

The task now becomes finding the optimal \hat{S} that minimizes $\Delta_{\rm p}\theta^2$. Denoting the probe state after the phase imprinter as $\hat{\rho}_{\theta} = \hat{\mathcal{U}}_{\theta}\hat{\rho}_{\rm p}\hat{\mathcal{U}}_{\theta}^{\dagger}$, such a minimization is realized by choosing [78]

$$\hat{S} = 2 \sum_{k,l,\lambda_k + \lambda_l > 0} \frac{\langle k | \overline{\rho} | l \rangle}{\lambda_k + \lambda_l} |k\rangle \langle l|, \qquad (37)$$

where λ_k and $|k\rangle$ are eigenvalues and eigenstates of the θ -averaged mixed state $\rho \equiv \int d\theta P(\theta) \, \hat{\rho}_{\theta}$ and $\bar{\rho} \equiv \int d\theta P(\theta) \, \hat{\rho}_{\theta} \, \theta$. The upper bound $\Delta \theta_m^2$ of optimization from the measurement is now given as the difference between the inverse of the minimal posterior variance $\Delta_p \theta^2$ and the a priori classical CRB of the a priori phase distribution $\frac{1}{F_0}$ as [48]:

$$\frac{1}{\Delta\theta_m^2} = \frac{1}{\Delta_p \theta^2} - \frac{1}{F_0}.$$
 (38)

The HL and SQL are now defined with respect to $\Delta\theta_m$. Numerically, we again choose the polarization conversion model Eq. (27) with 15 bosons in each drive with identical frequencies $\omega_1 = \omega_2 = \omega_0$ and renormalized amplitudes $\mathcal{A} = \frac{\omega_0}{2}$. As before, we specify an initial phase difference $\phi_{20} - \phi_{10} = 0.6\pi$ for the coherent-state input. The probe state $|\text{PES}\rangle_T$ is obtained at $T = 8T_{\text{com}}$. In

Fig. 5.(a), we plot $\Delta\theta_m$ as a function of the a priori uncertainty $\delta\theta$ for coherent-state inputs (green), Fock-state inputs (blue) and the N00N state (red) upon assuming a Gaussian distribution

$$P(\theta) = \frac{1}{\sqrt{2}\delta\theta} \exp\left(-\frac{\theta^2}{2\delta\theta^2}\right) \tag{39}$$

of the uncertain phase [48]. For small a priori uncertainty $\delta\theta < 0.1$, the PES's exhibit sub-SQL sensitivity and go beyond the SQL when $\delta\theta > 0.2$ for both coherent-state and Fock-state inputs. Meanwhile, the N00N state is less effective to the finite a priori distribution $\delta\theta$ and performs worse than the SQL for $\delta\theta > 0.06$. The PES's generated by our Floquet entangler are hence ineffective when trying to measure a phase that has a non-local a priori uncertainty. The advantage that entangled states have when measuring a minuscule phase shift require some prior knowledge of the vicinity scrutinized, but this results in poor performance when such knowledge is absent (cf Ref. [11]).

VII. EXPERIMENTAL CONSIDERATIONS

In this section, we propose an experiment that realizes our Floquet quantum sensor. After discussing general experimental considerations, we will propose a superconducting circuit realization. As discussed in Sec. IV B. the prerequisite of the path entanglement is a dispersive quasienergy band structure that depends on initial phases ϕ_1, ϕ_2 of two drives. Given the quasienergies evaluated and periodic in the driving frequency $\omega_{1,2}$, the amplitudes of drives should hence be comparable to these frequencies. In the quantized model [Eq. (15)], this requires the normalized coupling $\hat{H}_{1/2,0/e}^c$ to be comparable to $\omega_{1,2}$, posing significant constraints when the drives are conventional optical cavities (Fabry-Perot cavity, microsphere cavity, etc), where the frequency (> 100THz) is much larger than their typical coupling (< 1GHz) to matter [79–81]. Energy transfer in such cavities typically requires $N > 10^{10}$ particles for enhancement.

To lower this bound on the number of particles, we suggest using microwave cavities (coplanar waveguide resonator, LC resonator, etc.) with significantly smaller frequencies $\omega \sim 1-10 \mathrm{GHz}$ [82, 83], which couple to superconducting qubits in a controllable way. Based on our protocol for generating PES's, the interaction time between the qubit and cavities needs to be shorter than the relaxation time t_1 and dephasing time t_2 of the qubit (given the Q-factor of the two resonators is high enough). Consequently, the frequency of the resonators is lower-bounded by the inverse of the coherence time as $\omega \gg \frac{1}{t_{1,2}}$ (this also implies that qubits with long coherence times

are preferred). Assuming these conditions are satisfied, we now discuss a potential realization of Floquet entanglers in superconducting circuits.

To be concrete, we choose the polarization conversion model [Eq. (27)] as an example. In this case, we apply both current and voltage drives on the qubit as [Fig. 6.(b)]

$$\hat{H}(t) = \frac{\omega_q}{2}\hat{\sigma}_z + I(t)\hat{\sigma}_x + V(t)\hat{\sigma}_y, \tag{40}$$

with the current drive $I\left(t\right)=2\mathrm{Re}\left\{e^{i\omega_{q}t}\left[\frac{\omega_{0}}{2}+\mathcal{A}\cos\left(\omega t+\phi_{1}\right)+\mathcal{A}\cos\left(\omega t+\phi_{2}\right)\right]\right\}$ and the voltage drive $V\left(t\right)=2\mathcal{A}$. Re $\left\{e^{i\omega_{q}t}\left[\sin\left(\omega t+\phi_{1}\right)-\sin\left(\omega t+\phi_{2}\right)\right]\right\}$. By moving to a rotating frame with $\hat{U}\left(t\right)=e^{-i\frac{\omega_{q}t}{2}\hat{\sigma}_{z}}$ and a following rotating-wave approximation [84], the interaction Hamiltonian becomes the Floquet one in Eq. (27).

Following the logic of Sec. IV, the model with quantum drives can be realized by coupling the qubit and cavities in a time-dependent way:

$$\hat{H}(t) = \frac{\omega_q}{2} \hat{\sigma}_z + \omega \left(\hat{a}_1^{\dagger} \hat{a}_1 + \hat{a}_2^{\dagger} \hat{a}_2 \right)$$

$$+ 2\mathcal{A}\cos(\omega_q t) \left[\frac{\hat{a}_1 - \hat{a}_1^{\dagger}}{2i} - \frac{\hat{a}_2 - \hat{a}_2^{\dagger}}{2i} \right] \hat{\sigma}_y$$

$$+ 2\cos(\omega_q t) \left[\frac{\omega_0}{2} + \mathcal{A} \frac{\hat{a}_1 + \hat{a}_1^{\dagger}}{2} + \mathcal{A} \frac{\hat{a}_2 + \hat{a}_2^{\dagger}}{2} \right] \hat{\sigma}_x.$$

$$(41)$$

Similarly, by moving to the rotating frame with $\hat{U}(t)$ and keeping non-oscillating terms only, one obtains Eq. (27) with quantum drives in the interaction picture. We now show how such a Hamiltonian can potentially be realized in a superconducting circuit. We split our discussion on elements [Fig. 6.(a)] in the superconducting circuit and leave a detailed analysis of the circuit to App. I. See Fig. 6.(c) for a simplified version.

A. Superconducting qubit and cavities

Superconducting-circuit qubits [Fig. 6.(a)] are formed by truncating Josephson-junction based oscillators to the lowest two energy levels with gaps ranging from $1 \, \mathrm{GHz} < \omega_q < 20 \, \mathrm{GHz}$ [79, 85], which are assumed to be separated from higher excited levels [85]. For two-tone Floquet Hamiltonians, excitation to higher energy levels changes the energy transfer, and hence the path entanglement, completely. With this in mind, qubits with large anharmonicity are preferred. We hence suggest flux or fluxonium-like designs, which provide a large energy gap (> 20 \, \mathrm{GHz}) between two lowest energy levels and higher ones [86] and coherence times as long as $100 \sim 400 \mu s$ [87, 88].

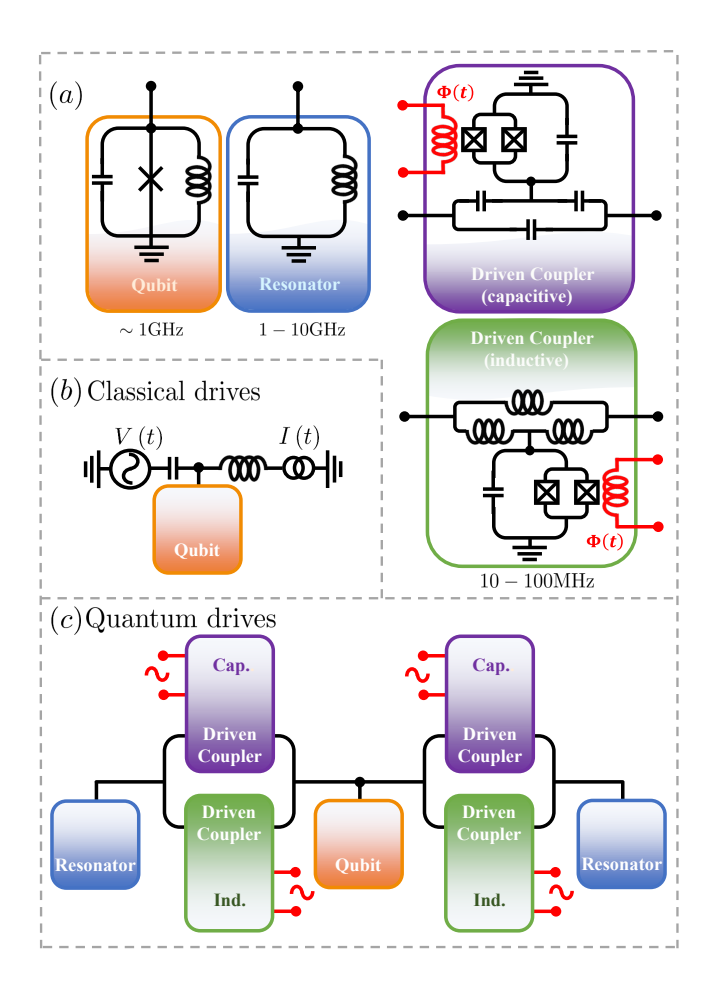


FIG. 6. Superconducting circuit realization for Eq. (41). (a) A table of superconducting elements in the circuit: the circuit diagram includes a flux qubit, an LC resonator, and two types of driven (tunable) couplers. The tunability arises from an indirect coupling to an idler mode, whose frequency is adjusted by the external flux $\Phi(t)$. The energy scales of these elements in current experiments are listed below. (b) A schematic circuit implementing Eq. (40) where the qubit is driven by a voltage source V(t) and a current source I(t). Proper grounding of the qubit is assumed. (c) A schematic circuit for Eq. (41), where the qubit is coupled to two resonators via tunable couplers (variable capacitors and inductors), with typical realizations shown in (a). Proper grounding of all circuit elements is again assumed.

We couple the qubit to two cavities. In order to obtain dispersive quasienergy bands with relatively small number of bosons, we suggest microwave cavities with close frequencies and coupling strengths. Two such examples are the coplanar waveguide resonator ($\omega \approx 1-10 {\rm GHz}$, $\frac{g}{2\pi} > 300 {\rm MHz}$ and $Q > 10^8$) and the LC resonator ($\omega \approx 1-10 {\rm GHz}$, $\frac{g}{2\pi} = 0.1-1 {\rm GHz}$ and $Q \sim 10^3$) in Fig. 6.(a).

B. Tunable coupler and qubit drive

The most nontrivial step in shaping Eq. (41) is the time-dependent coupling $A\cos(\omega_a t)$ between the qubit and resonators. This requires variable capacitors and inductors whose capacitance $C(t) = C_0 \cos(\omega_q t)$ and inductance $L(t) = L_0 \cos(\omega_q t)$ are tuned periodically in a superconducting environment. There are existing ways to realize such variable couplings [89-94], one of which is indirectly coupling the qubit and resonators by an idler qubit/cavity [92, 95], whose frequency is significantly larger than those of the qubit and resonators. The idler qubit/cavity remains in its ground state. However, by changing an external flux, one tunes its frequency in a controllable way, which effectively gives a time-dependent coupling after integrating out such idler degrees of freedom [Fig. 6.(a)]. The same principle underlies other tunable couplers like Delft couplers and Gmon couplers.

Another time dependence in Eq. (41) is in the term $\omega_0 \cos(\omega_q t) \hat{\sigma}_x$, which gives rise to the qubit energy in the rotating frame. This is typically realized by coupling the qubit to a current source $I_d(t)$ inductively or a voltage $V_d(t)$ source capacitively (App. I).

Finally, we estimate the number of bosons one needs to use for a given design of the circuit in order to have a dispersive spectrum. As mentioned earlier, this requires that the normalized amplitudes of the drives [Eq. (15)] comparable to the frequency of the bosons $\sqrt{N}\mathcal{A}\approx\omega$, which gives a rough number of bosons one need to have in the experiments as $N\approx\left(\frac{\omega}{\mathcal{A}}\right)^2$. Consequently, for an effective coupling $\mathcal{A}\approx 100\mathrm{MHz}$ and resonator frequency $\omega\approx 1\mathrm{GHz}$ [Fig. 6.(a)], one needs roughly > 100 bosons in the cavity. To further decrease the number of bosons, stronger couplings and cavities with longer wave-lengths are suggested. On the other hand, for two-tone Floquet models with simpler couplings and are realizable in the original picture (i.e. without moving to a rotating frame), direct couplings between the qubit and resonators can reach to as large as $\frac{g}{2\pi}>800\mathrm{MHz}$ [83] that lowers the bound on the number of bosons significantly.

C. Phase imprinter and parity measurement

The phase imprinter and parity measurement for a cavity mode can both be implemented by coupling to another qubit dispersively via $\hat{H}_{dis} = -\chi \hat{a}^{\dagger} \hat{a} \hat{\sigma}_z^{'}$ [76, 96]. Here, by 'dispersive', we do not refer to dispersive quasienergy bands, but rather a change in the frequency of the cavity when coupling to a qubit. We use a different notation for the Pauli matrices $\hat{\sigma}_{x,y,z}^{'}$ to distinguish this qubit from the ancilla qubit. The phase operation can be generated by evolving the cavity-qubit system for some time τ , yielding $\theta = -\chi \tau$. Here, a measurement on θ can be viewed as one on τ , given that the coupling strength χ is known, or as one on χ , if the evolution time τ is known. The parity measurement can be realized by first

coupling the probe qubit for $t=\frac{\pi}{\chi}$, where a contolled-phase gate $\hat{C}_{\pi}=|g\rangle\langle g|+e^{i\pi\hat{a}^{\dagger}\hat{a}}|e\rangle\langle e|$ is realized, with $|g\rangle$ and $|e\rangle$ representing the ground and excited states of the qubit. Next, by inserting \hat{C}_{π} between two $\frac{\pi}{2}$ pulses in a Ramsey-type interferometer, one encodes odd and even parities to the $|g\rangle$ and $|e\rangle$ states of the qubit [76]. A different realization of the parity measurement using no-photon measurements can be found in [77].

VIII. CONCLUSION & OUTLOOK

In this work, we demonstrate that energy transfer in two-tone Floquet systems can be utilized to generate path-entangled states (PES's) that exhibit sub-SQL in phase estimation. Classically, such energy transfer between drives with commensurate frequencies is described by power operators derived from the quasienergies and quasieigenstates of the Floquet Hamiltonians. In the quantum regime, a quantized-drives model is approximated by a lattice model, which is a direct sum of classical Floquet models with different initial phases. By initializing the qubit (qudit in App. E) properly, we obtain path-entangled states with phase sensitivity approaching the HL. For drives on a single qubit, we also give explicit lower- and upper-bounds on the corresponding QFI, which physically describes the square mean of energy transfer. We show by numerics that the above conclusions drawn from the lattice model are applicable to the original quantized-drives model.

For a standard parity readout in optical quantum sensors and superconducting platforms, we show that the path-entangled states of two driving modes with identical frequencies can reach the Heisenberg limit if its classical Floquet model has quasi-energy bands with degenerate critical points. We show both analytically and numerically that failing to satisfy either of these conditions (identical frequencies and degenerate critical points) leads to phase estimation with at most the SQL sensitivity. There is hence an open question of extracting the phase information (to the HL) encoded in driving modes with different frequencies or from non-degenerate quasienergy bands.

The effects of a finite a priori distribution of the phase and the robustness of our quantum sensor against loss are manifested in the study of uncertainty reduction by measurements and imperfect transmissions in the interferometer. Our numerical results show that the pathentangled states generated in our Floquet entangler are generally ineffective to an a priori phase distribution but more robust against imperfect transmissions. However, the parity measurement is less robust against loss in the interferometer, consistent with earlier observations that such measurement is no longer optimal for lossy interferometers [97]. Therefore, another natural future task is to find a better and more *experimental-friendly* decoding scheme in the presence of loss and a priori uncertainties. Ongoing efforts in these directions can be found in recent works [47, 98, 99].

It is now realized that, besides interferometric designs, some single-mode quantum states also exhibit phase sensitivity beyond the standard quantum limit (SQL) [96, 100]. We expect that our sensor design based on energy transfer can naturally apply to this new type of sensor by treating only one drive quantum-mechanically while the other remains classical [41]. It is important to note that for single-mode quantum sensing, different phase encoding and decoding schemes are required. Beyond quantum metrology, we anticipate that our twotone Floquet models can potentially be utilized in state preparation and engineering. An example of this is provided by the polarization conversion model [Eq. (27)], where the non-diffusive wavefunctions from the linearity of the bands suggest potential high-Fock state generation [Fig. 2.(i)]. We thus expect that state engineering can be further facilitated by band engineering and energy transfer in Floquet systems.

ACKNOWLEDGMENTS

We thank Tuvia Geven and Frederick Nathan for insightful discussions. We acknowledge the support of the Institute for Quantum Information and Matter, an NSF Physics Frontiers Center (PHY-2317110). AE acknowledges funding by the German National Academy of Sciences Leopoldina under the grant number LPDS 2021-02 and by the Walter Burke Institute for Theoretical Physics at Caltech. AR was supported by the Cluster of Excellence 'CUI: Advanced Imaging of Matter' of the Deutsche Forschungsgemeinschaft (DFG) (EXC 2056 and SFB925), and the Max Planck-New York City Center for Non-Equilibrium Quantum Phenomena. G.R. is grateful to AFOSR MURI program, under agreement number FA9550-22-1-0339, as well as to the Simons Foundation. Part of this work was done at the Aspen Center for Physics, which is supported by the NSF grant PHY-1607611.

Appendix A: Energy transfer and power operators - classical driving fields

In this appendix, we prove useful properties of the power operator in a quantum system driven by two classical fields. As in the main text, we assume that our system is a two-tone Floquet model defined in a finite-dimensional Hilbert space of dimension d. It is governed by a Hamiltonian of the form

$$\hat{H}(t) = \hat{H}_0 + \hat{H}_1(\omega_1 t + \phi_1) + \hat{H}_2(\omega_2 t + \phi_2), \tag{A1}$$

with H_0 a static contribution and \hat{H}_i ($\omega_i t + \phi_i$) periodically driven parts with drive frequencies ω_i and initial phases ϕ_i (i=1,2). In order to obtain a Floquet system, we assume that the frequencies are commensurate, i.e. $\omega_1/\omega_2 \in \mathbb{Q}$ is rational, and there exists a time T_{com} (the least common multiple of $T_1 = 2\pi/\omega_1$ and $T_2 = 2\pi/\omega_2$) such that $\hat{H}(t) = \hat{H}(t + T_{\text{com}})$. We further assume that H_i are differentiable (operator-valued) functions of ϕ_i (i=1,2).

First, we show that, at stroboscopic times $T = kT_{\text{com}}$ $(k \in \mathbb{Z})$, the power operator $\hat{P}_j(T)$ takes the compact form as $\hat{P}_j \equiv \sum_{n=1}^d \left(\partial_{\phi_j} \epsilon_n \right) |n\rangle \langle n|$. To this end, we first rewrite the unitary evolution operator $\hat{\mathcal{U}}(T) = \mathcal{T}e^{-i\int_0^T \hat{H}(t)dt}$ in its eigenbasis

$$\hat{\mathcal{U}}(T) = \sum_{n=1}^{d} e^{-i\epsilon_n T} |n\rangle \langle n|$$
(A2)

where ϵ_n and $|n\rangle$ are quasi-eigenenergies and quasi-energies eigenstates of the effective Floquet Hamiltonian $\hat{H}_{eff} = i/T_{\text{com}} \log \hat{\mathcal{U}}(T_{\text{com}})$. We note that both $\epsilon_n = \epsilon_n(\phi_{1,2}, \omega_{1,2})$ and $|n\rangle = |n(\phi_{1,2}, \omega_{1,2})\rangle$ are dependent on the phases $\phi_{1,2}$ and frequencies $\omega_{1,2}$, but are independent of T. The power operator can hence be written as

$$\hat{P}_{j}(T) = \frac{i}{T}\hat{\mathcal{U}}^{\dagger}(T)\,\partial_{\phi_{j}}\hat{\mathcal{U}}(T) \tag{A3}$$

$$= \sum_{n=1}^{d} \left(\partial_{\phi_j} \epsilon_n \right) |n\rangle \langle n| + \frac{i}{T} \sum_{n=1}^{d} \left(1 - e^{2i\epsilon_n T} \right) |n\rangle \langle n| \partial_{\phi_j} \left(|n\rangle \langle n| \right). \tag{A4}$$

Noting that $\| (1 - e^{2i\epsilon_n T}) |n\rangle \langle n| \partial_{\phi_j} (|n\rangle \langle n|) \|$ is bounded by a time-independent constant, we recover \hat{P}_j , as defined in the main text, in the limit $T \to \infty$.

Second, we prove that Tr $\left[\hat{P}_{j}\right]=0$. This follows from its definition via

$$\operatorname{Tr}\left[\hat{P}_{j}\right] = i \lim_{T \to \infty} \frac{1}{T} \operatorname{Tr}\left[\hat{\mathcal{U}}^{\dagger}\left(T\right) \partial_{\phi_{j}} \hat{\mathcal{U}}\left(T\right)\right] \tag{A5}$$

$$= \lim_{T \to \infty} \frac{1}{\omega_j T} \int_0^T dt \operatorname{Tr} \left[\hat{\mathcal{U}}^{\dagger} \left(t \right) \frac{d\hat{H}_j}{dt} \hat{\mathcal{U}} \left(t \right) \right]$$
 (A6)

$$= \lim_{T \to \infty} \frac{1}{\omega_j T} \int_0^T dt \operatorname{Tr} \left[\frac{d\hat{H}_j}{dt} \right]$$
 (A7)

$$= \lim_{T \to \infty} \frac{1}{\omega_j T} \operatorname{Tr} \left[\hat{H}_j(T) - \hat{H}_j(0) \right]$$
(A8)

$$=0. (A9)$$

Finally, we show $\sum_j \omega_j \hat{P}_j = 0$, which physically is a restatement of the energy conservation: the system can only restore a finite amount of energy. Therefore, over long periods of time T, there is no net flow of energy in or out. To see this, we again start from the definition of \hat{P}_j and expand as:

$$\sum_{i} \omega_{j} \hat{P}_{j} = \lim_{T \to \infty} \frac{i}{T} \sum_{i} \hat{\mathcal{U}}^{\dagger} (T) \, \omega_{j} \partial_{\phi_{j}} \hat{\mathcal{U}} (T) \tag{A10}$$

$$= \lim_{T \to \infty} \frac{1}{T} \int_0^T dt \ \hat{\mathcal{U}}^{\dagger}(t) \left[\sum_j \frac{d\hat{H}_j}{dt} \right] \hat{\mathcal{U}}(t)$$
(A11)

$$= \lim_{T \to \infty} \frac{1}{T} \int_{0}^{T} dt \, \hat{\mathcal{U}}^{\dagger}(t) \, \frac{d\hat{H}(t)}{dt} \hat{\mathcal{U}}(t) \tag{A12}$$

$$= \lim_{T \to \infty} \frac{1}{T} \hat{\mathcal{U}}^{\dagger}(t) \, \hat{H}(t) \, \hat{\mathcal{U}}(t) \,|_{0}^{T} - \lim_{T \to \infty} \frac{1}{T} \int_{0}^{T} dt \, \frac{d\hat{\mathcal{U}}^{\dagger}(t)}{dt} \, \hat{H}(t) \, \hat{\mathcal{U}}(t) - \lim_{T \to \infty} \frac{1}{T} \int_{0}^{T} dt \, \hat{\mathcal{U}}^{\dagger}(t) \, \hat{H}(t) \, \frac{d\hat{\mathcal{U}}(t)}{dt} \quad (A13)$$

$$= \lim_{T \to \infty} \frac{1}{T} \hat{\mathcal{U}}^{\dagger}(t) \, \hat{H}(t) \, \hat{\mathcal{U}}(t) \,|_{0}^{T} - i \lim_{T \to \infty} \frac{1}{T} \int_{0}^{T} dt \, \hat{\mathcal{U}}^{\dagger}(t) \, \left[\hat{H}(t) \,, \hat{H}(t) \right] \hat{\mathcal{U}}(t)$$

$$= 0, \tag{A14}$$

where from the third to fourth line we have integrated by parts, and from the last second to last line we have used the fact that $\hat{H}(t)$ commutes with itself at any time t.

Appendix B: Energy transfer and power operators - quantized driving fields

In this part, we compute the long-time limit of the functional power operator $\hat{P}_j[f]$. As in the main text, we express operators and states in the (Fourier-transformed) phase space and move to the interaction picture defined by a unitary transform $\hat{U}(t) = e^{-i\hat{H}_B t}$. In the interaction picture, the dynamics of the combined system of qudit and quantum drives $i\partial_t |\Psi(t)\rangle = \hat{H}_l(t) |\Psi(t)\rangle$ is decomposed into that of each phase component $i\partial_t |\psi(\phi,t)\rangle = \hat{H}_\phi(t) |\psi(\phi,t)\rangle$ [Eq. (16) and discussion below]. At stroboscopic moments $T = kT_{\text{com}}$, with k an integer, such time evolution can be expressed in terms of Floquet modes as:

$$|\psi(\phi,T)\rangle = \sum_{n=1}^{d} c_n e^{-i\epsilon_n T} |n\rangle,$$
 (B1)

where ϵ_n and $|n\rangle$ are quasi-eigenenergies and quasi-energies eigenstates of the effective Floquet Hamiltonian $\hat{H}_{eff} = i/T_{\text{com}} \log \mathcal{U}(\hat{T}_{\text{com}})$. $c_n = \langle n | \psi\left(\phi,0\right) \rangle$ are initial overlaps between $|\psi\left(\phi,0\right)\rangle$ and $|n\rangle$. In this work, we assume the initial state being a direct product between the qudit and driving modes, giving $|\psi\left(\phi,0\right)\rangle = |\psi\left(0\right)\rangle$ at t=0. However, it should be clear that all other quantities c_n , ϵ_n , and $|n\rangle$ depend on ϕ implicitly and we drop such dependence to simplify the notation. The stroboscopic dynamics of the full state $|\Psi\left(T\right)\rangle$ becomes a superposition of $|\psi\left(\phi,T\right)\rangle\otimes|\phi\rangle$ as:

$$|\Psi(T)\rangle = \sum_{n=1}^{d} \int_{BZ} d^{2}\phi f(\phi) c_{n} e^{-i\epsilon_{n}T} |n\rangle \otimes |\phi\rangle.$$
 (B2)

We next evaluate $\overline{P}_{j}\left(T\right)$ for the evolved state:

$$\overline{P}_{j}\left(T\right) = \frac{1}{T} \left(\left\langle \hat{a}_{j}^{\dagger} \hat{a}_{j} \right\rangle_{0} - \left\langle \hat{a}_{j}^{\dagger} \hat{a}_{j} \right\rangle_{T} \right). \tag{B3}$$

Here, we use $\langle \Box \rangle_0 = \langle \Psi (0) | \Box | \Psi (0) \rangle$ and $\langle \Box \rangle_T = \langle \Psi (T) | \Box | \Psi (T) \rangle$ to abbrievate expectation values of \Box at t=0 and t=T, respectively. Noting that the number operator $\hat{a}_j^{\dagger}\hat{a}_j$ of the j-th drive, as the canonical quadrature of the j-th phase ϕ_j , becomes $\hat{a}_j^{\dagger}\hat{a}_j = -i\partial_{\phi_j}$ in the phase space, we can calculate Eq. (B3) term by term:

$$\langle \hat{a}_{j}^{\dagger} \hat{a}_{j} \rangle_{0} = \int_{\text{BZ}} d^{2} \bar{\phi} d^{2} \phi f^{*} \left(\bar{\phi} \right) f \left(\phi \right) \langle \psi \left(\bar{\phi}, 0 \right) | \psi \left(\phi, 0 \right) \rangle \langle \bar{\phi} | \frac{\partial_{\phi_{j}}}{i} | \phi \rangle$$
(B4)

$$= i \int_{\mathrm{BZ}} d^{2} \phi f^{*} (\phi) \, \partial_{\phi_{j}} f (\phi) + i \int_{\mathrm{BZ}} d^{2} \phi |f (\phi)|^{2} \langle \psi (\bar{\phi}, 0) |\partial_{\phi_{j}} |\psi (\phi, 0) \rangle$$
 (B5)

$$=i\int_{\mathrm{BZ}} d^{2}\phi f^{*}\left(\phi\right) \partial_{\phi_{j}} f\left(\phi\right),\tag{B6}$$

where from the 1-st to 2-nd line we have integrated by parts, and from the 2-nd to 3-rd line we have used that $\partial_{\phi_j} |\psi(\phi, 0)\rangle = 0$ given the assumption (see Sec. IV) that the initial state is a product state between the system and drives.

We next calculate the second contribution $\langle \hat{a}_j^{\dagger} \hat{a}_j \rangle_T$ in Eq. (B3). After integrating by parts, it takes exactly the same form as the expansion for $\langle \hat{a}_j^{\dagger} \hat{a}_j \rangle_0$:

$$\langle \hat{a}_{j}^{\dagger} \hat{a}_{j} \rangle_{T} = i \int_{BZ} d^{2} \phi f^{*} (\phi) \partial_{\phi_{j}} f (\phi) + i \int_{BZ} d^{2} \phi |f (\phi)|^{2} \langle \psi (\phi, T) |\partial_{\phi_{j}} |\psi (\phi, T) \rangle.$$
 (B7)

Notably, the first term comes from the initial field distribution of the drives and cancels exactly the same contribution from $\langle \hat{a}_{j}^{\dagger} \hat{a}_{j} \rangle_{0}$. The non-trivial contribution comes from the second integral in Eq. (B7):

$$\Delta N_{j}(T) = i \int_{BZ} d^{2}\phi \left| f(\phi) \right|^{2} \left\langle \psi(\phi, T) \left| \partial_{\phi_{j}} | \psi(\phi, T) \right\rangle, \tag{B8}$$

which measures the difference between the average boson number $\langle \hat{a}_j^{\dagger} \hat{a}_j \rangle_T$ at moment t=T and initial boson number $\langle \hat{a}_j^{\dagger} \hat{a}_j \rangle_0$ at t=0. At stroboscopic times, expanding $|\psi\left(\phi,T\right)\rangle$ in terms of quasi-eigenenergies and quasi-energies eigenstates [Eq. (B1)], we can rewrite the average power input from the j-th drive as:

$$\overline{P_j}(T) = -\frac{\Delta N_j(T)}{T} \tag{B9}$$

$$= \sum_{n=1}^{d} \int_{BZ} d^{2}\phi |f(\phi)|^{2} |c_{n}|^{2} \partial_{\phi_{j}} \epsilon_{n} - \frac{i}{T} \sum_{n=1}^{d} \int_{BZ} d^{2}\phi |f(\phi)|^{2} c_{n}^{*} \partial_{\phi_{j}} c_{n}$$
(B10)

$$-\frac{i}{T} \sum_{m,n=1}^{d} \int_{PZ} d^{2}\phi \left| f(\phi) \right|^{2} c_{m}^{*} c_{n} e^{-i(\epsilon_{n} - \epsilon_{m})T} \left\langle m | \partial_{\phi_{j}} | n \right\rangle. \tag{B11}$$

Noting that both $\|\sum_{n=1}^{d} \int_{\mathrm{BZ}} d^2 \phi |f(\phi)|^2 c_n^* \partial_{\phi_j} c_n\|$ and $\|\sum_{m=1}^{D} \sum_{n=1}^{d} \int_{\mathrm{BZ}} |f(\phi)|^2 c_m^* c_n e^{-i(\epsilon_n - \epsilon_m)T} \langle m|\partial_{\phi_j}|n\rangle\|$ are bounded by T-independent constants, the contributions from them in $\overline{P_j}(T)$ henceforth scales as $O\left(\frac{1}{T}\right)$ and can be ignored when taking the limit $T \to \infty$. We hence conclude that $\overline{P_j}(T)$ has a finite, well-defined limit:

$$\lim_{T \to \infty} \overline{P_j}(T) = \sum_{n=1}^d \int_{\mathrm{BZ}} d^2 \phi |f(\phi)|^2 |c_n|^2 \partial_{\phi_j} \epsilon_n$$
 (B12)

$$= \langle \psi(0) | \hat{P}_i[f] | \psi(0) \rangle, \tag{B13}$$

with the functional operator defined as $\hat{P}_j[f] \equiv \sum_{n=1}^d \int_{\mathrm{BZ}} d^2\phi \, |f(\phi)|^2 \, (\partial_{\phi_j} \epsilon_n) \, |n\rangle \, \langle n|$. Physically, it can be viewed as a superposition of the power operators $\hat{P}_j = \sum_{n=1}^d \left(\partial_{\phi_j} \epsilon_n\right) |n\rangle \, \langle n|$ for the two-tone Floquet Hamiltonian, whose coefficient $|f(\phi)|^2$ is given by the initial field distributions in two drives. Without any ambiguity, we henceforth call it the 'functional power operator' for quantized driving fields.

The tracelessness and energy conservation of $\hat{P}_j[f]$ then follow easily from those of \hat{P}_j , which are proven in App. A.

Appendix C: Bounds on the quantum Fisher information

In this appendix, we prove that the quantum Fisher information of the path-entangled state Eq. (21) grows quadratically in time. We start with a general discussion on an ancilla qudit with dimension d, and specify to an ancilla qubit d = 2 later.

For a d-dimensional Floquet system, the power operator for the *j*-th drive is given as $\hat{P}_j = \sum_{n=1}^d \left(\partial_{\phi_j} \epsilon_n \right) |n\rangle \langle n|$ [Eq. (A4)], from which the functional power operator follows as

$$\hat{P}_{j}[f] = \sum_{n=1}^{d} \int_{BZ} d^{2}\phi |f(\phi)|^{2} (\partial_{\phi_{j}} \epsilon_{n}) |n\rangle \langle n|.$$
(C1)

The tracelessness of $\hat{P}_j[f]$ now ensures two disjoint sets $\mathcal{W}_{\pm}[f]$ of eigenvalues, containing positive and negative eigenvalues, respectively. Denoting eigenvalues of $\mathcal{W}_{\pm}[f]$ as $\{P_{\pm,k}[f]\}$, the tracelessness can be written as

 $\sum_{k=1}^{W_{+}[f]} P_{+,k}\left[k\right] + \sum_{l=1}^{W_{-}[f]} P_{-,l}\left[l\right] = 0 \text{ where } W_{\pm}\left[f\right] \text{ are cardinalities of } \mathcal{W}_{\pm}\left[f\right]. \text{ Further denoting the eigenstates of } P_{\pm,k}\left[f\right] \text{ as } |\pm,k\rangle_{f}, \text{ we define the initial qudit state as}$

$$|\beta, +\rangle_f = \frac{1}{\sqrt{W_+[f] + W_-[f]}} \left[\sum_{k=1}^{W_+[f]} e^{i\beta_k^{(+)}} |+, k\rangle_f + \sum_{l=1}^{W_-[f]} e^{i\beta_l^{(-)}} |-, l\rangle_f \right]. \tag{C2}$$

where $e^{i\beta_k^{(\pm)}}$ are arbitrary phase factors that satisfy $\langle \beta, +|_f \hat{P}_j[f] | \beta, +\rangle_f = 0$. We therefore have $D = W_+[f] + W_-[f] - 1$ independent phases $\left\{\beta_1^{(+)}, ..., \beta_{W_+[f]-1}^{(+)}, \beta_1^{(-)}, ..., \beta_{W_-[f]}^{(-)}\right\}$. Following the discussion in Sec. IV B, we define the path-entangled state as the output of three successive procedures: 1. prepare the input ancilla state as $|\beta, +\rangle_f$, according to an initial field distribution $f(\phi)$; 2. evolve the ancilla-drives system according to the quantized-drives model $\hat{\mathcal{U}}(T) = e^{-i\hat{H}_l T}$ for some $T = kT_{\text{com}}$ [Eq. (16)]; 3. project the ancilla degrees of freedom back to the input $|\beta, +\rangle_f$ defined by the projection operator $\hat{\Pi}_\beta = |\beta, +\rangle_f \langle \beta, +|_f$. At stroboscopic moments, this procedure yields:

$$|\text{PES}\rangle_T = \frac{1}{\mathcal{N}_T} \hat{\Pi}_\beta \sum_{n=1}^d \int_{\text{BZ}} d^2 \phi f(\phi) u_n e^{-i\epsilon_n T} |n\rangle \otimes |\phi\rangle,$$
 (C3)

where $u_n = \langle n|\beta, +\rangle_f$ is the overlap between the input $|\beta, +\rangle_f$ and the *n*-th quasienergy eigenstate of the effective Floquet Hamiltonian [Eq. (16)]. The normalization factor can be calculated by requiring $\langle \text{PES}|_T \,\hat{\mathbb{1}} \, |\text{PES}\rangle_T = 1$:

$$\mathcal{N}_{T}^{2} = \sum_{m,n=1}^{d} \int_{D_{T}} d^{2}\phi \left| f(\phi) \right|^{2} u_{m}^{*} u_{n} e^{-i(\epsilon_{n} - \epsilon_{m})T} \left\langle m \right| \hat{\Pi}_{\beta} \left| n \right\rangle$$
 (C4)

$$= \sum_{m,n=1}^{d} \int_{BZ} d^{2}\phi |f(\phi)|^{2} |u_{m}^{*}u_{n}|^{2} e^{-i(\epsilon_{n} - \epsilon_{m})T}$$
(C5)

$$= \sum_{n=1}^{d} \int_{\mathrm{BZ}} d^2 \phi \left| f(\phi) \right|^2 \left| u_n \right|^4 + O\left(\frac{1}{\sqrt{T}}\right). \tag{C6}$$

where in the last line we have used the stationary phase approximation upon assuming non-degenerate $\epsilon_n - \epsilon_m$ on the support of $f(\phi)$, which scales as $O\left(T^{-\frac{w}{2}}\right)$ for a w-dimensional integral. Mathematically, such non-degenerate condition requires a non-vanishing Hessian Hess $[\epsilon_n - \epsilon_m] \neq 0$. We note that we obtain $1/\sqrt{T}$ in Eq. (C6) although expecting 1/T from naively using the stationary phase approximation of a (seemingly) two-dimensional integral. To see why the two-dimensional integral is effectively just one-dimensional, note the energy conservation property of the power operators $\omega_1 \hat{P}_1 + \omega_2 \hat{P}_2 = 0$ gives a constraint on the quasienergies as:

$$(\omega_1 \partial_{\phi_1} + \omega_2 \partial_{\phi_2}) \epsilon_n = 0 \tag{C7}$$

for n=1,...,d. As a result, the quasienergies $\epsilon_n\left(\tilde{x}\right)$ are only functions of $\tilde{x}\equiv\frac{1}{\sqrt{2}}\left(\frac{\phi_1}{\omega_1}-\frac{\phi_2}{\omega_2}\right)$ and do not depend on the other canonical coordinate $\tilde{y}\equiv\frac{1}{\sqrt{2}}\left(\omega_2\phi_1+\omega_1\phi_2\right)$. One can hence integrated out the \tilde{y} degrees of freedom for $m\neq n$ in Eq. (C5) as:

$$\sum_{m \neq n} \int_{\mathrm{RZ}} d^2 \phi |f(\phi)|^2 |u_m^* u_n|^2 e^{-i(\epsilon_n - \epsilon_m)T}$$
(C8)

$$= \sum_{m \neq n} \int d\tilde{x} \left(\int d\tilde{y} \left| f\left(\tilde{x}, \tilde{y}\right) \right|^2 \left| u_m^* u_n \right|^2 \right) e^{-i(\epsilon_n - \epsilon_m)T}, \tag{C9}$$

which reduces to a 1-dimensional stationary phase problem. The non-degenerate condition Hess $[\epsilon_n - \epsilon_m] \neq 0$ becomes $\partial_{\bar{x}}^2 (\epsilon_n - \epsilon_m) \neq 0$. From Eq. (C6), in the limit $T \to \infty$, the normalization factor converges to:

$$\mathcal{N}^2 \equiv \lim_{T \to \infty} \mathcal{N}_T^2 = \sum_{n=1}^d \int_{BZ} d^2 \phi |f(\phi)|^2 |u_n|^4.$$
 (C10)

To see a HL-scaling of the QFI, we now compute $\frac{1}{T^2}F_q\left[|\text{PES}\rangle_T, \hat{J}_z\right]$ and show it asymptotically takes a T-independent, positive value at $T \to \infty$. For a pure state, the QFI is simply 4 times the variance of the generator:

$$\frac{1}{T^2} F_q \left[| \text{PES} \rangle_T, \hat{J}_z \right] = \frac{4}{T^2} \left(\langle \hat{J}_z^2 \rangle_{\text{PES}} - \langle \hat{J}_z \rangle_{\text{PES}}^2 \right), \tag{C11}$$

with $\langle\Box\rangle_{\mathrm{PES}}$ the expectation value of \Box with respect to the normalized path-entangled state $|\mathrm{PES}\rangle_T$. Taking $\hat{J}_z = \frac{1}{2}\left(\hat{a}_1^{\dagger}\hat{a}_1 - \hat{a}_2^{\dagger}\hat{a}_2\right) = -\frac{i}{2}\left(\partial_{\phi_1} - \partial_{\phi_2}\right)$, we evaluate the Eq. (C11) term by term:

$$\frac{4}{T^2} \langle \hat{J}_z^2 \rangle_{\text{PES}} = \frac{4}{T^2} \langle \text{PES}|_T \hat{J}_z^2 | \text{PES} \rangle_T \tag{C12}$$

$$= -\frac{1}{T^2 \mathcal{N}_T^2} \sum_{m,n=1}^d \int_{\mathrm{RZ}} d^2 \bar{\phi} d^2 \phi f^* \left(\bar{\phi} \right) f \left(\phi \right) \left| u_m^* u_n \right|^2 e^{-i(\epsilon_n - \epsilon_m)T} \left\langle \bar{\phi} \middle| \partial_{\Delta \phi}^2 \middle| \phi \right\rangle \tag{C13}$$

$$= \frac{1}{\mathcal{N}_T^2} \sum_{m,n=1}^d \int_{\mathrm{BZ}} d^2 \phi \left| f(\phi) \right|^2 \left| u_m^* u_n \right|^2 \left[\partial_{\Delta \phi} \epsilon_n \right]^2 e^{-i(\epsilon_n - \epsilon_m)T} + O\left(\frac{1}{T}\right)$$
 (C14)

$$= \frac{1}{\mathcal{N}_T^2} \sum_{n=1}^d \int_{BZ} d^2 \phi \left| f(\phi) \right|^2 \left| u_n \right|^4 \left[\partial_{\Delta \phi} \epsilon_n \right]^2 + O\left(\frac{1}{\sqrt{T}}\right)$$
 (C15)

$$= \frac{1}{\mathcal{N}^2} \sum_{n=1}^{d} \int_{BZ} d^2 \phi \left| f(\phi) \right|^2 \left| u_n \right|^4 \left[\partial_{\Delta \phi} \epsilon_n \right]^2 + O\left(\frac{1}{\sqrt{T}}\right), \tag{C16}$$

with $\partial_{\Delta\phi} \equiv \partial_{\phi_1} - \partial_{\phi_2}$. From the 2-nd to 3-rd line we have integrated by parts, noting the fact that a factor of T comes out only if the partial derivatives are applied to the exponential $e^{-i(\epsilon_n - \epsilon_m)T}$. We also assume that we are observing the system for a sufficiently long time such that $T \gg |N_1 - N_2|$, where N_1 and N_2 are the initial numbers of bosons in two drives. This allows terms involving $\partial_{\Delta\phi} f(\phi)$ to be absorbed into $O\left(\frac{1}{T}\right)$. From the 3-rd to 4-th line we again use the stationary phase approximation and drop the fast-oscillating exponentials when $m \neq n$. Finally from the 4-th to the last line we have merged the T-dependent terms of \mathcal{N}_T into $O\left(\frac{1}{\sqrt{T}}\right)$. A similar calculation can be conducted for the second term:

$$\frac{2}{T} \langle \hat{J}_z \rangle_{\text{PES}} = \frac{2}{T} \langle \text{PES}|_T \, \hat{J}_z \, | \text{PES} \rangle_T \tag{C17}$$

$$= -\frac{i}{T\mathcal{N}_T^2} \sum_{m,n=1}^{d} \int_{BZ} d^2 \bar{\phi} d^2 \phi f^* \left(\bar{\phi}\right) f(\phi) \left|u_m^* u_n\right|^2 e^{-i(\epsilon_n - \epsilon_m)T} \left\langle \bar{\phi} |\partial_{\Delta \phi}| \phi \right\rangle$$
(C18)

$$= \frac{1}{\mathcal{N}_T^2} \sum_{m,n=1}^d \int_{BZ} d^2 \phi |f(\phi)|^2 |u_m^* u_n|^2 \left[\partial_{\Delta \phi} \epsilon_n\right] e^{-i(\epsilon_n - \epsilon_m)T} + O\left(\frac{1}{T}\right)$$
 (C19)

$$= \frac{1}{\mathcal{N}_T^2} \sum_{n=1}^a \int_{BZ} d^2 \phi |f(\phi)|^2 |u_n|^4 \left[\partial_{\Delta \phi} \epsilon_n\right] + O\left(\frac{1}{\sqrt{T}}\right)$$
 (C20)

$$= \frac{1}{\mathcal{N}^2} \sum_{n=1}^{d} \int_{BZ} d^2 \phi |f(\phi)|^2 |u_n|^4 [\partial_{\Delta \phi} \epsilon_n] + O\left(\frac{1}{\sqrt{T}}\right), \tag{C21}$$

where again we have used the stationary phase approximation to replace the double summation to a single one. Note that the expectation value of \hat{J}_z for the probe state $|\text{PES}\rangle_T$ after the projection $\hat{\Pi}_\beta$ does not vanish asymptotically in

general. To prove an asymptotically positive $\frac{1}{T^2}F_q\left[|\text{PES}\rangle_T, \hat{J}_z\right]$ at $T \to \infty$, one hence needs to prove the following proposition:

Proposition 1 (Asymptotic coefficient of QFI). For a path-entangled probe state defined in Eq. (C3), the following inequality holds:

$$\frac{1}{\mathcal{N}^2} \sum_{n=1}^{d} \int_{BZ} d^2 \phi \left| f(\phi) \right|^2 \left| u_n \right|^4 \left[\partial_{\Delta \phi} \epsilon_n \right]^2 \tag{C22}$$

$$\geq \left[\frac{1}{\mathcal{N}^2} \sum_{n=1}^{d} \int_{BZ} d^2 \phi \left| f(\phi) \right|^2 \left| u_n \right|^4 \left[\partial_{\Delta \phi} \epsilon_n \right] \right]^2, \tag{C23}$$

with $\sum_{n=1}^{d} |u_n|^2 = 1$, $\int_{BZ} d^2 \phi |f(\phi)|^2 = 1$, $\sum_{n=1}^{d} \int_{BZ} d^2 \phi |f(\phi)|^2 |u_n|^2 \partial_{\Delta \phi} \epsilon_n = 0$, and $\mathcal{N}^2 = \sum_{n=1}^{d} \int_{BZ} d^2 \phi |f(\phi)|^2 |u_n|^4$. The equality holds only if $\hat{P}_j[f] = 0$ for j = 1, 2, given the initial field distribution $f(\phi)$.

The constraint $\sum_{n=1}^{d} \int_{\mathrm{BZ}} d^2\phi |f(\phi)|^2 |u_n|^2 \partial_{\Delta\phi} \epsilon_n = 0$ comes from the definition of $|\beta, +\rangle_f$ such that $\langle \beta, +|_f \hat{P}_j[f] |\beta, +\rangle_f = 0$. We start with some manipulation of the above inequality. Using the positiveness of \mathcal{N}^2 , it is equivalent to prove the following inequality:

$$\sum_{n=1}^{d} \int_{BZ} d^{2}\phi |f(\phi)|^{2} |u_{n}|^{4} \sum_{n=1}^{d} \int_{BZ} d^{2}\phi |f(\phi)|^{2} |u_{n}|^{4} (\partial_{\Delta\phi} \epsilon_{n})^{2}$$
(C24)

$$\geq \left[\sum_{n=1}^{d} \int_{BZ} d^{2}\phi |f(\phi)|^{2} |u_{n}|^{4} \partial_{\Delta\phi} \epsilon_{n}\right]^{2}.$$
 (C25)

For two integrable functions $x(\phi), y(\phi)$, the integral form of Cauchy-Schwarz inequality states $\left[\int_{\mathrm{BZ}} d^2\phi \ x(\phi) \ y(\phi)\right]^2 \le \int_{\mathrm{BZ}} d^2\phi \ x^2(\phi) \int_{\mathrm{BZ}} d^2\phi \ y^2(\phi)$. By choosing $x(\phi) = |f(\phi)| \sqrt{\sum_{n=1}^d |u_n|^4}$ and $y(\phi) = |f(\phi)| \sqrt{\sum_{n=1}^d |u_n|^4 \left[\partial_{\Delta\phi} \epsilon_n\right]^2}$, we obtain:

$$\int_{BZ} d^{2}\phi |f(\phi)|^{2} \sum_{n=1}^{d} |u_{n}|^{4} \int_{BZ} d^{2}\phi |f(\phi)|^{2} \sum_{n=1}^{d} |u_{n}|^{4} (\partial_{\Delta\phi}\epsilon_{n})^{2} \ge \left\{ \int_{BZ} d^{2}\phi |f(\phi)|^{2} \sqrt{\left[\sum_{n=1}^{d} |u_{n}|^{4}\right] \left[\sum_{n=1}^{d} |u_{n}|^{4} (\partial_{\Delta\phi}\epsilon_{n})^{2}\right]} \right\}^{2}.$$
(C26)

The inequality in Eq. (C26) is saturated if and only if $\sqrt{\sum_{n=1}^{d}|u_n|^4}$ and $\sqrt{\sum_{n=1}^{d}|u_n|^4}\left[\partial_{\Delta\phi}\epsilon_n\right]^2$ are linearly dependent, which dictates $\sqrt{\sum_{n=1}^{d}|u_n|^4}\left[\partial_{\Delta\phi}\epsilon_n\right]^2=\lambda_1\sqrt{\sum_{n=1}^{d}|u_n|^4}$, with λ_1 a ϕ -independent constant. We now use the summation form of Cauchy-Schwarz inequality for two indexed sets $\{p_n\}$ and $\{q_n\}$, which states $\left(\sum_{n=1}^{d}p_nq_n\right)^2\leq\sum_{n=1}^{d}p_n^2\sum_{n=1}^{d}q_n^2$. By identifying $p_n=|u_n|^2$ and $q_n=|u_n|^2$ $\partial_{\Delta\phi}\epsilon_n$, we obtain:

$$\left[\sum_{n=1}^{d} |u_n|^4\right] \left[\sum_{n=1}^{d} |u_n|^4 \left(\partial_{\Delta\phi} \epsilon_n\right)^2\right] \ge \left[\sum_{n=1}^{d} |u_n|^4 \partial_{\Delta\phi} \epsilon_n\right]^2. \tag{C27}$$

The inequality in Eq. (C27) is saturated if and only if vectors $|u_n|^2$ and $|u_n|^2 \partial_{\Delta\phi} \epsilon_n$ are linearly dependent, dictating $|u_n|^2 \partial_{\Delta\phi} \epsilon_n = \lambda_2(\phi) |u_n|^2$ for $\forall n = 1, ..., d$, with $\lambda_2(\phi)$ only a (smooth) function of ϕ . Consequently, to saturate the inequality in Eq. (C23), we must satisfy the following two equations:

$$\sqrt{\sum_{n=1}^{d} |u_n|^4 [\partial_{\Delta\phi} \epsilon_n]^2} = \lambda_1 \sqrt{\sum_{n=1}^{d} |u_n|^4}, \quad |u_n|^2 \partial_{\Delta\phi} \epsilon_n = \lambda_2(\phi) |u_n|^2.$$
 (C28)

The solution follows as:

$$\lambda_1 = |\lambda|, \quad \lambda_2(\phi) = \lambda,$$
 (C29)

with λ a ϕ -independent constant. We next show that $\lambda \neq 0$ if $\hat{P}_j[f] \neq 0$, which ultimately contradicts the definition of $|\beta, +\rangle_f$, dictating that $\langle \beta, +|_f \hat{P}_j[f] | \beta, +\rangle_f = 0$. We first note that the trace norm of $\|\hat{P}_j[f]\|_F \equiv \sqrt{\text{Tr}\left(\hat{P}_j^{\dagger}[f]\hat{P}_j[f]\right)} > 0$ if $\hat{P}_j[f] \neq 0$. From energy conservation $\omega_1\hat{P}_1[f] + \omega_2\hat{P}_2[f] = 0$, we also know $\|\hat{P}_1[f] - \hat{P}_2[f]\|_F > 0$. From the definition of $|\beta, +\rangle_f$ [Eq. (C2)], the trace norm can be compactly written as:

$$\|\hat{P}_{1}[f] - \hat{P}_{2}[f]\|_{F}^{2} = (W_{+}[f] + W_{-}[f]) \langle \beta, +|_{f} \left(\hat{P}_{1}[f] - \hat{P}_{2}[f]\right)^{2} |\beta, +\rangle_{f}$$
(C30)

$$= \left(W_{+}[f] + W_{-}[f]\right) \left\langle \beta, +\right|_{f} \left[\sum_{n=1}^{d} \int_{BZ} d^{2}\phi \left| f\left(\phi\right) \right|^{2} \left(\partial_{\Delta\phi} \epsilon_{n}\right) \left| n\right\rangle \left\langle n\right| \right]^{2} \left| \beta, +\right\rangle_{f}$$
(C31)

$$= (W_{+}[f] + W_{-}[f]) \langle \beta, +|_{f} \left[\int_{BZ} d^{2}\phi |f(\phi)|^{2} \delta \hat{P}(\phi) \right]^{2} |\beta, +\rangle_{f}$$
 (C32)

$$= \left(W_{+}[f] + W_{-}[f]\right) \int_{BZ} d^{2}\phi_{1}d^{2}\phi_{2} \left|f\left(\phi_{1}\right)\right|^{2} \left|f\left(\phi_{2}\right)\right|^{2} \left\langle\beta, +\right|_{f} \delta \hat{P}(\phi_{1}) \delta \hat{P}(\phi_{2}) \left|\beta, +\right\rangle_{f}, \quad (C33)$$

where in the third line we have introduced $\delta \hat{P}(\phi) \equiv \hat{P}_1(\phi) - \hat{P}_2(\phi) = \sum_{n=1}^d \left[\partial_{\Delta\phi} \epsilon_n(\phi)\right] |n(\phi)\rangle \langle n(\phi)|$ [Eq. (A4)] to simplify the notation. Using the covariance form of the Cauchy-Schwarz inequality $\left|\langle \hat{X}\hat{Y}\rangle_{\beta}\right|^2 \leq \langle \hat{X}^2\rangle_{\beta} \langle \hat{Y}^2\rangle_{\beta}$, with $\langle \Box \rangle_{\beta} \equiv \langle \beta, +|_f \Box |\beta, +\rangle_f$, the expectation in Eq. (C33) satisfies the following inequality:

$$\left| \langle \delta \hat{P}(\phi_{1}) \delta \hat{P}(\phi_{2}) \rangle_{\beta} \right| \leq \sqrt{\left\langle \left[\delta \hat{P}(\phi_{1}) \right]^{2} \right\rangle_{\beta} \left\langle \left[\delta \hat{P}(\phi_{2}) \right]^{2} \right\rangle_{\beta}} \tag{C34}$$

$$= \sqrt{\left(\sum_{n=1}^{d} \left[\partial_{\Delta\phi} \epsilon_n \left(\boldsymbol{\phi_1}\right)\right]^2 \left|u_n(\boldsymbol{\phi_1})\right|^2\right) \left(\sum_{n=1}^{d} \left[\partial_{\Delta\phi} \epsilon_n \left(\boldsymbol{\phi_2}\right)\right]^2 \left|u_n(\boldsymbol{\phi_2})\right|^2\right)}.$$
 (C35)

(C36)

The trace norm is hence bounded by:

$$\|\hat{P}_{1}[f] - \hat{P}_{2}[f]\|_{F} \le \sqrt{W_{+}[f] + W_{-}[f]} \int_{BZ} d^{2}\phi |f(\phi)|^{2} \sqrt{\sum_{n=1}^{d} (\partial_{\Delta\phi}\epsilon_{n})^{2} |u_{n}|^{2}}$$
(C37)

$$= |\lambda| \sqrt{W_{+}[f] + W_{-}[f]},$$
 (C38)

where in the last line we have used Eq. (C28) and two normalization conditions: $\sum_{n=1}^{d} |u_n|^2 = 1$ and $\int_{BZ} d^2\phi |f(\phi)|^2 = 1$. It is then clear that $|\lambda| > 0$.

This, however, contradicts the requirement that $\langle \beta, +|_f \hat{P}_j[f] | \beta, + \rangle_f = 0$:

$$\sum_{n=1}^{d} \int_{BZ} d^{2}\phi |f(\phi)|^{2} |u_{n}|^{2} \partial_{\Delta\phi} \epsilon_{n} = \lambda \sum_{n=1}^{d} \int_{BZ} d^{2}\phi |f(\phi)|^{2} |u_{n}|^{2} = \lambda,$$
 (C39)

where we have used $\sum_{n=1}^{d} |u_n|^2 = 1$ and $\int_{BZ} d^2\phi |f(\phi)|^2 = 1$. We then prove that the equlity in Eq. (C23) holds only if $\hat{P}_j[f] = 0$.

Finally, note that all the above calculations are T-independent. In fact, we have taken the asymptotic limit $T \to \infty$ and dropped the $O\left(\frac{1}{T}\right)$ contributions. As a result, for non-vanishing functional power operators $\hat{P}_j[f]$, the asymptotic coefficient of the QFI $\lim_{T\to\infty}\frac{1}{T^2}F_q\left[|\mathrm{PES}\rangle_T,\hat{J}_z\right]$ takes a finite, T-independent and positive value.

We now show that the finite, T-independent, and positive asymptotic coefficient of the QFI for a 2-level ancilla can be further bounded within $\left[\frac{1}{2}P^2\left[f\right],2P^2\left[f\right]\right]$, as given in Eq. (22). Note that for a 2-level ancilla, the analysis above applies by setting d=2. Specifically, we have the following two constraints:

$$|u_1|^2 + |u_2|^2 = 1,$$
 (C40)

$$\int_{\mathrm{BZ}} d^2 \phi |f(\phi)|^2 \left[|u_1|^2 \partial_{\Delta \phi} \epsilon_1 + |u_2|^2 \partial_{\Delta \phi} \epsilon_2 \right] = 0.$$
 (C41)

The special property of a 2-level ancilla is that the expectation value of $\frac{2}{T}\langle \hat{J}_z \rangle_{\rm PES}$ asymptotically vanishes:

$$\lim_{T \to \infty} \frac{2}{T} \langle \hat{J}_z \rangle_{\text{PES}} = \frac{1}{\mathcal{N}^2} \int_{\text{PZ}} d^2 \phi \left| f(\phi) \right|^2 \left[\left| u_1 \right|^4 \partial_{\Delta \phi} \epsilon_1 + \left| u_2 \right|^4 \partial_{\Delta \phi} \epsilon_2 \right]$$
 (C42)

$$= \frac{1}{\mathcal{N}^2} \int_{BZ} d^2 \phi \left| f(\phi) \right|^2 \left[\left| u_1 \right|^4 \partial_{\Delta \phi} \epsilon_1 + \left(1 - \left| u_1 \right|^2 \right)^2 \partial_{\Delta \phi} \epsilon_2 \right]$$
 (C43)

$$= \frac{1}{\mathcal{N}^2} \int_{BZ} d^2 \phi |f(\phi)|^2 \left[|u_1|^4 \left(\partial_{\Delta \phi} \epsilon_1 + \partial_{\Delta \phi} \epsilon_2 \right) + \left(1 - 2 |u_1|^2 \right) \partial_{\Delta \phi} \epsilon_2 \right]$$
 (C44)

$$= \frac{1}{\mathcal{N}^2} \int_{BZ} d^2 \phi \left| f(\phi) \right|^2 \left[\left(1 - 2 \left| u_1 \right|^2 \right) \partial_{\Delta \phi} \epsilon_2 \right]$$
 (C45)

$$= \frac{1}{\mathcal{N}^2} \int_{\mathrm{PZ}} d^2 \phi |f(\phi)|^2 \left[\left(|u_2|^2 - |u_1|^2 \right) \partial_{\Delta \phi} \epsilon_2 \right]$$
 (C46)

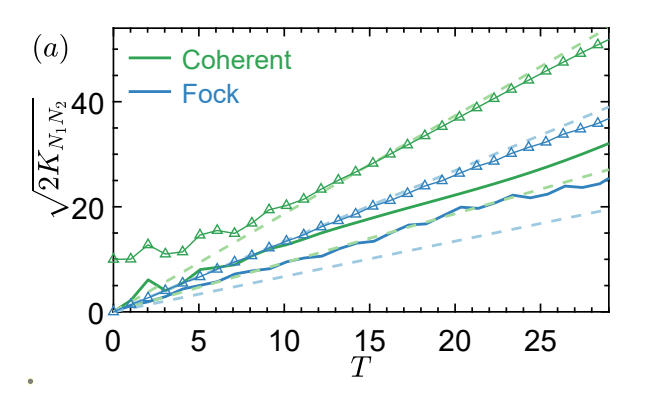
$$= \frac{1}{\mathcal{N}^2} \int_{BZ} d^2 \phi |f(\phi)|^2 \left[|u_1|^2 \partial_{\Delta \phi} \epsilon_1 + |u_2|^2 \partial_{\Delta \phi} \epsilon_2 \right] = 0, \tag{C47}$$

where from Eq. (C42) to Eq. (C43) and Eq. (C45) to Eq. (C46) we have used the property Eq. (C40); from Eq. (C44) to Eq. (C45) and Eq. (C46) to Eq. (C47) we have used the tracelessness of $\hat{P}_{1,2}$, which gives $\partial_{\Delta\phi}\epsilon_1 + \partial_{\Delta\phi}\epsilon_2 = 0$; finally, in Eq. (C47), we have used the property Eq. (C41). As a result, to find an expression for $\lim_{T\to\infty}\frac{1}{T^2}F_q\left[|\text{PES}\rangle_T,\hat{J}_z\right]$, we only need to evaluate the following term:

$$\lim_{T \to \infty} \frac{1}{T^2} F_q \left[|\text{PES}\rangle_T, \hat{J}_z \right] = \frac{1}{\mathcal{N}^2} \int_{\text{BZ}} d^2 \phi \left| f(\phi) \right|^2 \left[\left| u_1 \right|^4 \left(\partial_{\Delta \phi} \epsilon_1 \right)^2 + \left| u_2 \right|^4 \left(\partial_{\Delta \phi} \epsilon_2 \right)^2 \right]$$
 (C48)

$$= \frac{1}{\mathcal{N}^2} \int_{BZ} d^2 \phi |f(\phi)|^2 \left(|u_1|^4 + |u_2|^4 \right) \left(\partial_{\Delta \phi} \epsilon_1 \right)^2, \tag{C49}$$

$$\mathcal{N}^{2} = \int_{BZ} d^{2}\phi |f(\phi)|^{2} (|u_{1}|^{4} + |u_{2}|^{4}), \qquad (C50)$$



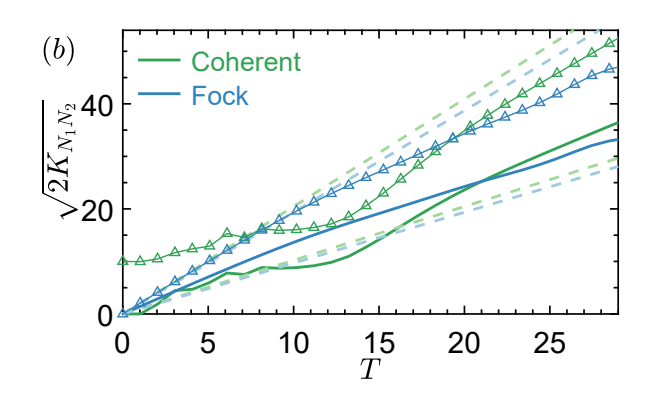


FIG. 7. Time evolution of the covariance $K_{N_1N_2} \equiv -2 \left[\langle \hat{a}_1^{\dagger} \hat{a}_1 \hat{a}_2^{\dagger} \hat{a}_2 \rangle_{\mathrm{PES}} - \langle \hat{a}_1^{\dagger} \hat{a}_1 \rangle_{\mathrm{PES}} \langle \hat{a}_2^{\dagger} \hat{a}_2 \rangle_{\mathrm{PES}} \right]$ for different models and inputs. Specifically, we select two models discussed in the main text: (a) qubit under circularly-polarized drives with same chiralities [Eq. (24)] and (b) qubit under circularly-polarized drives with opposite chiralities [Eq. (27)]. Green and blue curves represent coherent-state and Fock-state inputs initially. Bounds in Eq. (D11) are represented as colored dashed lines for both inputs. For comparison, we add the quantum Fisher information $\sqrt{F_Q}$ for both inputs ($-\Delta$ - curves). We start with an average of 50 bosons in each drive. For coherent-state inputs, we introduce an initial phase difference $\phi_{20} - \phi_{10} = 0.6\pi$ between two drives. Other parameters in different models are given as: (a) $\omega = \frac{\omega_0}{4}$, $\mathcal{A} = \frac{\omega_0}{8}$; and (b) $\omega = \omega_0$, $\mathcal{A} = \frac{\omega_0}{2}$.

where from Eq. (C48) to Eq. (C49) we have used the tracelessness of the power operators that gives $\partial_{\Delta\phi}\epsilon_1 + \partial_{\Delta\phi}\epsilon_2 = 0$. Noting that $|u_1|^4 + |u_2|^4$ is bounded between $\left[\frac{1}{2}, 1\right]$ under the constraint $|u_1|^2 + |u_2|^2 = 1$, we find the following bounds for the numerator and denominator of Eq. (C49):

$$\frac{1}{2}P^{2}[f] \leq \int_{BZ} d^{2}\phi |f(\phi)|^{2} (|u_{1}|^{4} + |u_{2}|^{4}) (\partial_{\Delta\phi}\epsilon_{1})^{2} \leq P^{2}[f],$$
 (C51)

$$\frac{1}{2} \le \mathcal{N}^2 \le 1,\tag{C52}$$

with $P^{2}\left[f\right] \equiv \frac{1}{2} \int_{\mathrm{BZ}} d^{2}\phi \left|f^{2}\left(\phi\right)\right| \left[\left(\partial_{\Delta\phi}\epsilon_{1}\right)^{2}+\left(\partial_{\Delta\phi}\epsilon_{2}\right)^{2}\right]$. The asymptotic coefficient of the QFI is hence bounded by:

$$\frac{1}{2}P^{2}\left[f\right] \leq \lim_{T \to \infty} \frac{1}{T^{2}} F_{q} \left[\left|\text{PES}\right\rangle_{T}, \hat{J}_{z}\right] \leq 2P^{2}\left[f\right]. \tag{C53}$$

Appendix D: Path entanglement

We now show that $|\text{PES}\rangle_T$ with QFI approaching the Heisenberg limit, given by Eq. (C53), exhibits path entanglement for large conversion time T. Specifically, such entanglement is quantified by a similar bound Q[f] in the long-time limit. For clarity, we explain the terminology 'path entanglement' (Sec. IVB). It is borrowed from optical interferometry [69], where two spatially distinguishable modes of photons enter different interferometric arms or paths. Path entanglement simply refers to the mode entanglement between arms or paths. In order to show that the state $|\text{PES}\rangle_T$ [Eq. (C3)] is path-entangled, we need to show the following inequality holds [101]:

$$\operatorname{Var}\left(\hat{J}_{z}\right) > \operatorname{Var}\left(\frac{1}{2}\hat{a}_{1}^{\dagger}\hat{a}_{1}\right) + \operatorname{Var}\left(\frac{1}{2}\hat{a}_{2}^{\dagger}\hat{a}_{2}\right),\tag{D1}$$

with $Var(\square)$ the variance of \square with respect to $|PES\rangle_T$. We can equivalently show:

$$\langle \hat{a}_{1}^{\dagger} \hat{a}_{1} \hat{a}_{2}^{\dagger} \hat{a}_{2} \rangle_{\text{PES}} \langle \langle \hat{a}_{1}^{\dagger} \hat{a}_{1} \rangle_{\text{PES}} \langle \hat{a}_{2}^{\dagger} \hat{a}_{2} \rangle_{\text{PES}}. \tag{D2}$$

We stick to an ancilla qubit (d=2) and calculate the left-hand side of Eq. (D2) in the large T limit. Using the phase representation of the number operator $\hat{a}_{j}^{\dagger}\hat{a}_{j}=-i\partial_{\phi_{j}}$, we have

$$\langle \hat{a}_{1}^{\dagger} \hat{a}_{1} \hat{a}_{2}^{\dagger} \hat{a}_{2} \rangle_{\text{PES}} = -\frac{1}{\mathcal{N}_{T}^{2}} \sum_{m,n=1,2} \int_{\text{BZ}} d^{2} \bar{\phi} d^{2} \phi f^{*} \left(\bar{\phi} \right) f \left(\phi \right) \left| u_{m}^{*} u_{n} \right|^{2} e^{-i(\epsilon_{n} - \epsilon_{m})T} \left\langle \bar{\phi} \left| \partial_{\phi_{1}} \partial_{\phi_{2}} \right| \phi \right\rangle$$
(D3)

$$=T^{2} \frac{1}{N^{2}} \sum_{n=1,2} \int_{BZ} d^{2} \phi |f(\phi)|^{2} |u_{n}|^{4} (\partial_{\phi_{1}} \epsilon_{n}) (\partial_{\phi_{2}} \epsilon_{n}) + O(T^{3/2}), \tag{D4}$$

where we use the stationary phase approximation [see discussion around Eq. (C6)] to replace the double summation to a single one. From the energy conservation: $(\omega_1 \partial_{\phi_1} + \omega_2 \partial_{\phi_2}) \epsilon_n = 0$, we know $(\partial_{\phi_1} \epsilon_n)(\partial_{\phi_2} \epsilon_n) \leq 0$. Specifically, for a dispersive band structure, we have $(\partial_{\phi_1} \epsilon_n)(\partial_{\phi_2} \epsilon_n) < 0$ and hence

$$\langle \hat{a}_1^{\dagger} \hat{a}_1 \hat{a}_2^{\dagger} \hat{a}_2 \rangle_{\text{PES}} = -\mathcal{B}T^2 + O(T^{3/2}),\tag{D5}$$

with $\mathcal{B} \equiv \frac{1}{\mathcal{N}^2} \sum_{n=1,2} \int_{\mathrm{BZ}} d^2 \phi |f(\phi)|^2 |u_n|^4 |(\partial_{\phi_1} \epsilon_n)(\partial_{\phi_2} \epsilon_n)|.$

We next evaluate the right-hand side of Eq. (D2):

$$\langle \hat{a}_{j}^{\dagger} \hat{a}_{j} \rangle_{\text{PES}} = -\frac{i}{\mathcal{N}_{T}^{2}} \sum_{m,n=1,2} \int_{\mathbf{D}Z} d^{2} \bar{\phi} d^{2} \phi f^{*} \left(\bar{\phi} \right) f \left(\phi \right) \left| u_{m}^{*} u_{n} \right|^{2} e^{-i(\epsilon_{n} - \epsilon_{m})T} \left\langle \bar{\phi} \right| \partial_{\phi_{j}} \left| \phi \right\rangle \tag{D6}$$

$$= T \frac{1}{N^2} \sum_{n=1,2} \int_{\mathbb{R}^2} d^2 \phi |f(\phi)|^2 |u_n|^4 \partial_{\phi_j} \epsilon_n + O(T^{1/2})$$
 (D7)

$$=O(T^{1/2}). (D8)$$

From the 1-st line to the 2-nd line, we drop the fast oscillating terms using the stationary phase approximation. From the 2-nd to the last line, we use the fact that

$$\sum_{n=1,2} \int_{BZ} d^{2} \phi |f(\phi)|^{2} |u_{n}|^{4} \partial_{\phi_{j}} \epsilon_{n} = 0,$$
 (D9)

following the same argument as in Eq. (C42)-(C47). It follows that

$$\langle \hat{a}_1^{\dagger} \hat{a}_1 \hat{a}_2^{\dagger} \hat{a}_2 \rangle_{\text{PES}} - \langle \hat{a}_1^{\dagger} \hat{a}_1 \rangle_{\text{PES}} \langle \hat{a}_2^{\dagger} \hat{a}_2 \rangle_{\text{PES}} = -\mathcal{B}T^2 + O(T^{3/2}). \tag{D10}$$

This shows that at sufficiently late times T, Eq. (D2) is fulfilled and $|PES\rangle_T$ is path-entangled.

We now comment on the relation of the Heisenberg-limit scaling of the QFI, derived in the previous appendix, and the path entanglement shown here. We first bound \mathcal{B} . Using $|u_1|^4 + |u_2|^4 \in \left[\frac{1}{2}, 1\right]$, we have

$$\frac{1}{2}Q[f] \le \mathcal{B} \le 2Q[f],\tag{D11}$$

with $Q[f] \equiv \int_{\mathrm{BZ}} d^2\phi \left| f^2(\phi) \right| \left| (\partial_{\phi_1} \epsilon_1) \left(\partial_{\phi_2} \epsilon_2 \right) \right|$. Note that we can express $P^2[f]$, defined in Eq. (C53), as

$$P^{2}[f] = \int_{BZ} d^{2}\phi \left| f^{2}(\phi) \right| \left[(\partial_{\phi_{1}}\epsilon_{1})^{2} + (\partial_{\phi_{2}}\epsilon_{2})^{2} + 2(\partial_{\phi_{1}}\epsilon_{1})(\partial_{\phi_{2}}\epsilon_{2}) \right]$$
(D12)

$$= \int_{\mathbb{R}^{7}} d^{2}\phi \left| f^{2}(\phi) \right| \left[(\partial_{\phi_{1}}\epsilon_{1})^{2} + (\partial_{\phi_{2}}\epsilon_{2})^{2} \right] + 2Q[f], \tag{D13}$$

using $\partial_{\phi_j} \epsilon_1 + \partial_{\phi_j} \epsilon_2 = 0$ from the tracelessness of $\hat{P}_j[f]$. It is then clear that a non-zero $\mathcal{Q}[f]$ from path entanglement can enhance the QFI bounded by $P^2[f]$. Thus, the HL sensitivity is not an exclusive property for path (mode) entanglement, such entanglement enters as an enhancement in F_q . This phenomenon is also present for the N00N state: the sum of QFI $F_q\left[\text{N00N}, \frac{1}{2}\hat{a}_1^{\dagger}\hat{a}_1\right] + F_q\left[\text{N00N}, \frac{1}{2}\hat{a}_2^{\dagger}\hat{a}_2\right] = \frac{N^2}{2}$ for two number operators (divided by $\frac{1}{2}$) equals half of the QFI $F_q\left[\text{N00N}, \hat{J}_z\right]$ for $\hat{J}_z = \frac{1}{2}\hat{a}_1^{\dagger}\hat{a}_1 - \frac{1}{2}\hat{a}_2^{\dagger}\hat{a}_2$. The missing half comes exactly from the mode entanglement. Here, we see a more general version of this. Labeling $K_{N_1N_2} \equiv -2\left[\langle \hat{a}_1^{\dagger}\hat{a}_1\hat{a}_2^{\dagger}\hat{a}_2\rangle_{\text{PES}} - \langle \hat{a}_1^{\dagger}\hat{a}_1\rangle_{\text{PES}}\langle \hat{a}_2^{\dagger}\hat{a}_2\rangle_{\text{PES}}\right]$, we note that the contribution in the QFI from mode entanglement is given by $2K_{N_1N_2}$. In Fig. 7, we plot $\sqrt{2K_{N_1N_2}}$ as functions of T for models given in Eq. (24) and Eq. (27).

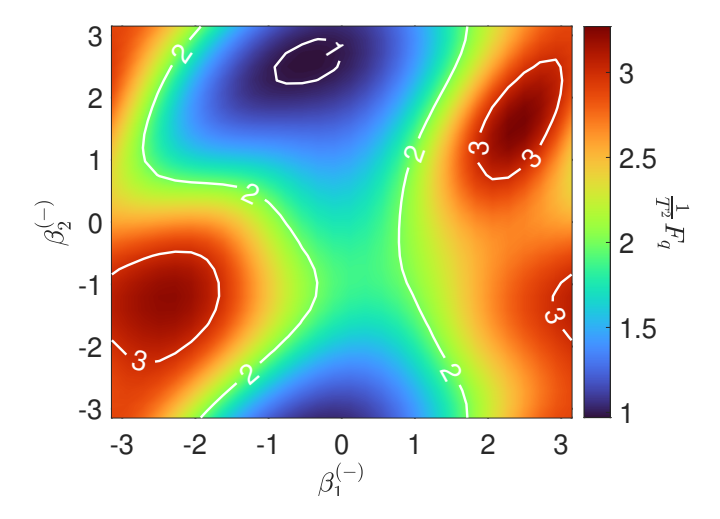


FIG. 8. Optimization of the quantum Fisher information for the qutrit model. For the qutrit model given in Eq. (E1), there are 2 degrees of freedom $\beta_1^{(-)}, \beta_2^{(-)}$ in defining the initial qutrit state $|\beta, +\rangle_f$. The landscape of the quantum Fisher information $\frac{1}{T^2}F_q\left[|\text{PES}\rangle_T, \hat{J}_z\right](\beta_1^{(-)}, \beta_2^{(-)})$ shows strong dependence on these parameters. We initialize the drives in the Fock state with 30 bosons in each mode choose the following parameters: $\omega_{12} = \omega$, $\omega_{23} = \frac{1}{2}\omega$, $\mathcal{A} = \frac{\omega}{2}$ and $T = 10T_{\text{com}}$.

Appendix E: Maximizing the quantum Fisher information in qudit systems

In this appendix, we generalize the above analysis to higher dimensional systems (qudits). Naturally, introducing a larger Hilbert space endows us with extra degrees of freedom in defining the initial state that optimizes the QFI.

We start with optimizaing the QFI for a qubit. According to our procedure of generating PES's, there is a phase degree of freedom β in defining $|\beta,+\rangle_f$. While this initial phase does not affect the energy transfer since $\langle \beta,+|_f \hat{P}_j [f] | \beta,+\rangle_f = 0$ holds for $\forall \beta \in [0,2\pi)$, the scaling of QFI, $\lim_{T\to\infty} \frac{1}{T^2} F_q \left[|\text{PES}\rangle_T, \hat{J}_z \right]$, varies with β in general. Hence, by optimizing the initial phase β , one maximizes the QFI of PES's. This, however, is only an improvement by a constant factor, compared with the improvement by a scaling factor $\frac{1}{\sqrt{T}}$ when moving from the SQL to the HL. Furthermore, the bound $P^2[f]$ on the QFI is independent of β , which means we can only maximize $\lim_{T\to\infty} \frac{1}{T^2} F_q \left[|\text{PES}\rangle_T, \hat{J}_z \right]$ within the interval $\left[\frac{1}{2} P^2 [f], 2P^2 [f] \right]$. Following this procedure, we get $\sim 10\%$ improvement of QFI for the polarization conversion model [Eq. (27)].

When promoting the qubit to a d-dimensional ancilla (qudit, d>2), such optimization becomes more significant. From the definition of $|\beta,+\rangle_f$ [Eq. (C2)], we have $D=W_+[f]+W_-[f]-1$ independent phases $\left\{\beta_1^{(+)},...,\beta_{W_+[f]-1}^{(+)},\beta_1^{(-)},...,\beta_{W_-[f]}^{(-)}\right\}$. Importantly, while the PES's in Eq. (C3) still exhibit the HL (App. C), they now generally have a non-vanishing expectation of \hat{J}_z (where in the qubit case $\langle \hat{J}_z \rangle = 0$ for all β). Therefore, it is necessary to tune the D phases such that the QFI is maximized.

As an example, we study the optimization of the QFI for the following driven-qutrit model:

$$\hat{H}_{\phi}(t) = \omega_{12} |e1\rangle \langle e1| + (\omega_{12} + \omega_{23}) |e2\rangle \langle e2|$$

$$+ \frac{1}{2} \mathcal{A} \cos(\omega t + \phi_1) (|e1\rangle \langle g| + |g\rangle \langle e1|)$$

$$+ \frac{1}{2} \mathcal{A} \cos(\omega t + \phi_2) (|e2\rangle \langle e1| + |e1\rangle \langle e2|)$$

$$+ 2\mathcal{A} \sin(\omega t + \phi_1) (|e2\rangle \langle g| + |g\rangle \langle e2|)$$

$$- 2\mathcal{A} \sin(\omega t + \phi_2) (|e2\rangle \langle g| + |g\rangle \langle e2|),$$
(E1)

where $|g\rangle$, $|e1\rangle$, $|e2\rangle$ are the ground state, 1-st excited state and 2-nd excited state for the qutrit. For a symmetric Fock-state input $|f(\phi)|^2 = \frac{1}{4\pi^2}$, the functional power operator $P_2[f]$ with respect to the second drive has one positive

eigenvalue P_{+} and two negative eigenvalues $P_{-,1}, P_{-,2}$ satisfying $P_{+} + P_{-,1} + P_{-,2} = 0$. Denoting the corresponding eigenvectors as $|+\rangle$, $|-,1\rangle$, and $|-,2\rangle$, the initial qudit state $|\beta,+\rangle$ is hence defined as [Eq. (C2)]:

$$|\beta, +\rangle = \frac{1}{\sqrt{3}} \left(|+\rangle + e^{i\beta_1^{(-)}} |-, 1\rangle + e^{i\beta_2^{(-)}} |-, 2\rangle \right).$$
 (E2)

The optimization of the QFI goes over $\beta_1^{(-)}, \beta_2^{(-)} \in [0, 2\pi)$. In Fig. 8, this optimization results in a significant increase in the QFI from $\frac{1}{T^2}F_q\left[\left|\mathrm{PES}\right\rangle_T,\hat{J}_z\right]<1$ to $\frac{1}{T^2}F_q\left[\left|\mathrm{PES}\right\rangle_T,\hat{J}_z\right]>3.$

Appendix F: Derivation of the parity operator

In this appendix, we derive the form of the parity operator following a Mach-Zehnder interferometer. We first recall how a 50-50 beam splitter, represented as $\hat{\mathcal{U}}_{\text{de}}^{\text{MZI}} = e^{-i\hat{J}_x\frac{\pi}{2}}$, acts on the annihilation operators:

$$\hat{\mathcal{U}}_{\text{de}}^{\text{MZI},\dagger} \hat{a}_{1} \hat{\mathcal{U}}_{\text{de}}^{\text{MZI}} = e^{i\frac{\pi}{4} \left(\hat{a}_{1}^{\dagger} \hat{a}_{2} + \hat{a}_{2}^{\dagger} \hat{a}_{1} \right)} \hat{a}_{1} e^{-i\frac{\pi}{4} \left(\hat{a}_{1}^{\dagger} \hat{a}_{2} + \hat{a}_{2}^{\dagger} \hat{a}_{1} \right)}$$
(F1)

$$= \frac{1}{\sqrt{2}} (\hat{a}_1 - i\hat{a}_2), \tag{F2}$$

$$= \frac{1}{\sqrt{2}} (\hat{a}_1 - i\hat{a}_2), \tag{F2}$$

$$\hat{\mathcal{U}}_{de}^{\text{MZI},\dagger} \hat{a}_2 \hat{\mathcal{U}}_{de}^{\text{MZI}} = e^{i\frac{\pi}{4} (\hat{a}_1^{\dagger} \hat{a}_2 + \hat{a}_2^{\dagger} \hat{a}_1)} \hat{a}_2 e^{-i\frac{\pi}{4} (\hat{a}_1^{\dagger} \hat{a}_2 + \hat{a}_2^{\dagger} \hat{a}_1)}$$

$$= \frac{1}{2} (\hat{a}_2 - i\hat{a}_1). \tag{F4}$$

$$=\frac{1}{\sqrt{2}}\left(\hat{a}_2 - i\hat{a}_1\right),\tag{F4}$$

where we have used the Baker-Campbell-Hausdorff (BCH) formula. Plugging these transformations into the parity operator, we obtain:

$$\hat{\mathcal{U}}_{\mathrm{de}}^{\mathrm{MZI},\dagger} \hat{\Pi} \hat{\mathcal{U}}_{\mathrm{de}}^{\mathrm{MZI}} = \hat{\mathcal{U}}_{\mathrm{de}}^{\mathrm{MZI},\dagger} (-1)^{\hat{a}_2 \hat{a}_2} \hat{\mathcal{U}}_{\mathrm{de}}^{\mathrm{MZI}}$$
 (F5)

$$=e^{i\frac{\pi}{4}(\hat{a}_{1}^{\dagger}\hat{a}_{2}+\hat{a}_{2}^{\dagger}\hat{a}_{1})}e^{i\pi\hat{a}_{2}\hat{a}_{2}}e^{-i\frac{\pi}{4}(\hat{a}_{1}^{\dagger}\hat{a}_{2}+\hat{a}_{2}^{\dagger}\hat{a}_{1})}$$
(F6)

$$=e^{i\frac{\pi}{2}(\hat{a}_{1}^{\dagger}\hat{a}_{1}+\hat{a}_{2}^{\dagger}\hat{a}_{2})}e^{\frac{\pi}{2}(\hat{a}_{2}^{\dagger}\hat{a}_{1}-\hat{a}_{1}^{\dagger}\hat{a}_{2})},\tag{F7}$$

where the first exponential in Eq. (F7) is a global phase factor in the SU(2) interferometer given by the total boson number $\hat{N} = \hat{a}_1^{\dagger} \hat{a}_1 + \hat{a}_2^{\dagger} \hat{a}_2$. The second term, which can be written as $e^{i\hat{J}_y\pi}$, has nontrivial action on the annihilation

$$e^{\frac{\pi}{2}(\hat{a}_{2}^{\dagger}\hat{a}_{1} - \hat{a}_{1}^{\dagger}\hat{a}_{2})}\hat{a}_{1}e^{-\frac{\pi}{2}(\hat{a}_{2}^{\dagger}\hat{a}_{1} - \hat{a}_{1}^{\dagger}\hat{a}_{2})} = \hat{a}_{2},\tag{F8}$$

$$e^{\frac{\pi}{2}(\hat{a}_{2}^{\dagger}\hat{a}_{1} - \hat{a}_{1}^{\dagger}\hat{a}_{2})}\hat{a}_{2}e^{-\frac{\pi}{2}(\hat{a}_{2}^{\dagger}\hat{a}_{1} - \hat{a}_{2}^{\dagger}\hat{a}_{2})} = -\hat{a}_{1},\tag{F9}$$

which hence behaves as a SWAP operator with an extra sign determined by the parity of bosons in the 2nd mode:

$$e^{\frac{\pi}{2}(\hat{a}_2^{\dagger}\hat{a}_1 - \hat{a}_1^{\dagger}\hat{a}_2)} = \hat{S}\hat{\Pi},$$
 (F10)

with $\hat{S} = \sum_{n,m=1}^{\infty} |n\rangle \langle m| \otimes |m\rangle \langle n|$ the SWAP operator over two bosonic modes. Finally we apply $\hat{\mathcal{U}}_{\theta}^{\text{MZI}}$ on the transformed parity operator and obtain:

$$\hat{\mathcal{U}}_{\theta}^{\mathrm{MZI},\dagger} \, \hat{\mathcal{U}}_{\mathrm{de}}^{\mathrm{MZI},\dagger} \, \hat{\Pi} \, \hat{\mathcal{U}}_{\mathrm{de}}^{\mathrm{MZI}} \, \hat{\mathcal{U}}_{\theta}^{\mathrm{MZI}}$$
 (F11)

$$= \hat{\mathcal{U}}_{\theta}^{\text{MZI},\dagger} e^{i\frac{\pi}{2} \left(\hat{a}_{1}^{\dagger} \hat{a}_{1} + \hat{a}_{2}^{\dagger} \hat{a}_{2}\right)} \hat{S} \hat{\Pi} \hat{\mathcal{U}}_{\theta}^{\text{MZI}}$$
(F12)

$$=e^{i\frac{1}{2}(\hat{a}_{1}^{\dagger}\hat{a}_{1}-\hat{a}_{2}^{\dagger}\hat{a}_{2})\theta}e^{i\frac{\pi}{2}(\hat{a}_{1}^{\dagger}\hat{a}_{1}+\hat{a}_{2}^{\dagger}\hat{a}_{2})}\hat{S}\hat{\Pi}e^{-i\frac{1}{2}(\hat{a}_{1}^{\dagger}\hat{a}_{1}-\hat{a}_{2}^{\dagger}\hat{a}_{2})\theta}$$
(F13)

$$=e^{i\frac{1}{2}(\hat{a}_{1}^{\dagger}\hat{a}_{1}-\hat{a}_{2}^{\dagger}\hat{a}_{2})\theta}e^{i\frac{\pi}{2}(\hat{a}_{1}^{\dagger}\hat{a}_{1}+\hat{a}_{2}^{\dagger}\hat{a}_{2})}\hat{S}e^{i\pi\hat{a}_{2}^{\dagger}\hat{a}_{2}}e^{-i\frac{1}{2}(\hat{a}_{1}^{\dagger}\hat{a}_{1}-\hat{a}_{2}^{\dagger}\hat{a}_{2})\theta}$$
(F14)

$$=e^{i(\theta-\frac{\pi}{2})\hat{a}_{1}^{\dagger}\hat{a}_{1}}\hat{S}e^{-i(\theta-\frac{\pi}{2})\hat{a}_{1}^{\dagger}\hat{a}_{1}}$$
(F15)

$$=e^{i\left(\theta-\frac{\pi}{2}\right)\left(\hat{a}_{1}^{\dagger}\hat{a}_{1}-\hat{a}_{2}^{\dagger}\hat{a}_{2}\right)}\hat{S}\tag{F16}$$

$$=e^{2i\hat{J}_z\left(\theta-\frac{\pi}{2}\right)}\hat{S},\tag{F17}$$

where we have used \hat{S} $\hat{a}_1^{\dagger}\hat{a}_1$ $\hat{S} = \hat{a}_2^{\dagger}\hat{a}_2$ and \hat{S} $\hat{a}_2^{\dagger}\hat{a}_2$ $\hat{S} = \hat{a}_1^{\dagger}\hat{a}_1$.

Appendix G: Sensitivity of parity measurement

In this appendix, we prove two necessary conditions on driving frequencies and bandstructure for sub-SQL sensitivity from parity measurement on the path-entangled states $|\text{PES}\rangle_T$ defined in Eq. (C3). We start with evaluating the expectation value of the parity operator $\hat{\Pi}_{\tilde{\theta}} = e^{2i\hat{J}_z\tilde{\theta}}\hat{S}$ [Eq. (F17)] for $|\text{PES}\rangle_T$. The action of $e^{2i\hat{J}_z\tilde{\theta}}$ and \hat{S} on a phase eigenstate $|\phi\rangle = |\phi_1\rangle \otimes |\phi_2\rangle$ is given as:

$$e^{2i\hat{J}_z\tilde{\theta}} |\phi\rangle = |\phi_1 + \tilde{\theta}\rangle \otimes |\phi_2 - \tilde{\theta}\rangle, \tag{G1}$$

$$\hat{S} | \boldsymbol{\phi} \rangle = | \phi_2 \rangle \otimes | \phi_1 \rangle \,. \tag{G2}$$

Here, $e^{2i\hat{J}_z\tilde{\theta}}$ acts as a translation in phase space, while \hat{S} swaps two phases. We next evaluate the expectation explicitly:

$$\langle \hat{\Pi}_{\tilde{\theta}} \rangle_{\text{PES}} = \langle \text{PES}|_T \, \hat{\Pi}_{\tilde{\theta}} \, | \text{PES} \rangle_T$$
 (G3)

$$= \frac{1}{\mathcal{N}_T^2} \sum_{m,n=1}^{a} \int_{BZ} d^2 \bar{\phi} d^2 \phi f^* \left(\bar{\phi}\right) f \left(\phi\right) u_m^* u_n e^{-i(\epsilon_n - \epsilon_m)T} \left\langle m | \hat{\Pi}_\beta | n \right\rangle \left\langle \bar{\phi} | \hat{\Pi}_{\tilde{\theta}} | \phi \right\rangle \tag{G4}$$

$$= \frac{1}{\mathcal{N}_T^2} \sum_{m,n=1}^d \int_{\mathrm{BZ}} d^2 \bar{\phi} d^2 \phi f^* \left(\bar{\phi}\right) f\left(\phi\right) \left|u_m^* u_n\right|^2 e^{-i(\epsilon_n - \epsilon_m)T} \left\langle\bar{\phi}\right| e^{2i\hat{J}_z \tilde{\theta}} \hat{S} \left|\phi\right\rangle \tag{G5}$$

$$= \frac{1}{\mathcal{N}_{T}^{2}} \sum_{m,n=1}^{d} \int_{\mathrm{BZ}} d^{2} \bar{\phi} d^{2} \phi f^{*} \left(\bar{\phi}\right) f\left(\phi\right) \left|u_{m}^{*} u_{n}\right|^{2} e^{-i(\epsilon_{n} - \epsilon_{m})T} \left\langle\bar{\phi}_{1} | \phi_{2} + \tilde{\theta}\right\rangle \left\langle\bar{\phi}_{2} | \phi_{1} - \tilde{\theta}\right\rangle$$
(G6)

$$= \frac{1}{\mathcal{N}_T^2} \sum_{m,n=1}^d \int_{\mathrm{BZ}} d^2 \bar{\phi} d^2 \phi f^* \left(\bar{\phi}\right) f\left(\phi\right) \left|u_m^* u_n\right|^2 e^{-i(\epsilon_n - \epsilon_m)T} \delta(\bar{\phi}_1 - \phi_2 - \tilde{\theta}) \ \delta(\bar{\phi}_2 - \phi_1 + \tilde{\theta})$$
 (G7)

$$= \frac{1}{\mathcal{N}_T^2} \sum_{m,n=1}^d \int_{BZ} d^2 \phi f^*(\phi_2 + \tilde{\theta}, \phi_1 - \tilde{\theta}) f(\phi_1, \phi_2) \left| u_m^*(\phi_2 + \tilde{\theta}, \phi_1 - \tilde{\theta}) u_n(\phi_1, \phi_2) \right|^2 e^{-i\left[\epsilon_n(\phi_1, \phi_2) - \epsilon_m(\phi_2 + \tilde{\theta}, \phi_1 - \tilde{\theta})\right]T}, \tag{G8}$$

where in the last line we write the ϕ -dependence explicitly. To simplify the expression, we use the energy conservation $\epsilon_1 \hat{P}_1 + \epsilon_2 \hat{P}_2 = 0$, which enables our treating of $\epsilon_n(\tilde{x}) = \epsilon_n(\phi_1, \phi_2)$ as a single-parameter function of $\tilde{x} = \frac{1}{\sqrt{2}} \left(\frac{\phi_1}{\omega_1} - \frac{\phi_2}{\omega_2} \right)$ that does not depend on $\tilde{y} = \frac{1}{\sqrt{2}} \left(\omega_2 \phi_1 + \omega_1 \phi_2 \right)$ completely. In terms of \tilde{x}, \tilde{y} , Eq. (G8) can be written as:

$$\langle \hat{\Pi}_{\tilde{\theta}} \rangle_{\text{PES}} = \frac{1}{\mathcal{N}_T^2} \sum_{m,n=1}^d \int d\tilde{x} d\tilde{y} \mathcal{M}_{nm}(\tilde{x}, \tilde{y}, \tilde{\theta}) e^{-i\chi_{nm}(\tilde{x}, \tilde{y}, \tilde{\theta})T}, \tag{G9}$$

$$\mathcal{M}_{nm}(\tilde{x}, \tilde{y}, \tilde{\theta}) = f^*(\phi_2 + \tilde{\theta}, \phi_1 - \tilde{\theta}) f(\phi_1, \phi_2) \left| u_m^*(\phi_2 + \tilde{\theta}, \phi_1 - \tilde{\theta}) u_n(\phi_1, \phi_2) \right|^2, \tag{G10}$$

$$\chi_{nm}(\tilde{x}, \tilde{y}, \tilde{\theta}) = \epsilon_n(\tilde{x}) - \epsilon_m \left[-\frac{1}{2} \left(\frac{\omega_1}{\omega_2} + \frac{\omega_2}{\omega_1} \right) \tilde{x} + \frac{1}{2} \left(\frac{1}{\omega_1^2} - \frac{1}{\omega_2^2} \right) \tilde{y} + \frac{1}{\sqrt{2}} \left(\frac{1}{\omega_1} + \frac{1}{\omega_2} \right) \tilde{\theta} \right], \tag{G11}$$

where we have defined the characteristic function χ_{nm} as the difference between quasienergies from the *n*-th band at (ϕ_1, ϕ_2) and the *m*-th band at $(\phi_2 + \tilde{\theta}, \phi_1 - \tilde{\theta})$. A similar expression can be obtained for $\partial_{\tilde{\theta}} \langle \hat{\Pi}_{\tilde{\theta}} \rangle_{\text{PES}}$ by direct differentiation

$$\partial_{\tilde{\theta}} \langle \hat{\Pi}_{\tilde{\theta}} \rangle_{\text{PES}} = \frac{1}{\mathcal{N}_T^2} \sum_{m,n=1}^d \int d\tilde{x} d\tilde{y} \left[\partial_{\tilde{\theta}} \mathcal{M}_{nm}(\tilde{x}, \tilde{y}, \tilde{\theta}) \right] e^{-i\chi_{nm}(\tilde{x}, \tilde{y}, \tilde{\theta})T}$$
(G12)

$$-\frac{iT}{\mathcal{N}_T^2} \sum_{m,n=1}^d \int d\tilde{x} d\tilde{y} \mathcal{M}_{nm}(\tilde{x}, \tilde{y}, \tilde{\theta}) \left[\partial_{\tilde{\theta}} \chi_{nm}(\tilde{x}, \tilde{y}, \tilde{\theta}) \right] e^{-i\chi_{nm}(\tilde{x}, \tilde{y}, \tilde{\theta})T}. \tag{G13}$$

Noting that at asymptotic time $T \to \infty$, the integrands in Eq. (G9), (G12), (G13) are fast oscillating and sharing same exponentials $e^{-i\chi_{nm}(\tilde{x},\tilde{y},\tilde{\theta})T}$, these integrals are hence fully determined by their behaviors at critical points of the characteristic function $\chi_{nm}(\tilde{x},\tilde{y},\tilde{\theta})$, known as the stationary phase approximation. To find all such critical points, we need to solve the following equation:

$$\nabla \chi_{nm}(\tilde{x}, \tilde{y}, \tilde{\theta}) = 0, \tag{G14}$$

where $\nabla = (\partial_{\tilde{x}}, \partial_{\tilde{y}})$ is the gradient operator in the \tilde{x}, \tilde{y} basis. This gives:

$$\partial_{\tilde{x}}\chi_{nm} = 0 \quad \rightarrow \quad \epsilon'_{n}(\tilde{x}) + \frac{1}{2} \left(\frac{\omega_{1}}{\omega_{2}} + \frac{\omega_{2}}{\omega_{1}} \right) \epsilon'_{m} \left[-\frac{1}{2} \left(\frac{\omega_{1}}{\omega_{2}} + \frac{\omega_{2}}{\omega_{1}} \right) \tilde{x} + \frac{1}{2} \left(\frac{1}{\omega_{1}^{2}} - \frac{1}{\omega_{2}^{2}} \right) \tilde{y} + \frac{1}{\sqrt{2}} \left(\frac{1}{\omega_{1}} + \frac{1}{\omega_{2}} \right) \tilde{\theta} \right] = 0, \tag{G15}$$

$$\partial_{\tilde{y}}\chi_{nm} = 0 \quad \rightarrow \quad \frac{1}{2} \left(\frac{1}{\omega_1^2} - \frac{1}{\omega_2^2} \right) \epsilon_m' \left[-\frac{1}{2} \left(\frac{\omega_1}{\omega_2} + \frac{\omega_2}{\omega_1} \right) \tilde{x} + \frac{1}{2} \left(\frac{1}{\omega_1^2} - \frac{1}{\omega_2^2} \right) \tilde{y} + \frac{1}{\sqrt{2}} \left(\frac{1}{\omega_1} + \frac{1}{\omega_2} \right) \tilde{\theta} \right] = 0, \quad (G16)$$

where $\epsilon_{n,m}^{'}(t) \equiv \frac{d}{dt} \epsilon_{n,m}(t)$ is the differential notation. Case $\omega_1 \neq \omega_2$: For $\omega_1 \neq \omega_2$, the above equations give:

$$\epsilon_{n}^{'}(\tilde{x}) = \epsilon_{m}^{'} \left[-\frac{1}{2} \left(\frac{\omega_{1}}{\omega_{2}} + \frac{\omega_{2}}{\omega_{1}} \right) \tilde{x} + \frac{1}{2} \left(\frac{1}{\omega_{1}^{2}} - \frac{1}{\omega_{2}^{2}} \right) \tilde{y} + \frac{1}{\sqrt{2}} \left(\frac{1}{\omega_{1}} + \frac{1}{\omega_{2}} \right) \tilde{\theta} \right] = 0, \tag{G17}$$

which gives rise to the following two cases: 1. no solution: there is no stationary phase and hence the expectation value of the parity operator $\langle \hat{\Pi}_{\tilde{\theta}} \rangle_{\text{PES}} = o\left(\frac{1}{T}\right)$ decays faster than T^{-1} as $T \to \infty$, which does not contain any information about the phase $\tilde{\theta}$. A similar argument can be directly applied to $\partial_{\tilde{\theta}} \langle \hat{\Pi}_{\tilde{\theta}} \rangle_{\text{PES}}$ and gives $\partial_{\tilde{\theta}} \langle \hat{\Pi}_{\tilde{\theta}} \rangle_{\text{PES}} = o(1)$ as $T \to \infty$. From Eq. (31), we conclude that $\sqrt{F_{\tilde{\theta}}} = o(1)$ as $T \to \infty$. 2. Solution exists: the stationary phases occur exactly at the non-pumping points $\epsilon_{n,m}' = 0$, which sets Eq. (G13) to 0 at any moment as [Eq. (G17)]:

$$\partial_{\tilde{\theta}}\chi_{nm}(\tilde{x},\tilde{y},\tilde{\theta}) = -\frac{1}{\sqrt{2}} \left(\frac{1}{\omega_1} + \frac{1}{\omega_2} \right) \epsilon'_m \left[-\frac{1}{2} \left(\frac{\omega_1}{\omega_2} + \frac{\omega_2}{\omega_1} \right) \tilde{x} + \frac{1}{2} \left(\frac{1}{\omega_1^2} - \frac{1}{\omega_2^2} \right) \tilde{y} + \frac{1}{\sqrt{2}} \left(\frac{1}{\omega_1} + \frac{1}{\omega_2} \right) \tilde{\theta} \right] = 0.$$
 (G18)

We hence evaluate $\langle \hat{\Pi}_{\tilde{\theta}} \rangle_{\text{PES}}$ according to Eq. (G9) and $\partial_{\tilde{\theta}} \langle \hat{\Pi}_{\tilde{\theta}} \rangle_{\text{PES}}$ according to Eq. (G12). For an everywhere dispersive band structure ($\partial_{\Delta\phi} \epsilon_n$ and $\partial_{\Delta\phi}^2 \epsilon_n$ not vanishing at the same time), the Hessian of $\chi_{nm}(\tilde{x}, \tilde{y}, \tilde{\theta})$ is non-zero, dictating all critical points non-degenerate. In this case, we have $\langle \hat{\Pi}_{\tilde{\theta}} \rangle_{\text{PES}} = O(\frac{1}{T})$ and $\partial_{\tilde{\theta}} \langle \hat{\Pi}_{\tilde{\theta}} \rangle_{\text{PES}} = O(\frac{1}{T})$, which necessarily gives

rise to $\sqrt{F_{\tilde{\theta}}} = O(\frac{1}{T})$. Together with the first case, we conclude that given an everywhere dispersive band structure, $\langle \hat{\Pi}_{\tilde{\theta}} \rangle_{\text{PES}} = O(\frac{1}{T})$ and $\partial_{\tilde{\theta}} \langle \hat{\Pi}_{\tilde{\theta}} \rangle_{\text{PES}} = o(1)$, yielding $\sqrt{F_{\tilde{\theta}}} = o(1)$ that fails to reach either the SQL or the HL. If the everywhere dispersive condition is lifted, the Hessian of $\chi_{nm}(\tilde{x}, \tilde{y}, \tilde{\theta})$ is, if solution exists, zero, which then gives rise to degenerate critical points. Here, we can bound both $\langle \hat{\Pi}_{\tilde{\theta}} \rangle_{\text{PES}} = O(1)$ and $\partial_{\tilde{\theta}} \langle \hat{\Pi}_{\tilde{\theta}} \rangle_{\text{PES}} = O(1)$ by some O(1) constant. In this case, $\langle \hat{\Pi}_{\tilde{\theta}} \rangle_{\text{PES}}$ is still slowly oscillating, which in general gives $\sqrt{F_{\tilde{\theta}}} = O(1)$. Potential exceptions arise when $\left| \langle \hat{\Pi}_{\tilde{\theta}} \rangle_{\text{PES}} \right| \to 1$ as $T \to \infty$, where the denominator of Eq. (31) becomes singular, and no straightforward argument can be made for $F_{\tilde{\theta}}$. Nevertheless, in the numerical examples studied in this work (see also the following discussions when $\omega_1 = \omega_2$), we find no enhancement arising from these singularities.

Case $\omega_1 = \omega_2$: To enhance the sensitivity of the parity measurement from a non-vanishing Eq. (G13) as $T \to \infty$, we need to set the driving frequencies to be identical $\omega_1 = \omega_2 = \omega$. This constitutes our first necessary condition.

In this case, we relabel the characteristic functions χ_{nm} as follows:

$$\mathcal{G}_{nm}(\tilde{x},\tilde{\theta}) = \epsilon_n(\tilde{x}) - \epsilon_m \left[-\tilde{x} + \frac{\sqrt{2}}{\omega} \tilde{\theta} \right], \tag{G19}$$

which is the form given in Eq. (33). The difference of \mathcal{G}_{nm} from the general functions χ_{nm} is that the former does not depend on the second variable \tilde{y} . The critical points of \mathcal{G}_{nm} are already degenerate as $\partial_{\tilde{y}}^2 \mathcal{G}_{nm} = \partial_{\tilde{x}} \partial_{\tilde{y}} \mathcal{G}_{nm} = 0$. We need to integrate out this redundancy in evaluating $\langle \hat{\Pi}_{\tilde{\theta}} \rangle_{\text{PES}}$ and $\partial_{\tilde{\theta}} \langle \hat{\Pi}_{\tilde{\theta}} \rangle_{\text{PES}}$

$$\langle \hat{\Pi}_{\tilde{\theta}} \rangle_{\text{PES}} = \frac{1}{\mathcal{N}_T^2} \sum_{m,n=1}^d \int d\tilde{x} \bar{\mathcal{M}}_{nm}(\tilde{x}, \tilde{\theta}) e^{-i\mathcal{G}_{nm}(\tilde{x}, \tilde{\theta})T}, \tag{G20}$$

$$\partial_{\tilde{\theta}} \langle \hat{\Pi}_{\tilde{\theta}} \rangle_{\text{PES}} = \frac{1}{\mathcal{N}_T^2} \sum_{m,n=1}^d \int d\tilde{x} \left[\partial_{\tilde{\theta}} \bar{\mathcal{M}}_{nm}(\tilde{x},\tilde{\theta}) \right] e^{-i\mathcal{G}_{nm}(\tilde{x},\tilde{\theta})T}$$
(G21)

$$-\frac{iT}{\mathcal{N}_T^2} \sum_{m,n=1}^d \int d\tilde{x} \bar{\mathcal{M}}_{nm}(\tilde{x},\tilde{\theta}) \left[\partial_{\tilde{\theta}} \mathcal{G}_{nm}(\tilde{x},\tilde{\theta}) \right] e^{-i\mathcal{G}_{nm}(\tilde{x},\tilde{\theta})T}, \tag{G22}$$

$$\bar{\mathcal{M}}_{nm}(\tilde{x},\tilde{\theta}) = \int d\tilde{y} f^*(\phi_2 + \tilde{\theta},\phi_1 - \tilde{\theta}) f(\phi_1,\phi_2) \left| u_m^*(\phi_2 + \tilde{\theta},\phi_1 - \tilde{\theta}) u_n(\phi_1,\phi_2) \right|^2.$$
 (G23)

As before, when $T \to \infty$, the integrands in Eq. (G20)(G21)(G22) are fast-oscillating and the integrals are governed by their behaviors at critical points:

$$\partial_{\tilde{x}} \mathcal{G}_{nm}(\tilde{x}, \tilde{\theta}) = 0. \tag{G24}$$

The existence of solutions to Eq. (G24) is guaranteed, unlike in the case where $\omega_1 \neq \omega_2$, as $\mathcal{G}_{nm}(\tilde{x}, \tilde{\theta})$ is periodic in \tilde{x} . By the mean value theorem, there must exist at least one \tilde{x}_0 such that $\partial_{\tilde{x}}\mathcal{G}_{nm}(\tilde{x}, \tilde{\theta})|_{\tilde{x}=\tilde{x}_0}=0$. If these critical points are non-degenerate, the asymptotic behaviors of Eq. (G20) and Eq. (G21) are both governed by $O(\frac{1}{\sqrt{T}})$, while that of Eq. (G22) by $O(\sqrt{T})$. The appearance of \sqrt{T} instead of T arises from the reduction of the integral's dimensionality from 2 to 1. In consequence, Eq. (31) gives rise to $\sqrt{F_{\tilde{\theta}}} = O(\sqrt{T})$, exhibiting a SQL scaling as $T \to \infty$. We hence conclude that the sub-SQL sensitivity from parity measurement can be obtained only if the critical points of $\mathcal{G}_{n,m}$ are degenerate. This constitutes our second necessary condition.

As a final remark, the coefficient $\partial_{\tilde{\theta}} \mathcal{G}_{nm}(\tilde{x},\theta)$ of the integrand in Eq. (G22) need to be non-vanishing at stationary phases such the enhancement of $\partial_{\tilde{\theta}} \langle \hat{\Pi} \rangle_{\text{PES}}$ from Eq. (G22) is non-zero. Otherwise, Eq. (G21) at most gives an O(1) contribution in $\partial_{\tilde{\theta}} \langle \hat{\Pi} \rangle_{\text{PES}}$ and $\langle \hat{\Pi} \rangle_{\text{PES}}$ again oscillates slowly. As before, we expect $\sqrt{F_{\tilde{\theta}}} = O(1)$ in general. Strictly speaking, singularities may occur when $\left| \langle \hat{\Pi} \rangle_{\text{PES}} \right| \to 1$, where it becomes difficult to make any straightforward statements about $\sqrt{F_{\tilde{\theta}}}$. However, from extensive numerical studies, we see no enhancement arising from such singularities. An example can be seen from the driven model given in Eq. 24 with coherent-state inputs [Fig. 4.(b)].

Appendix H: Global phase estimation

In this appendix, we review the standard Bayesian procedure [65, 78] for the global phase estimation, which defines the posterior variance $\Delta_p \theta^2$ in Sec. VI. In a global quantum sensor, the unknown phase θ has a finite a priori uncertainty $\Delta \theta$. In this case, the a priori phase should be viewed as a random variable that takes values in $[0, 2\pi)$ according to its distribution function $P(\theta)$. The task now becomes estimating a random outcome θ as precise as possible. The mathematical quantity to be minimized is the mean-square error (MSE) of the estimator [48, 78]:

$$C = \int_{0}^{2\pi} d\theta \, \mathcal{E}(\theta) P(\theta), \qquad (H1)$$

where $\mathcal{E}(\theta) = \sum_{\mu=1}^{M} (\theta_{\text{est}}(\pi_{\mu}) - \theta)^2 p(\pi_{\mu}|\theta)$ is the squared error of the estimator for a given θ . Similarly, the first minimization step is achieved by choosing a minimal MSE estimator whose estimated value coincides with the mean of θ :

$$\theta_{\text{est}}^{\text{MSE}}(\pi_{\mu}) = \int_{0}^{2\pi} d\theta \, \theta p(\theta | \pi_{\mu}), \qquad (\text{H2})$$

where the conditional probabilities $p(\theta|\pi_{\mu})$ and $p(\pi_{\mu}|\theta)$ are related by the Bayes theorem $p(\theta|\pi_{\mu}) = p(\pi_{\mu}|\theta) \frac{P(\theta)}{p(\pi_{\mu})}$ with the marginal probability distribution $p(\pi_{\mu})$ of the outcome π_{μ} given by $p(\pi_{\mu}) = \int_{0}^{2\pi} d\theta \ p(\pi_{\mu}|\theta) P(\theta)$. As a result, the MSE to be minimized becomes the posterior variance of θ :

$$\Delta_{\mathbf{p}}\theta^{2} = \sum_{\mu=1}^{M} p(\pi_{\mu}) \int_{0}^{2\pi} d\theta \left(\theta - \theta_{\text{est}}^{MSE}(\pi_{\mu})\right)^{2} p(\theta|\pi_{\mu}). \tag{H3}$$

From classical information theory, for a single-shot measurement, $\Delta_p \theta^2$ is bounded by a generalized CRB [48]:

$$\Delta_{\mathbf{p}}\theta^2 \ge \frac{1}{\overline{F}_{\theta} + F_0},\tag{H4}$$

where $\overline{F}_{\theta} = \int_{0}^{2\pi} d\theta F_{\theta} P\left(\theta\right)$ is the averaged classical Fisher information [see Eq. (4)] and $F_{0} = \int_{0}^{2\pi} d\theta \left[\frac{d}{d\theta} \log P\left(\theta\right)\right]^{2} P\left(\theta\right)$ is the classical Fisher information for the a priori distribution $P\left(\theta\right)$. As in the local phase estimation, the classical Fisher information is upper-bounded by the corresponding QFI F_{q} . The posterior variance $\Delta_{\rm p}\theta^{2}$ is hence lower-bounded by:

$$\Delta_{\mathbf{p}}\theta^2 \ge \frac{1}{F_a + F_0}.\tag{H5}$$

Taking the limit $P(\theta) \to \delta(\theta - \theta_0)$, Eq. (H5) converges to the qCRB for a local phase sensor [Eq. (7)].

The equality in Eq. (H5) holds if and only if $\overline{F}_{\theta} = F_q$ for any $\theta \in [0, 2\pi)$, which is a stringent condition in experiments. For interferometer-like sensors, the sensitivity is, hence, much worse than the right-hand-side bound. It is also known that the optimal global quantum sensor deviates significantly from its local counterpart in both the probe states and sensing schemes [11]. Recent efforts on optimizing protocols and minimizing the posterior variance $\Delta_p \theta^2$ can be found in [11, 47, 48]. In this work, we focus on the estimation of a local phase, treating the a priori uncertainty $\Delta\theta$ as a source of noise (Sec. VIB).

Appendix I: Superconducting circuit realization

In this appendix, we give an example of establishing superconducting circuits for a specific two-tone Floquet system after quantizing the drives. We follow the standard procedure given in [93, 95].

The time-dependent Hamiltonian in Eq. (41) can be typically realized by the circuit showin in Fig. 9, whose Lagrangian, $\mathcal{L} = T - U$, takes the following form

$$T = \frac{1}{2}C_{q}\dot{\phi}_{q}^{2} + \frac{1}{2}C_{1}\dot{\phi}_{1}^{2} + \frac{1}{2}C_{2}\dot{\phi}_{2}^{2} + \frac{1}{2}C_{x_{1}}\dot{\phi}_{x_{1}}^{2} + \frac{1}{2}C_{x_{2}}\dot{\phi}_{x_{2}}^{2} + \frac{1}{2}C_{y_{1}}\dot{\phi}_{y_{1}}^{2} + \frac{1}{2}C_{y_{2}}\dot{\phi}_{y_{2}}^{2} + \frac{1}{2}C_{qc_{1}}\left(\dot{\phi}_{q} - \dot{\phi}_{y_{1}}\right)^{2} + \frac{1}{2}C_{qc_{2}}\left(\dot{\phi}_{q} - \dot{\phi}_{y_{2}}\right)^{2} + \frac{1}{2}C_{q_{1}}\left(\dot{\phi}_{q} - \dot{\phi}_{1}\right)^{2} + \frac{1}{2}C_{q_{2}}\left(\dot{\phi}_{q} - \dot{\phi}_{y_{2}}\right)^{2} + \frac{1}{2}C_{q_{2}}\left(\dot{\phi}_{q} - \dot{\phi}_{1}\right)^{2} + \frac{1}{2}C_{q_{2}}\left(\dot{\phi}_{q} - \dot{\phi}_{2}\right)^{2},$$

$$U = U\left(\phi_{q}\right) + \frac{1}{2L_{1}}\phi_{1}^{2} + \frac{1}{2L_{2}}\phi_{2}^{2} + \frac{1}{2L_{q_{1}}}\left(\phi_{q} - \phi_{1}\right)^{2} + \frac{1}{2L_{q_{2}}}\left(\phi_{q} - \phi_{2}\right)^{2} + \frac{1}{2L_{q_{2}}}\left(\phi_{q} - \phi_{c_{1}}\right)^{2} + \frac{1}{2L_{q_{2}}}\left(\phi_{q} - \phi_{c_{2}}\right)^{2} + \frac{1}{2L_{q_{2}}}\left(\phi$$

where $U(\phi_q)$ is the potential for the qubit and I(t) is the external current drive on the qubit. For notational simplicity, we implicitly incorporate the coupling strength into I(t). All other related quantities are marked in Fig. 9. Introducing $\phi = (\phi_q, \phi_1, \phi_{y_1}, \phi_{x_1}, \phi_2, \phi_{y_2}, \phi_{x_2})^T$, the kinetic part T has a compact form as $T = \frac{1}{2}\dot{\phi}^T C\dot{\phi}$, where the capacitance matrix is given by:

$$C = \begin{pmatrix} C_q + C_{qc_1} + C_{q1} + C_{qc_2} + C_{q2} & -C_{q1} & -C_{qc_1} & 0 & -C_{q2} & -C_{qc_2} & 0 \\ -C_{q1} & C_1 + C_{c_11} + C_{q1} & -C_{c_11} & 0 & 0 & 0 & 0 \\ -C_{qc_1} & -C_{c_11} & C_{y_1} + C_{qc_1} + C_{c_11} & 0 & 0 & 0 & 0 \\ 0 & 0 & 0 & C_{x_1} & 0 & 0 & 0 \\ -C_{q2} & 0 & 0 & 0 & C_2 + C_{c_22} + C_{q2} & -C_{c_22} & 0 \\ -C_{qc_2} & 0 & 0 & 0 & -C_{c_22} & C_{y_2} + C_{qc_2} + C_{c_22} & 0 \\ 0 & 0 & 0 & 0 & 0 & 0 & C_{x_2} \end{pmatrix}.$$

Assuming $C_{x_{1,2}}, C_{y_{1,2}}, C_{1,2}, C_q \gg C_{qc_{1,2}}, C_{c_{1}1}, C_{c_{2},2} \gg C_{q1}, C_{q2}$, its inverse is given as

$$C^{-1} = \begin{pmatrix} \frac{1}{C_q} & \frac{C_{q1} + \frac{C_{qc_1}C_{c_11}}{C_{y1}}}{C_qC_1} & \frac{C_{qc_1}}{C_qC_{y_1}} & 0 & \frac{C_{q1} + \frac{C_{qc_2}C_{c_22}}{C_{y2}}}{C_qC_2} & \frac{C_{qc_2}}{C_qC_{y_2}} & 0 \\ \frac{C_{q1} + \frac{C_{qc_1}C_{c_11}}{C_yC_1}}{C_qC_1} & \frac{1}{C_1} & \frac{C_{c_11}}{C_1C_{y_1}} & 0 & 0 & 0 & 0 \\ \frac{C_{q1} + \frac{C_{qc_1}C_{c_11}}{C_qC_{y_1}}}{C_qC_1} & \frac{C_{c_11}}{C_1C_{y_1}} & \frac{1}{C_y} & 0 & 0 & 0 & 0 \\ 0 & 0 & 0 & \frac{1}{C_{x_1}} & 0 & 0 & 0 & 0 \\ \frac{C_{q1} + \frac{C_{qc_2}C_{c_22}}{C_yC_2}}{C_qC_2} & 0 & 0 & 0 & \frac{1}{C_2} & \frac{C_{c_22}}{C_2C_{y_2}} & 0 \\ \frac{C_{qc_2}}{C_qC_{y_2}} & 0 & 0 & 0 & \frac{C_{c_22}}{C_2C_{y_2}} & \frac{1}{C_{y_2}} & 0 \\ 0 & 0 & 0 & 0 & 0 & 0 & \frac{1}{C_{x_2}} \end{pmatrix},$$

from which we can write down the Hamiltonian in terms of ϕ and its canonical conjugate $\mathbf{n} = \frac{\partial \mathcal{L}}{\partial \dot{\phi}} = C\dot{\phi}$. After canonical quantization (i.e. promoting ϕ and \mathbf{n} to operators), we obtain:

$$\begin{split} \hat{H} = & 4E_{Cq} \hat{n}_q^2 + U\left(\phi_q\right) + \left(\frac{1}{2L_{qc_1}} + \frac{1}{2L_{q_1}} + \frac{1}{2L_{q_2}} + \frac{1}{2L_{q_2}}\right) \phi_q^2 \\ & + 4E_{C1} \hat{n}_1^2 + \left(\frac{1}{2L_1} + \frac{1}{2L_{c_{11}}} + \frac{1}{2L_{q_{1}}}\right) \hat{\phi}_1^2 \\ & + 4E_{C2} \hat{n}_2^2 + \left(\frac{1}{2L_1} + \frac{1}{2L_{c_{22}}} + \frac{1}{2L_{q_2}}\right) \hat{\phi}_2^2 \\ & + 4E_{Cy_1} \hat{n}_{y_1}^2 - E_{y_1} \cos \hat{\phi}_{y_1} \\ & + 4E_{Cy_2} \hat{n}_{y_2}^2 - E_{y_2} \cos \hat{\phi}_{y_2} \\ & + 4E_{Cx_2} \hat{n}_{x_1}^2 - E_{x_1} \cos \hat{\phi}_{x_1} + \left(\frac{1}{2L_{qc_1}} + \frac{1}{2L_{c_1}}\right) \hat{\phi}_{x_1}^2 \\ & + 4E_{Cx_2} \hat{n}_{x_2}^2 - E_{x_2} \cos \hat{\phi}_{x_2} + \left(\frac{1}{2L_{qc_2}} + \frac{1}{2L_{c_2}}\right) \hat{\phi}_{x_2}^2 \\ & - \frac{1}{L_{qc_1}} \hat{\phi}_q \hat{\phi}_{x_1} - \frac{1}{L_{qc_2}} \hat{\phi}_q \hat{\phi}_{x_2} - \frac{1}{L_{c_{11}}} \hat{\phi}_1 \hat{\phi}_{x_1} - \frac{1}{L_{c_{22}}} \hat{\phi}_2 \hat{\phi}_{x_2} - \frac{1}{L_{q_1}} \hat{\phi}_q \hat{\phi}_1 - \frac{1}{L_{q_2}} \hat{\phi}_q \hat{\phi}_2 \\ & + 8 \frac{C_{qc_1}}{\sqrt{C_q C_{y_1}}} \sqrt{E_{Cq} E_{Cy_1}} \hat{n}_q \hat{n}_{y_1} + 8 \frac{C_{qc_2}}{\sqrt{C_q C_{y_2}}} \sqrt{E_{Cq} E_{Cy_2}} \hat{n}_q \hat{n}_{y_2} \\ & + 8 \left(1 + \frac{C_{qc_1} C_{c_{11}}}{C_{q_1} C_{y_1}}\right) \frac{C_{q_1}}{\sqrt{C_q C_1}} \sqrt{E_{Cq} E_{C_1}} \hat{n}_q \hat{n}_1 + 8 \left(1 + \frac{C_{qc_2} C_{c_{22}}}{C_{q_2} C_{y_2}}\right) \frac{C_{q_2}}{\sqrt{C_q C_2}} \sqrt{E_{Cq} E_{C_2}} \hat{n}_q \hat{n}_2 \\ & + I\left(t\right) \hat{\phi}_q, \end{split}$$

with $E_{C\lambda} \equiv \frac{1}{8C_{\lambda}}$. Although the Hamiltonian looks formidable, each line has explicit physical meanings: the first line gives the renormalized qubit energy, the second and third lines give renormalized resonator energies, the fourth and fifth lines give the energy of two charge couplers, the sixth and seventh give the renormalized energies of two flux couplers, the eighth line gives all possible flux couplings, and the ninth to eleventh line give all possible charge couplings. Finally, the last line gives a drive on the qubit. Introducing creation and annihilation operators for each mode and approximating the qubit degrees of freedom by a 2-level system, the above Hamiltonian becomes:

$$\begin{split} \hat{H} &= \frac{\omega_{q}}{2} \hat{\sigma}_{z} + \omega_{1} \hat{a}_{1}^{\dagger} \hat{a}_{1} + \omega_{2} \hat{a}_{2}^{\dagger} \hat{a}_{2} + \omega_{y_{1}} \hat{b}_{y_{1}}^{\dagger} \hat{b}_{y_{1}} + \omega_{y_{2}} \hat{b}_{y_{2}}^{\dagger} \hat{b}_{y_{2}} + \omega_{x_{1}} \hat{b}_{x_{1}}^{\dagger} \hat{b}_{x_{1}} + \omega_{x_{2}} \hat{b}_{x_{2}}^{\dagger} \hat{b}_{x_{2}} \\ &+ g_{qx_{1}} \hat{\sigma}_{x} \left(\hat{b}_{x_{1}} + \hat{b}_{x_{1}}^{\dagger} \right) + g_{qx_{2}} \hat{\sigma}_{x} \left(\hat{b}_{x_{2}} + \hat{b}_{x_{2}}^{\dagger} \right) + g_{1x_{1}} \left(\hat{a}_{1} + \hat{a}_{1}^{\dagger} \right) \left(\hat{b}_{x_{1}} + \hat{b}_{x_{1}}^{\dagger} \right) \\ &+ g_{2x_{2}} \left(\hat{a}_{2} + \hat{a}_{2}^{\dagger} \right) \left(\hat{b}_{x_{2}} + \hat{b}_{x_{2}}^{\dagger} \right) + g_{q^{1}}^{(x)} \hat{\sigma}_{x} \left(\hat{a}_{1} + \hat{a}_{1}^{\dagger} \right) + g_{q^{2}}^{(x)} \hat{\sigma}_{x} \left(\hat{a}_{2} + \hat{a}_{2}^{\dagger} \right) \\ &+ i g_{qy_{1}} \hat{\sigma}_{y} \left(\hat{b}_{x_{1}} - \hat{b}_{x_{1}}^{\dagger} \right) + i g_{qy_{2}} \hat{\sigma}_{y} \left(\hat{b}_{y_{2}} - \hat{b}_{y_{2}}^{\dagger} \right) + g_{1y_{1}} \left(\hat{a}_{1} - \hat{a}_{1}^{\dagger} \right) \left(\hat{b}_{y_{1}} - \hat{b}_{y_{1}}^{\dagger} \right) \\ &+ g_{2y_{2}} \left(\hat{a}_{2} - \hat{a}_{2}^{\dagger} \right) \left(\hat{b}_{y_{2}} - \hat{b}_{y_{2}}^{\dagger} \right) + i g_{q^{1}} \hat{\sigma}_{y} \left(\hat{a}_{1} - \hat{a}_{1}^{\dagger} \right) + i g_{q^{2}}^{(y)} \hat{\sigma}_{y} \left(\hat{a}_{2} - \hat{a}_{2}^{\dagger} \right) \\ &+ \sqrt{\frac{\xi_{q}}{2}} I \left(t \right) \hat{\sigma}_{x} + \frac{\alpha_{x_{1}}}{12} \left(\hat{b}_{x_{1}} + \hat{b}_{x_{1}}^{\dagger} \right)^{4} + \frac{\alpha_{x_{2}}}{12} \left(\hat{b}_{x_{2}} + \hat{b}_{x_{2}}^{\dagger} \right)^{4} + \frac{\alpha_{y_{1}}}{12} \left(\hat{b}_{y_{1}} + \hat{b}_{y_{1}}^{\dagger} \right)^{4} + \frac{\alpha_{y_{2}}}{12} \left(\hat{b}_{y_{2}} + \hat{b}_{y_{2}}^{\dagger} \right)^{4}, \end{split}$$

with ω_q and ξ_g given by the potential $U\left(\phi_q\right)$ (i.e. the type) of the qubit (for example, this factor has similar form as that of 4 couplers' if the qubit is transmon-like, or is given by the persistent current in a flux qubit), and are generally obtained by numerical study or direct measurement. In Fig. 9, we diagrammatically draw a flux qubit to represent such degrees of freedom. Other parameters, on the other hand, can be written out explicitly:

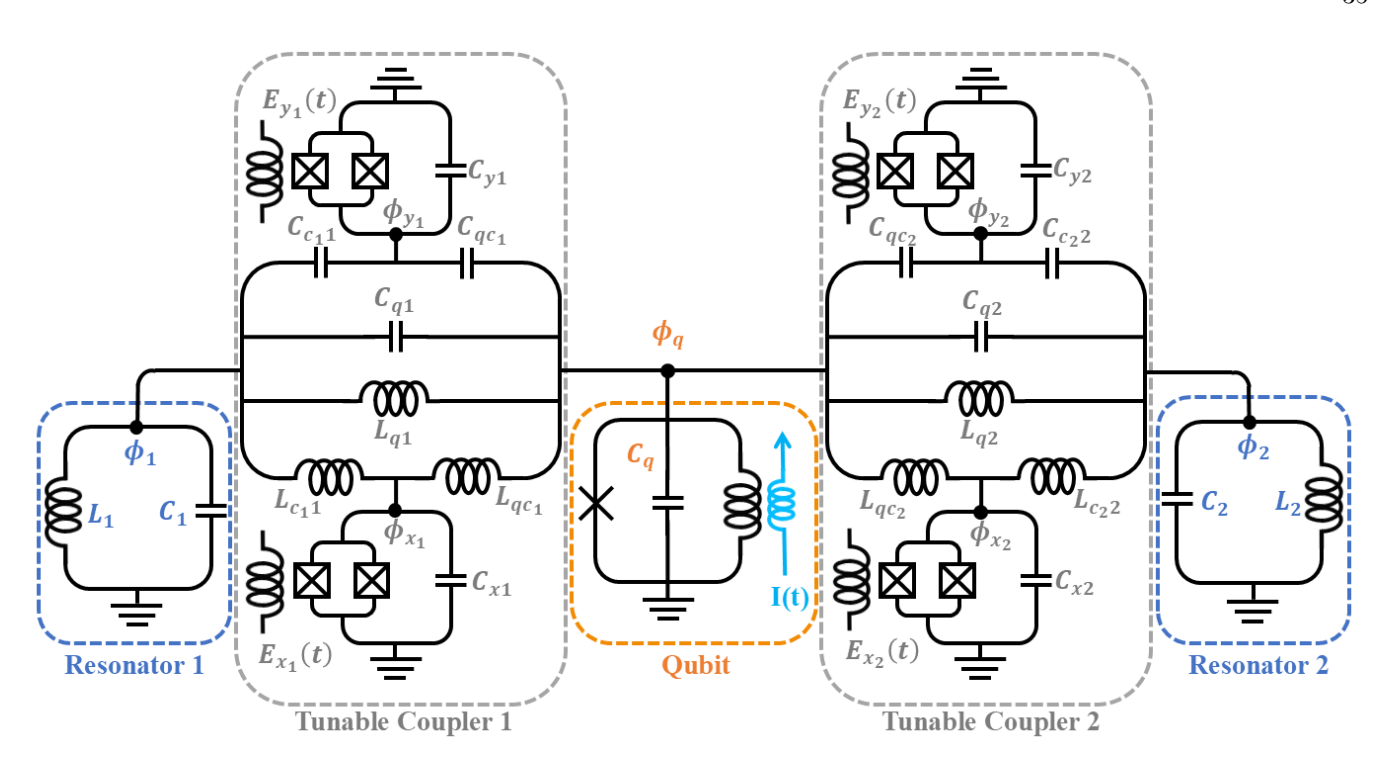


FIG. 9. Superconducting circuit realization of the polarization conversion model. We propose a superconducting circuit that implements the polarization conversion model [Eq. (41)] by tunably coupling two microwave resonators to a superconducting qubit. This tunability is achieved through passive couplings to idler modes under external flux drives. Additionally, we drive the qubit using an external current source I(t), which acts as the qubit energy in the rotating frame.

$$\omega_{1,2} = \sqrt{8E_{C1,C2} \left(\frac{1}{L_{1,2}} + \frac{1}{L_{c_11,c_22}} + \frac{1}{L_{q_1,q_2}}\right)}, \qquad g_{1y_1,2y_2} = -4\frac{C_{c_11,c_22}}{\sqrt{C_{1,2}C_{y_1,y_2}}} \sqrt{\frac{E_{C1,C2}E_{Cy_1,Cy_2}}{\xi_{1,2}\xi_{y_1,y_2}}},$$

$$\omega_{y_{1,2}} = \sqrt{8E_{Cy_1,Cy_2}E_{y_1,y_2}}, \qquad g_{q_{1,q_2}} = -4\left(1 + \frac{C_{qc_1,qc_2}}{C_{q_1,q_2}C_{y_1y_2}}\right) \frac{C_{q_1,q_2}}{\sqrt{C_qC_{1,2}}} \sqrt{\frac{E_{Cq}E_{C1,C2}}{\xi_q\xi_{1,2}}},$$

$$g_{qx_1,qx_2} = -\frac{\sqrt{\xi_q\xi_{x_1,x_2}}}{2L_{qc_1,qc_2}}, \qquad \alpha_{x_1,x_2} = -\frac{\xi_{y_1,y_2}^2}{8}E_{y_1,y_2},$$

$$g_{1x_1,2x_2} = -\frac{\sqrt{\xi_1,2\xi_{x_1,x_2}}}{2L_{c_11,c_22}}, \qquad \xi_{1,2} = \sqrt{\frac{8E_{Cy_1,Cy_2}}{L_{c_11,c_22}}} + \frac{1}{L_{q_1,q_2}},$$

$$g_{qy_1,qy_2} = -4\frac{C_{qc_1,qc_2}}{\sqrt{C_qC_{y_1,y_2}}} \sqrt{\frac{E_{Cq}E_{Cy_1,Cy_2}}{\xi_q\xi_{y_1,y_2}}},$$

$$\xi_{y_1,y_2} = \sqrt{\frac{8E_{Cy_1,Cy_2}}{E_{y_1,y_2}}},$$

$$\xi_{y_1,y_2} = \sqrt{\frac{8E_{Cy_1,Cy_2}}{E_{y_1,y_2}}},$$

$$\xi_{y_1,y_2} = \sqrt{\frac{8E_{Cy_1,Cx_2}}{E_{y_1,y_2}}}.$$

$$\xi_{x_1,x_2} = \sqrt{\frac{8E_{Cy_1,Cx_2}}{E_{x_1,x_2}} + \frac{1}{L_{c_11,c_2}}}}.$$

$$(14)$$

We now apply a Schrieffer-Wolff transform $\hat{U}_{SW} = e^{\hat{S}_x + \hat{S}_y}$ on the Hamiltonian [Eq. (I3)], which is defined as:

$$\begin{split} \hat{S}_{x} = & \frac{1}{2} \frac{g_{qx_{1}}}{\omega_{q} - \omega_{x_{1}}} \left(\hat{\sigma}^{+} \hat{b}_{x_{1}} - \hat{\sigma}^{-} \hat{b}_{x_{1}}^{\dagger} \right) + \frac{1}{2} \frac{g_{qx_{2}}}{\omega_{q} - \omega_{x_{2}}} \left(\hat{\sigma}^{+} \hat{b}_{x_{2}} - \hat{\sigma}^{-} \hat{b}_{x_{2}}^{\dagger} \right) \\ & + \frac{1}{2} \frac{g_{qx_{1}}}{\omega_{q} + \omega_{x_{1}}} \left(\hat{\sigma}^{+} \hat{b}_{x_{1}}^{\dagger} - \hat{\sigma}^{-} \hat{b}_{x_{1}} \right) + \frac{1}{2} \frac{g_{qx_{2}}}{\omega_{q} + \omega_{x_{2}}} \left(\hat{\sigma}^{+} \hat{b}_{x_{2}}^{\dagger} - \hat{\sigma}^{-} \hat{b}_{x_{2}} \right) \\ & + \frac{g_{1x_{1}}}{\omega_{1} - \omega_{x_{1}}} \left(\hat{a}_{1}^{\dagger} \hat{b}_{x_{1}} - \hat{a}_{1} \hat{b}_{x_{1}}^{\dagger} \right) + \frac{g_{2x_{2}}}{\omega_{2} - \omega_{x_{2}}} \left(\hat{a}_{2}^{\dagger} \hat{b}_{x_{2}} - \hat{a}_{2} \hat{b}_{x_{2}}^{\dagger} \right) \\ & + \frac{g_{1x_{1}}}{\omega_{1} + \omega_{x_{1}}} \left(\hat{a}_{1}^{\dagger} \hat{b}_{x_{1}}^{\dagger} - \hat{a}_{1} \hat{b}_{x_{1}} \right) + \frac{g_{2x_{2}}}{\omega_{2} + \omega_{x_{2}}} \left(\hat{a}_{2}^{\dagger} \hat{b}_{x_{2}}^{\dagger} - \hat{a}_{2} \hat{b}_{x_{2}} \right) , \\ \hat{S}_{y} = & \frac{1}{2} \frac{g_{qy_{1}}}{\omega_{q} - \omega_{y_{1}}} \left(\hat{\sigma}^{+} \hat{b}_{y_{1}} - \hat{\sigma}^{-} \hat{b}_{y_{1}}^{\dagger} \right) + \frac{1}{2} \frac{g_{qy_{2}}}{\omega_{q} - \omega_{y_{2}}} \left(\hat{\sigma}^{+} \hat{b}_{y_{2}} - \hat{\sigma}^{-} \hat{b}_{y_{2}}^{\dagger} \right) \\ & - \frac{1}{2} \frac{g_{qy_{1}}}{\omega_{q} + \omega_{y_{1}}} \left(\hat{\sigma}^{+} \hat{b}_{y_{1}}^{\dagger} - \hat{\sigma}^{-} \hat{b}_{y_{1}} \right) - \frac{g_{2y_{2}}}{\omega_{q} + \omega_{y_{2}}} \left(\hat{a}_{1}^{\dagger} \hat{b}_{y_{2}} - \hat{\sigma}^{-} \hat{b}_{y_{2}} \right) \\ & - \frac{g_{1y_{1}}}{\omega_{1} - \omega_{y_{1}}} \left(\hat{a}_{1}^{\dagger} \hat{b}_{y_{1}} - \hat{a}_{1} \hat{b}_{y_{1}}^{\dagger} \right) - \frac{g_{2y_{2}}}{\omega_{2} - \omega_{y_{2}}} \left(\hat{a}_{2}^{\dagger} \hat{b}_{y_{2}} - \hat{a}_{2} \hat{b}_{y_{2}}^{\dagger} \right) \\ & + \frac{g_{1y_{1}}}{\omega_{1} + \omega_{y_{1}}} \left(\hat{a}_{1}^{\dagger} \hat{b}_{y_{1}}^{\dagger} - \hat{a}_{1} \hat{b}_{y_{1}} \right) + \frac{g_{2y_{2}}}{\omega_{2} - \omega_{y_{2}}} \left(\hat{a}_{2}^{\dagger} \hat{b}_{y_{2}}^{\dagger} - \hat{a}_{2} \hat{b}_{y_{2}} \right) , \end{split}$$

with $\hat{\sigma}^{\pm} = \hat{\sigma}_x \pm i\hat{\sigma}_y$. By assuming that 4 couplers remain in their ground states (i.e. the coupling is dispersive) and small nonlinearities $|\alpha_{x_1,x_2,y_1,y_2}| \ll |\omega_{q,1,2} \pm \omega_{x_1,x_2,y_1,y_2}|$, dropping all fast-oscillating terms, we finally obtain an effective Hamiltonian between the driven qubit and two resonators:

$$\hat{H}_{eff} = \frac{\omega_q}{2} \hat{\sigma}_z + \sqrt{\frac{\xi_q}{2}} I(t) \hat{\sigma}_x + \omega_1 \hat{a}_1^{\dagger} \hat{a}_1 + \omega_2 \hat{a}_2^{\dagger} \hat{a}_2
+ \tilde{g}_{q1}^{(x)} \hat{\sigma}_x \left(\hat{a}_1 + \hat{a}_1^{\dagger} \right) + \tilde{g}_{q2}^{(x)} \hat{\sigma}_x \left(\hat{a}_2 + \hat{a}_2^{\dagger} \right) + i \tilde{g}_{q1}^{(y)} \hat{\sigma}_y \left(\hat{a}_1 - \hat{a}_1^{\dagger} \right) + i \tilde{g}_{q2}^{(y)} \hat{\sigma}_y \left(\hat{a}_2 - \hat{a}_2^{\dagger} \right),$$
(I6)

where

$$\begin{split} \tilde{g}_{q1}^{(x)} = & g_{q1}^{(x)} + \frac{1}{2} g_{qx_1} g_{1x_1} \left[\left(\frac{1}{\omega_q - \omega_{x_1}} - \frac{1}{\omega_q + \omega_{x_1}} \right) + \left(\frac{1}{\omega_1 - \omega_{x_1}} - \frac{1}{\omega_1 + \omega_{x_1}} \right) \right], \\ \tilde{g}_{q2}^{(x)} = & g_{q2}^{(x)} + \frac{1}{2} g_{qx_2} g_{1x_2} \left[\left(\frac{1}{\omega_q - \omega_{x_2}} - \frac{1}{\omega_q + \omega_{x_2}} \right) + \left(\frac{1}{\omega_2 - \omega_{x_2}} - \frac{1}{\omega_2 + \omega_{x_2}} \right) \right], \\ \tilde{g}_{q1}^{(y)} = & g_{q1}^{(y)} - \frac{1}{2} g_{qy_1} g_{1y_1} \left[\left(\frac{1}{\omega_q - \omega_{y_1}} - \frac{1}{\omega_q + \omega_{y_1}} \right) + \left(\frac{1}{\omega_1 - \omega_{y_1}} - \frac{1}{\omega_1 + \omega_{y_1}} \right) \right], \\ \tilde{g}_{q2}^{(y)} = & g_{q2}^{(y)} - \frac{1}{2} g_{qy_2} g_{1y_2} \left[\left(\frac{1}{\omega_q - \omega_{y_2}} - \frac{1}{\omega_q + \omega_{y_2}} \right) + \left(\frac{1}{\omega_2 - \omega_{y_2}} - \frac{1}{\omega_2 + \omega_{y_2}} \right) \right]. \end{split}$$

By threading time-dependent external flux in the dc-SQUIDs of 4 couplers, we can make 4 couplers' frequencies time-dependent $\omega_{x_1,x_2,y_1,y_2}(t)$, and hence 4 time-dependent couplings $\tilde{g}_{q1,q2}^{(x,y)}(t)$. Note that we leave a time-independent coupling $g_{q1,q2}^{(x,y)}$ in each of the couplings, such that the offset can be tuned exactly to zero. Setting $\omega_1 = \omega_2 = \omega$ and

$$\tilde{g}_{q1}^{(x)}(t) = \tilde{g}_{q2}^{(x)}(t) = \mathcal{A}\cos(\omega_q t),$$

$$\tilde{g}_{q1}^{(y)}(t) = -\tilde{g}_{q2}^{(y)}(t) = -\mathcal{A}\cos(\omega_q t),$$

$$\sqrt{\frac{\xi_q}{2}}I(t) = \omega_0\cos(\omega_q t),$$
(I8)

we recover the Hamiltonian in Eq. (41).

^[1] J. Aasi et al., Enhanced sensitivity of the ligo gravitational wave detector by using squeezed states of light,

- [2] M. Tse et al., Quantum-enhanced advanced ligo detectors in the era of gravitational-wave astronomy, Phys. Rev. Lett. 123, 231107 (2019).
- [3] J. Ye and P. Zoller, Essay: Quantum sensing with atomic, molecular, and optical platforms for fundamental physics, Phys. Rev. Lett. **132**, 190001 (2024).
- [4] N. Aslam, H. Zhou, E. K. Urbach, M. J. Turner, R. L. Walsworth, M. D. Lukin, and H. Park, Quantum sensors for biomedical applications, Nat. Rev. Phys. 5, 157 (2023).
- [5] J. Ahn, Z. Xu, J. Bang, P. Ju, X. Gao, and T. Li, Ultrasensitive torque detection with an optically levitated nanorotor, Nat. Nanotechnol. 15, 89 (2020).
- [6] J. Chaste, A. Eichler, J. Moser, G. Ceballos, R. Rurali, and A. Bachtold, A nanomechanical mass sensor with yoctogram resolution, Nat. Nanotechnol. 7, 301 (2012).
- [7] V. Giovannetti, S. Lloyd, and L. Maccone, Advances in quantum metrology, Nat. Photonics 5, 222 (2011).
- [8] V. Giovannetti, S. Lloyd, and L. Maccone, Quantum-enhanced measurements: Beating the standard quantum limit, Science **306**, 1330 (2004).
- [9] D. J. Wineland, J. J. Bollinger, W. M. Itano, F. L. Moore, and D. J. Heinzen, Spin squeezing and reduced quantum noise in spectroscopy, Phys. Rev. A 46, R6797 (1992).
- [10] J. J. Bollinger, W. M. Itano, D. J. Wineland, and D. J. Heinzen, Optimal frequency measurements with maximally correlated states, Phys. Rev. A 54, R4649 (1996).
- [11] C. D. Marciniak, T. Feldker, I. Pogorelov, R. Kaubruegger, D. V. Vasilyev, R. van Bijnen, P. Schindler, P. Zoller, R. Blatt, and T. Monz, Optimal metrology with programmable quantum sensors, Nature 603, 604 (2022).
- [12] R. Demkowicz-Dobrzański, M. Jarzyna, and J. Kołodyński, Quantum limits in optical interferometry, in <u>Progress in Optics</u> (Elsevier, 2015) p. 345–435.
- [13] G. A. Durkin and J. P. Dowling, Local and global distinguishability in quantum interferometry, Phys. Rev. Lett. 99, 070801 (2007).
- [14] D. Leibfried, M. D. Barrett, T. Schaetz, J. Britton, J. Chiaverini, W. M. Itano, J. D. Jost, C. Langer, and D. J. Wineland, Toward heisenberg-limited spectroscopy with multiparticle entangled states, Science 304, 1476 (2004).
- [15] J. P. Dowling, Quantum optical metrology the low-down on high-n00n states, Contemp. Phys. 49, 125 (2008).
- [16] J. Joo, W. J. Munro, and T. P. Spiller, Quantum metrology with entangled coherent states, Phys. Rev. Lett. 107, 083601 (2011).
- [17] R. J. Birrittella, P. M. Alsing, and C. C. Gerry, The parity operator: Applications in quantum metrology, AVS Quantum Sci. 3, 014701 (2021).
- [18] C. C. Gerry and J. Mimih, The parity operator in quantum optical metrology, Contemp. Phys. 51, 497 (2010).
- [19] L. Pezzé and A. Smerzi, Mach-zehnder interferometry at the heisenberg limit with coherent and squeezed-vacuum light, Phys. Rev. Lett. 100, 073601 (2008).
- [20] J. Zhang, M. Um, D. Lv, J.-N. Zhang, L.-M. Duan, and K. Kim, Noon states of nine quantized vibrations in two radial modes of a trapped ion, Phys. Rev. Lett. 121, 160502 (2018).

- [21] M. W. Mitchell, J. S. Lundeen, and A. M. Steinberg, Super-resolving phase measurements with a multiphoton entangled state, Nature 429, 161 (2004).
- [22] G. Y. Xiang, B. L. Higgins, D. W. Berry, H. M. Wiseman, and G. J. Pryde, Entanglement-enhanced measurement of a completely unknown optical phase, Nat. Photonics 5, 43 (2011).
- [23] I. Afek, O. Ambar, and Y. Silberberg, High-noon states by mixing quantum and classical light, Science 328, 879 (2010).
- [24] T. Oka and H. Aoki, Photovoltaic hall effect in graphene, Phys. Rev. B 79, 081406 (2009).
- [25] N. H. Lindner, G. Refael, and V. Galitski, Floquet topological insulator in semiconductor quantum wells, Nat. Phys. 7, 490 (2011).
- [26] N. H. Lindner, D. L. Bergman, G. Refael, and V. Galitski, Topological floquet spectrum in three dimensions via a two-photon resonance, Phys. Rev. B 87, 235131 (2013).
- [27] J.-i. Inoue and A. Tanaka, Photoinduced transition between conventional and topological insulators in twodimensional electronic systems, Phys. Rev. Lett. 105, 017401 (2010).
- [28] F. Nathan, I. Martin, and G. Refael, Topological frequency conversion in weyl semimetals, Phys. Rev. Res. 4, 043060 (2022).
- [29] Y. H. Wang, H. Steinberg, P. Jarillo-Herrero, and N. Gedik, Observation of floquet-bloch states on the surface of a topological insulator, Science 342, 453 (2013).
- [30] M. C. Rechtsman, J. M. Zeuner, Y. Plotnik, Y. Lumer, D. Podolsky, F. Dreisow, S. Nolte, M. Segev, and A. Szameit, Photonic floquet topological insulators, Nature 496, 196 (2013).
- [31] Y.-G. Peng, C.-Z. Qin, D.-G. Zhao, Y.-X. Shen, X.-Y. Xu, M. Bao, H. Jia, and X.-F. Zhu, Experimental demonstration of anomalous floquet topological insulator for sound, Nat. Commun. 7, 13368 (2016).
- [32] I. Martin, G. Refael, and B. Halperin, Topological frequency conversion in strongly driven quantum systems, Phys. Rev. X 7, 041008 (2017).
- [33] S. Körber, L. Privitera, J. C. Budich, and B. Trauzettel, Interacting topological frequency converter, Phys. Rev. Res. 2, 022023 (2020).
- [34] J. Luneau, C. Dutreix, Q. Ficheux, P. Delplace, B. Douçot, B. Huard, and D. Carpentier, Topological power pumping in quantum circuits, Phys. Rev. Res. 4, 013169 (2022).
- [35] I.-D. Potirniche, A. C. Potter, M. Schleier-Smith, A. Vishwanath, and N. Y. Yao, Floquet symmetryprotected topological phases in cold-atom systems, Phys. Rev. Lett. 119, 123601 (2017).
- [36] M. S. Rudner, N. H. Lindner, E. Berg, and M. Levin, Anomalous edge states and the bulk-edge correspondence for periodically driven two-dimensional systems, Phys. Rev. X 3, 031005 (2013).
- [37] P. Titum, E. Berg, M. S. Rudner, G. Refael, and N. H. Lindner, Anomalous floquet-anderson insulator as a nonadiabatic quantized charge pump, Phys. Rev. X 6, 021013 (2016).
- [38] R. Roy and F. Harper, Periodic table for floquet topological insulators, Phys. Rev. B 96, 155118 (2017).
- [39] C. W. von Keyserlingk and S. L. Sondhi, Phase structure of one-dimensional interacting floquet systems. ii. symmetry-broken phases, Phys. Rev. B 93, 245146

- (2016).
- [40] F. Nathan, G. Refael, M. S. Rudner, and I. Martin, Quantum frequency locking and downconversion in a driven qubit-cavity system, Phys. Rev. Res. 2, 043411 (2020).
- [41] F. Nathan, I. Martin, and G. Refael, Topological frequency conversion in a driven dissipative quantum cavity, Phys. Rev. B 99, 094311 (2019).
- [42] D. M. Long, P. J. D. Crowley, A. J. Kollár, and A. Chandran, Boosting the quantum state of a cavity with floquet driving, Phys. Rev. Lett. 128, 183602 (2022).
- [43] C. W. Helstrom, Quantum detection and estimation theory, J. Stat. Phys. 1, 231 (1969).
- [44] L. Pezzè, A. Smerzi, M. K. Oberthaler, R. Schmied, and P. Treutlein, Quantum metrology with nonclassical states of atomic ensembles, Rev. Mod. Phys. 90, 035005 (2018).
- [45] S. L. Braunstein and C. M. Caves, Statistical distance and the geometry of quantum states, Phys. Rev. Lett. 72, 3439 (1994).
- [46] T. Oka and S. Kitamura, Floquet engineering of quantum materials, Annu. Rev. Condens. Matter Phys. 10, 387 (2019).
- [47] R. Kaubruegger, A. Shankar, D. V. Vasilyev, and P. Zoller, Optimal and variational multiparameter quantum metrology and vector-field sensing, PRX Quantum 4, 020333 (2023).
- [48] R. Kaubruegger, D. V. Vasilyev, M. Schulte, K. Hammerer, and P. Zoller, Quantum variational optimization of ramsey interferometry and atomic clocks, Phys. Rev. X 11, 041045 (2021).
- [49] U. Dorner, R. Demkowicz-Dobrzanski, B. J. Smith, J. S. Lundeen, W. Wasilewski, K. Banaszek, and I. A. Walmsley, Optimal quantum phase estimation, Phys. Rev. Lett. 102, 040403 (2009).
- [50] B. M. Escher, R. L. de Matos Filho, and L. Davidovich, General framework for estimating the ultimate precision limit in noisy quantum-enhanced metrology, Nat. Phys. 7, 406 (2011).
- [51] R. Demkowicz-Dobrzanski, U. Dorner, B. J. Smith, J. S. Lundeen, W. Wasilewski, K. Banaszek, and I. A. Walmsley, Quantum phase estimation with lossy interferometers, Phys. Rev. A 80, 013825 (2009).
- [52] G. Tóth and I. Apellaniz, Quantum metrology from a quantum information science perspective, J. Phys. A 47, 424006 (2014).
- [53] C. L. Degen, F. Reinhard, and P. Cappellaro, Quantum sensing, Rev. Mod. Phys. 89, 035002 (2017).
- [54] L. Pezzè, A. Smerzi, M. K. Oberthaler, R. Schmied, and P. Treutlein, Quantum metrology with nonclassical states of atomic ensembles, Rev. Mod. Phys. 90, 035005 (2018).
- [55] M. G. A. Paris, Entanglement and visibility at the output of a mach-zehnder interferometer, Phys. Rev. A 59, 1615 (1999).
- [56] G. Haack, H. Förster, and M. Büttiker, Parity detection and entanglement with a mach-zehnder interferometer, Phys. Rev. B 82, 155303 (2010).
- [57] S. Colombo, E. Pedrozo-Peñafiel, and V. Vuletić, Entanglement-enhanced optical atomic clocks, Appl. Phys. Lett. 121, 210502 (2022).
- [58] B. Yurke, S. L. McCall, and J. R. Klauder, Su(2) and su(1,1) interferometers, Phys. Rev. A 33, 4033 (1986).
- [59] E. Polino, M. Valeri, N. Spagnolo, and F. Sciarrino, Pho-

- tonic quantum metrology, AVS Quantum Sci. 2, 024703 (2020).
- [60] D.-W. Wang, H. Cai, R.-B. Liu, and M. O. Scully, Mesoscopic superposition states generated by synthetic spinorbit interaction in fock-state lattices, Phys. Rev. Lett. 116, 220502 (2016).
- [61] Y. Maleki and A. M. Zheltikov, A high-n00n output of harmonically driven cavity qed, Sci. Rep. 9, 16780 (2019).
- [62] Y.-H. Kang, Z.-P. Lin, J.-Q. Yang, Y. Wang, J. Song, Z.-B. Yang, and Y. Xia, Effective protocol for generating noon states of resonator modes, Opt. Express 31, 42976 (2023).
- [63] C. Psaroudaki and G. Refael, Energy transfer in random-matrix ensembles of floquet hamiltonians, Phys. Rev. B 108, 064301 (2023).
- [64] Note that $\omega_1 \hat{P}_1 + \omega_2 \hat{P}_2 = 0$ directly leads to $(\omega_1 \partial_{\phi_1} + \omega_2 \partial_{\phi_2}) \epsilon_n = 0$.
- [65] K. Macieszczak, M. Fraas, and R. Demkowicz-Dobrzański, Bayesian quantum frequency estimation in presence of collective dephasing, New J. Phys. 16, 113002 (2014).
- [66] A. Blais, A. L. Grimsmo, S. M. Girvin, and A. Wallraff, Circuit quantum electrodynamics, Rev. Mod. Phys. 93, 025005 (2021).
- [67] M. Aspelmeyer, T. J. Kippenberg, and F. Marquardt, Cavity optomechanics, Rev. Mod. Phys. 86, 1391 (2014).
- [68] A. V. Chumak, V. I. Vasyuchka, A. A. Serga, and B. Hillebrands, Magnon spintronics, Nat. Phys. 11, 453 (2015).
- [69] X.-M. Jin, C.-Z. Peng, Y. Deng, M. Barbieri, J. Nunn, and I. A. Walmsley, Sequential path entanglement for quantum metrology, Sci. Rep. 3, 1779 (2013).
- [70] A. Rath, C. Branciard, A. Minguzzi, and B. Vermersch, Quantum fisher information from randomized measurements, Phys. Rev. Lett. 127, 260501 (2021).
- [71] L. Pezzè, A. Smerzi, M. K. Oberthaler, R. Schmied, and P. Treutlein, Quantum metrology with nonclassical states of atomic ensembles, Rev. Mod. Phys. 90, 035005 (2018).
- [72] Z. Ren, W. Li, A. Smerzi, and M. Gessner, Metrological detection of multipartite entanglement from young diagrams, Phys. Rev. Lett. **126**, 080502 (2021).
- [73] V. Dodonov, I. Malkin, and V. Man'ko, Even and odd coherent states and excitations of a singular oscillator, Physica 72, 597 (1974).
- [74] C. C. Gerry and J. Mimih, Heisenberg-limited interferometry with pair coherent states and parity measurements, Phys. Rev. A 82, 013831 (2010).
- [75] P. M. Anisimov, G. M. Raterman, A. Chiruvelli, W. N. Plick, S. D. Huver, H. Lee, and J. P. Dowling, Quantum metrology with two-mode squeezed vacuum: Parity detection beats the heisenberg limit, Phys. Rev. Lett. 104, 103602 (2010).
- [76] L. Sun, A. Petrenko, Z. Leghtas, B. Vlastakis, G. Kirchmair, K. M. Sliwa, A. Narla, M. Hatridge, S. Shankar, J. Blumoff, L. Frunzio, M. Mirrahimi, M. H. Devoret, and R. J. Schoelkopf, Tracking photon jumps with repeated quantum non-demolition parity measurements, Nature 511, 444 (2014).
- [77] L. Cohen, D. Istrati, L. Dovrat, and H. S. Eisenberg, Super-resolved phase measurements at the shot noise

- limit by parity measurement, Opt. Express **22**, 11945 (2014).
- [78] J. Rubio and J. Dunningham, Quantum metrology in the presence of limited data, New J. Phys. 21, 043037 (2019).
- [79] Z.-L. Xiang, S. Ashhab, J. Q. You, and F. Nori, Hybrid quantum circuits: Superconducting circuits interacting with other quantum systems, Rev. Mod. Phys. 85, 623 (2013).
- [80] C. J. Hood, T. W. Lynn, A. C. Doherty, A. S. Parkins, and H. J. Kimble, The atom-cavity microscope: Single atoms bound in orbit by single photons, Science 287, 1447 (2000).
- [81] D. W. Vernooy, A. Furusawa, N. P. Georgiades, V. S. Ilchenko, and H. J. Kimble, Cavity qed with high-q whispering gallery modes, Phys. Rev. A 57, R2293 (1998).
- [82] T. Niemczyk, F. Deppe, H. Huebl, E. P. Menzel, F. Hocke, M. J. Schwarz, J. J. Garcia-Ripoll, D. Zueco, T. Hümmer, E. Solano, A. Marx, and R. Gross, Circuit quantum electrodynamics in the ultrastrong-coupling regime, Nat. Phys. 6, 772 (2010).
- [83] P. Forn-Díaz, J. Lisenfeld, D. Marcos, J. J. García-Ripoll, E. Solano, C. J. P. M. Harmans, and J. E. Mooij, Observation of the bloch-siegert shift in a qubit-oscillator system in the ultrastrong coupling regime, Phys. Rev. Lett. 105, 237001 (2010).
- [84] D. Malz and A. Smith, Topological two-dimensional floquet lattice on a single superconducting qubit, Phys. Rev. Lett. 126, 163602 (2021).
- [85] S. Rasmussen, K. Christensen, S. Pedersen, L. Kristensen, T. Bækkegaard, N. Loft, and N. Zinner, Superconducting circuit companion—an introduction with worked examples, PRX Quantum 2, 040204 (2021).
- [86] T. P. Orlando, J. E. Mooij, L. Tian, C. H. van der Wal, L. S. Levitov, S. Lloyd, and J. J. Mazo, Superconducting persistent-current qubit, Phys. Rev. B 60, 15398 (1999).
- [87] I. M. Pop, K. Geerlings, G. Catelani, R. J. Schoelkopf, L. I. Glazman, and M. H. Devoret, Coherent suppression of electromagnetic dissipation due to superconducting quasiparticles, Nature 508, 369 (2014).
- [88] L. B. Nguyen, Y.-H. Lin, A. Somoroff, R. Mencia, N. Grabon, and V. E. Manucharyan, High-coherence fluxonium qubit, Phys. Rev. X 9, 041041 (2019).
- [89] I. N. Moskalenko, I. A. Simakov, N. N. Abramov, A. A. Grigorev, D. O. Moskalev, A. A. Pishchimova, N. S. Smirnov, E. V. Zikiy, I. A. Rodionov, and I. S. Besedin, High fidelity two-qubit gates on fluxoniums using a tunable coupler, npj Quantum Inf. 8, 130 (2022).
- [90] R. Harris, A. J. Berkley, M. W. Johnson, P. Bunyk, S. Govorkov, M. C. Thom, S. Uchaikin, A. B. Wilson,

- J. Chung, E. Holtham, J. D. Biamonte, A. Y. Smirnov, M. H. S. Amin, and A. Maassen van den Brink, Signand magnitude-tunable coupler for superconducting flux qubits, Phys. Rev. Lett. **98**, 177001 (2007).
- [91] M. S. Allman, J. D. Whittaker, M. Castellanos-Beltran, K. Cicak, F. da Silva, M. P. DeFeo, F. Lecocq, A. Sirois, J. D. Teufel, J. Aumentado, and R. W. Simmonds, Tunable resonant and nonresonant interactions between a phase qubit and *lc* resonator, Phys. Rev. Lett. 112, 123601 (2014).
- [92] X. Li, T. Cai, H. Yan, Z. Wang, X. Pan, Y. Ma, W. Cai, J. Han, Z. Hua, X. Han, Y. Wu, H. Zhang, H. Wang, Y. Song, L. Duan, and L. Sun, Tunable coupler for realizing a controlled-phase gate with dynamically decoupled regime in a superconducting circuit, Phys. Rev. Appl. 14, 024070 (2020).
- [93] F. Yan, P. Krantz, Y. Sung, M. Kjaergaard, D. L. Campbell, T. P. Orlando, S. Gustavsson, and W. D. Oliver, Tunable coupling scheme for implementing high-fidelity two-qubit gates, Phys. Rev. Appl. 10, 054062 (2018).
- [94] A. M. van den Brink, A. J. Berkley, and M. Yalowsky, Mediated tunable coupling of flux qubits, New J. Phys. 7, 230 (2005).
- [95] D. L. Campbell, A. Kamal, L. Ranzani, M. Senatore, and M. D. LaHaye, Modular tunable coupler for superconducting circuits, Phys. Rev. Appl. 19, 064043 (2023).
- [96] W. Wang, Y. Wu, Y. Ma, W. Cai, L. Hu, X. Mu, Y. Xu, Z.-J. Chen, H. Wang, Y. P. Song, H. Yuan, C.-L. Zou, L.-M. Duan, and L. Sun, Heisenberg-limited singlemode quantum metrology in a superconducting circuit, Nat. Commun. 10, 4382 (2019).
- [97] S. D. Huver, C. F. Wildfeuer, and J. P. Dowling, Entangled fock states for robust quantum optical metrology, imaging, and sensing, Phys. Rev. A 78, 063828 (2008).
- [98] S. Zhou, M. Zhang, J. Preskill, and L. Jiang, Achieving the heisenberg limit in quantum metrology using quantum error correction, Nat. Commun. 9, 78 (2018).
- [99] S. Zhou, A. G. Manes, and L. Jiang, Achieving metrological limits using ancilla-free quantum error-correcting codes, Phys. Rev. A 109, 042406 (2024).
- [100] L. A. Clark, A. Stokes, and A. Beige, Quantumenhanced metrology with the single-mode coherent states of an optical cavity inside a quantum feedback loop, Phys. Rev. A 94, 023840 (2016).
- [101] M. Gessner, L. Pezzè, and A. Smerzi, Entanglement and squeezing in continuous-variable systems, Quantum 1, 17 (2017).